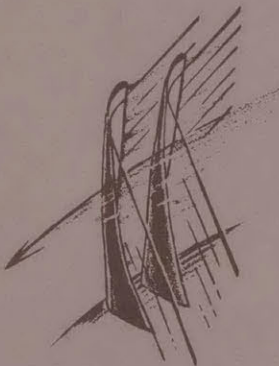DETAILED TIME RESOLVED MEASUREMENTS AND
ANALYSIS OF UNSTEADY FLOW IN A
TRANSONIC COMPRESSOR

by

WING FAI NG

GT & PDL Report No. 150   August 1980

GAS TURBINE & PLASMA DYNAMICS LABORATORY
MASSACHUSETTS INSTITUTE OF TECHNOLOGY
CAMBRIDGE, MASSACHUSETTS

DETAILED TIME RESOLVED MEASUREMENTS AND
ANALYSIS OF UNSTEADY FLOW IN A
TRANSONIC COMPRESSOR

by

WING FAI NG

GT & PDL Report No. 150   August 1980

ABSTRACT

Detailed time and space resolved measurements for a transonic compressor stage have been completed in the MIT Blowdown Compressor Facility. The stage studied was a new first stage for a NASA two-stage machine which incorporated low-aspect-ratio blading. This rotor has an inlet hub/tip ratio of 0.375, aspect ratio of 1.56 and an inlet relative Mach number of 1.38. The purposes of the test were to compare the results obtained by the Blowdown technique with those found by steady state testing at NASA Lewis Research Center, and to provide new time resolved data on the blade-to-blade flow in the rotor and stator. Data were obtained by surveys with a five diaphragm high frequency response probe and by tip casing transducers.

The stage was tested at 100% design speed. Time resolved estimates of efficiency were obtained by direct measurement of stagnation pressure together with calculation of stagnation temperature by the Euler equation using measured tangential flow Mach number. Test results showed that the rotor achieved an adiabatic efficiency of 0.895 at a total pressure ratio of 1.677. The stage achieved an adiabatic efficiency of 0.862 at a total pressure ratio of 1.658. Corrected mass flow at design was measured to be 33.3 Kg/s with respect to air. Time averaged flow quantities in general agree very well with results from steady state tests at NASA Lewis Research Center. A significant difference was observed in the variation of efficiency with radius, with a low efficiency region near mid-span not observed in the steady state testing. Moreover, the measured rotor efficiency in the "core flow" between the blade wakes for the supersonic region is lower than can be explained by normal shock losses. Large streamwise vorticity is observed at the blade trailing edge in the inner half of the annulus, which may be associated with shock termination at the sonic radius.

3
ACKNOWLEDGEMENTS

The author would like to express his sincere appreciation to all of the members of the Gas Turbine Laboratory who contributed to this work. Foremost among these is Professor Jack L. Kerrebrock, without whose expertise on the subject, the completion would have been impossible. He also provided much time and unending encouragement, both were of invaluable help.

Also many thanks are due to Professor Alan H. Epstein, whose guidance was essential in all phases of the research.

Professor William T. Thompkins, Jr. deserves special thanks for providing many helpful suggestions during frequent discussions.

The typing skill of Holly Rathbun is greatly appreciated.

Finally, the author dedicates this thesis to his late beloved Brother, whom he missed very much during his course of study at MIT.

4
TABLE OF CONTENTS

5

LIST OF FIGURES

LIST OF SYMBOLS

ω	Rotational Speed of the Rotor or Vorticity
T	Temperature
θ	Tangential Flow Angle or Tangential Direction
ϕ	Radial Flow Angle
M	Mach Number
r	Radial Direction
$\vec{\omega}$	Vorticity Vector
$\vec{V}$	Velocity Vector
$\dot{m}$	Mass Flow
C_p	Specific Heat at Constant Pressure
I	Moment of Inertia
R	Gas Constant
γ	Ratio of Specific Heat

Subscripts

t	Total or Tip
S	Static
1	Rotor Inlet
2	Rotor Exit or Upstream
θ	Tangential Direction
r	Radial Direction
z	Streamwise Direction
0	Supply Tank Condition

CHAPTER I

INTRODUCTION

The aerodynamic behavior of transonic compressors have been the subject of intensive research and development in recent years. The lack of fully time and space resolved experimental data, combined with great complexities introduced by partially supersonic rotor blades have made the design of efficient stages very difficult. Current design practice still relies to a large degree on experimental data from two-dimensional cascades tested in steady flow. It is believed that a better understanding of the aerodynamics of transonic compressors coupled with a rationalized design process can result in significant improvements in transonic compressor efficiency. Thus large benefits in reduced fuel consumption can result.[1]

Since our understanding of these flows is far from complete, considerable research is presently directed toward unraveling them. However, most available data is from steady state measurements made between blade rows with conventional total pressure probes, wedges probes which give flow angles on the mean axisymmetric stream surfaces, stagnation temperature probes, and casing static pressures. This data gives little information about blade-to-blade variations in the flow, and none about radial flows, which have nearly zero mean values. Due to the highly unsteady nature and three-dimensional effect on flow field in transonic compressor, data which exhibit the blade-to-blade flow are required.

In this paper, the flow field downstream of a full scale transonic compressor stage is investigated. Detailed time resolved measurements

of total and static pressures, radial flow angles and tangential flow angles were taken both downstream of the rotor and stator. Measurements were taken using a high frequency response pressure probe,[2] developed for use in the MIT Blowdown Compressor Facility. The transonic rotor tested is the first-stage of a NASA two stage machine incorporating low-aspect ratio blading. The rotor was designed with an inlet relative Mach number of 1.38 and a stage total pressure ratio of 1.63, Ref. 3. It has excellent overall performance as inferred by conventional steady state techniques.

The scope of this work includes analysis of the data and presentation in terms of flow Mach number, flow angles, and pressure ratios for ready comparison to other data. Where possible, time averaged of the time resolved data are compared to corresponding values obtained by NASA Lewis Research Center by conventional steady state testing. No serious attempt has been made here to interpret the data or resolve conflicts between the two sets of information. This is reserved for a further effort.

CHAPTER II

THE EXPERIMENT

II.A Test Facility

The MIT Blowdown Compressor Facility (Fig. 2.1) used in these
experiments is fully described in Ref. 4, and a short description of
the facility will be presented here. Basically, the Blowdown Facility
consists of a compressor test section (Fig. 2.2) which is initially
separated from a supply tank by an aluminum diaphragm. The test
section is followed by a dump tank into which the compressor discharges.
Before a test, the rotor is brought up to speed in a vacuum and the
diaphragm is ruptured with plastic explosives allowing the test gases
(mixture of Freon and Argon) to flow through the test section. A
throttle plate downstream of the test section controls the mass flow
through the stage. If the supply tank pressure remains high enough to
choke the throttle plate, axial Mach number will remain constant.
The rotor is driven by its own inertia during the test and will
decelerate as it does work on the fluid. On the other hand, the
temperature and pressure in the supply tank (which is essentially at
stagnation condition), decreases as a result of expansion of the gas
into the dump tank. To ensure a constant inlet tangential Mach number,
the change in the supply tank temperature and rotor deceleration must
be governed by the relation

$$\left\{\frac{\omega(t)}{\omega(0)}\right\}^2 = \frac{T_1(t)}{T_1(0)}$$

where ω is the rotational speed of the rotor and T_1 is the temperature

in the supply tank.

This can be achieved by proper matching of the rotating assembly inertia with supply tank conditions. For the current experiments, the tank pressure required to maintain steady state conditions was experimentally determined to be 0.71 atmospheres. Figure 2.3 shows the matching between the rotor deceleration $\{\omega(t)/\omega(0)\}^2$ and the change in supply tank temperature $T_1(t)/T_1(0)$. It shows a rather good fit during the test time, constant rotor inlet velocity triangles are achieved.

In order to obtain circumferential survey across the stator gaps, a slowly rotating stator (Fig. 2.2) was used with a radially traversed probe. To achieve a slowly rotating stator, a massive hub and tip rings were attached to the stator blades, so that the rotating stator will have a large moment of inertia. The maximum angular velocity of the stator is 2% of the rotor angular velocity. Thus during the test, the stator was allowed to rotate, in the same direction as the rotor, while a probe surveyed downstream of it, moving radially inward. This setup resulted in a blade-to-blade survey at the same time as the radial survey.

II.B Test Compressor and Operating Point

The transonic compressor tested is the first-stage of a NASA two stage fan incorporating low-aspect ratio blading. Details of the rotor are described in full in Ref. 3. The rotor has an aspect ratio of 1.56, inlet hub-tip ratio of 0.375 and exit hub-tip ratio of 0.478. A drawing of the rotor blade shape is shown in Fig. 2.5. The rotor has 22 blades and the stator has 34 blades. At design speed, the rotor has an inlet tip relative Mach number of 1.38, and the stage

has a total pressure ratio of 1.63.

The stage was tested at 100% design speed in a mixture of Argon and Freon. This corresponds to an initial rotor speed of 201 rps in the Blowdown experiment, which is about 75% of the design speed when tested in air (267 rps). The operating point of the stage is determined by the rotational speed of the rotor as well as the throttle area behind the stage, which controls the mass flow. In the Blowdown experiment this is adjusted by changing the throttle plate (Fig. 2.2). These two conditions specify the operating point on the performance map and results can be compared to corresponding data from NASA steady state testing. (Reading number 1283 of Ref. 3.) The average static radial tip clearances at leading edge were measured to be 0.171 cm (0.067 in.).

II.C Instrumentation

II.C.1 High Frequency Sphere Probe (Five-Way Probe)

Time resolved measurements of the fluctuating flow field behind the compressor rotor were determined using a miniature high frequency sphere probe described in Ref. 2. The probe is 0.2 inches in diameter yielding a frequency response above 30 KHz. It consists of a nearly spherical head on which five silicon pressure sensors are mounted, (Fig. 2.6 A and B). The transducer in the center sees nearly stagnation pressure while the two side pairs give good angular sensitivity in two planes. During a compressor test the probe is traversed radially inward with the center transducer perpendicular to the mean flow direction. This implies that when surveying the flow field behind the rotor (Port 3), it is necessary to turn the probe by a 45° angle

from the center line.

The aerodynamic behavior of the probe has been established by steady state testing of a model twice the size of the actual probe. A set of calibration curves were obtained which cover a range of Mach numbers from 0.3 to 0.9. The following non-dimensional parameters were retrieved from the calibration measurements and plotted against tangential angle (θ) and radial angle (ϕ).

$$C_{P_4}(\phi,M) = \frac{P_4 - P_S}{P_T - P_S} \qquad (2.1)$$

$$F_{2,3}(\phi,\theta,M) = \frac{P_2 - P_3}{(P_3 - P_1) + (P_2 - P_1)} \qquad (2.2)$$

$$C_{P_1}(\phi,\theta,M) = \frac{P_1 - P_S}{P_T - P_S} \qquad (2.3)$$

$$H(\phi,\theta,M) = \frac{P_T - P_S}{(P_3 - P_1) + (P_2 - P_1)} \qquad (2.4)$$

$$K_{P_{2,3}}(\phi,\theta,M) = \frac{P_{2,3} - P_S}{(P_3 - P_1) + (P_2 - P_1)} \qquad (2.5)$$

Some typical calibration curves which correspond to Mach number 0.7 are presented in Fig. 2.8. Since all diaphragms are well upstream of the separation point on the sphere, Reynolds number effects are weak.

From the above set of equations, flow variables can be determined

from the measured pressures (P_1, P_2, P_3, P_4) using an iterative

procedure for which a flow chart is shown in Fig. 2.9. First, assume

a value of Mach number. Values of the static and total pressure,

radial flow angle (ϕ), and pitchwise flow angle (θ) can be found from

Equations (2.1) to (2.5). The ratio of total pressure and static

pressure gives a new value for Mach number. If the new Mach number

differs from the guessed value by more than 1%, a new Mach number

guess is made and the iteration repeated until convergence is achieved.

The probe can travel across the annulus of about 5 inches in

less than 30 milliseconds, which is roughly equal to 15 ft/sec. The

traversing motion of the probe gives rise to a relative radial angle

of -2 degrees. The probe was traversed by pressurizing a piston-type

mechanism while the probe position during the traverse was recorded

as a function of test time and is plotted in Fig. 2.7. This figure

corresponds to the test in which the probe was put behind the rotor.

The pressure sensitivity of the strain gauged silicon diaphragms

may vary between tests and proper calibration is required. This is

done by venting of the facility to atmospheric pressure after each

test. Since the facility pressures are also known at the beginning of

a test, these two points can be used to determine the sensitivity for

each individual silicon diaphragm.

All silicon diaphragms used in the sphere probe are highly

temperature sensitive and they experienced thermal drift when used in

the Blowdown Tunnel. Besides using resistive compensation circuits,

cooling water is used to maintain the probe at a constant temperature.

However, these precautions do not eliminate the temperature sensitivity

completely; a compensation scheme is used to correct for thermal drift such that the time averaged total pressure as obtained from the sphere probe agrees with that from a total pressure probe, which is described in the next section.

II.C.2 Total Pressure Probe

For measurement of the fluctuating total pressure downstream of the rotor, a probe was designed and constructed with a semi-conducting strain-gauge transducer built directly into the probe head. Figure 2.10 reveals the design details of the probe. The head construction is very similar to that of usual Pilot probes. The transducer's diaphragm was recessed about one diameter from the entrance in order to make the probe insensitive to variations of the flow direction within ± 20°. This probe was mounted on a traversing mechanism which allowed the test section radius to be traversed in approximately 30 milliseconds.

The semi-conductor transducer used in the total pressure probe was less sensitive to temperature variations than those on the sphere probe. It is a Kulite transducer of type XCQ-093 series. Since the total pressure probe did not have a serious thermal drift problem, the radial variation of total pressure behind the rotor can be obtained by time averaging the signal from the total pressure probe.

II,C.3 Instrumentation Ports

A series of instrumentation ports were located on one side of the test section at the locations shown on Fig. 2.2 and Fig. 2.11. Because the rotor blade is twisted, Port 3 is about 0.5 chords down-

stream of the rotor at the tip and is only about 0.2 chords away from the trailing edge near the hub. Port 4 is at 0.4 chords downstream of the stator. The instrumentation was constructed such that any probe could be used in any port.

II.C.4 Wall Static Measurement and Other Instrumentation

Supply tank and dump tank pressures were measured using pressure transducers which have a lower frequency response and are more stable. Figure 2.4 shows the change in supply tank pressure, downstream wall static pressure at Port 7 and dump tank pressure during the complete Blowdown experiment of 600 ms. These flow quantities which have a time constant of variation on the order of one millisecond are referred to as low speed quantities. A high frequency pressure probe is also put in the casing at about 0.2 chord length (5/8") ahead of the leading edge of the rotor (Port 56) to give an indication of the shock strength upstream of the rotor. A similar measurement was also taken at mid-chord of the rotor (Port 2.5). This information is particularly useful in locating the position of the shock. The semi-conductor transducer used in the tip casing was Kulite strain-gauge transducers of type XCQ-093 series and was found to be insensitive to temperature changes. The rotor and stator angular positions, radial position of the 5-way probe and total pressure probe were also monitored during the test.

II.D Data Acquisition and Processing

All signals from various transducers were first amplified. Low speed quantities were then filtered using a low pass analog filter at

I KHz. The signal was then recorded using an on line analog to digital
converter (A/D) having seven high speed channels. Another multiplexed
channel is shared by up to 16 low speed measurements. Each high
speed channel has three different sampling rates during a complete
Blowdown test of 600 milliseconds. During the test time the sampling
rate is set at 100 KHz, which gives about 25 data points per blade
passing. The digitized data was then transmitted to a computer and
stored on the disc. All the data was then backed up onto digital
magnetic tape for permanent storage. A flow chart of data acquisition
and processing is given in Fig. 2.12.

CHAPTER III

RESULTS

III.A Description of Results

III.A.I Probe Data Behind Rotor

Wall static measurements at different locations of the test
section are plotted in Figure 2.4 for the complete Blowdown Test of
600 ms. The steady state test time begins at 90 ms and lasts for 30 ms.
At about 220 ms the flow velocity is near zero ("slosh point"). As
the pressure in the dump tank increases, a point is reached where
pressure in the dump tank equals pressure in the supply tank (Fig. 2.4).
At this point the flow stops and actually reversed its direction. A
typical variation of position of the radially traversing sphere probe
during a test is also shown in Figure 2.7. The initial blade passing
frequency is 4 KHz.

For the remainder of this section, the data will be presented as
functions of dimensionless radius, r/r_+, using the actual probe
position for each data set. The probe moves at nearly constant velocity
across the annulus, and since its radial velocity is very small
compared to the rotor or gas velocities, the abscissae may be equally
well considered proportional to time. Thus each (short) segment of
data may be considered a time history at a given radial position.

The analyzed probe data behind the rotor in absolute (i.e. non-
rotating) coordinates are shown in Figure 3.1.A-C, in which the rotor
total (P_{T2}/P_{T1}) and static pressure (P_{S2}/P_{T1}), and outlet flow angles
are plotted versus radius ratio. Figures 3.1.D-G show the Mach number
components computed from the pressures plus the measured flow angles.

Figure 3.1.A shows that there are significant total and static pressure fluctuations in the wakes. Static pressure is by no means uniform across the wake. The total pressure deflect in the wake is more pronounced near the hub that at the tip, and the flow is shown to have large blade-to-blade variations. In addition, both pressure signals show local up-spikes at some radii. The origin of these up-spikes is not fully known yet.

The data presented in Figs 3.1.B and 3.1.C show that there is a large tangential and radial flow angle variation associated with the wakes. A variation in tangential flow angle in the wake in excess of $20°$ have been observed. The variation is relatively periodic from blade-to-blade for the tangential flow angle. The radial flow angle is defined to be negative if the flow is towards the hub. Figure 3.1.C shows that there is large radial outflow associated with the wakes, hence they have a highly three-dimensional structure. Rotor wakes at $r/r_t < 0.63$ show a strong negative inflow towards the hub. Variation in radial flow angle of more than $-25°$ have been recorded, which actually exceeds the range of good probe accuracy. The large inward flows indicated near the hub are thought to be erraneous, due to the close proximity of the spherical probe head to the hub surface. Acceleration of the flow between the probe and the wall would lower P_4, relative to P_1, indicating a flow toward the hub.

The calculated Mach number components are shown in Figures 3.1.D-G. Local up-spikes in total Mach number are due to a sudden defect in static pressure shown in Fig. 3.1.A. Axial Mach number is relatively periodic and shows a large defect in the wakes. Figure 3.1.E shows

that the wake has an excess of pitchwise Mach number, which is what

one would expect for a rotor wake when observed from a stationary

reference frame.

The data as measured from a stationary reference frame can also

be transferred into a rotating reference frame. The results are

presented in this form in Fig. 3.1.H-1, in which the relative flow

angle and Mach number are plotted versus radius ratio. Figure 3.1.1

shows that the relative flow Mach number is nearly constant across

the passage and drops down in the wakes. We note large variations of

wake strength between adjacent blades as inferred from the relative

Mach number.

Since the total pressure ratio, exit flow angles and Mach number

are measured, we may use Euler's Turbine equation to calculate the

total temperature ratio. However, one must keep in mind that the

equation only applies to a streamtube in which the flow is steady in

a coordinate system relative to the rotor. Although Fig. 3.1.1

(relative Mach number) thus shows that the flow is quite steady, some

portions of the flow are unsteady on a blade passing time scale and

substantial error may result in using Euler's equation. It is not

possible with the available data to separate the effects of blade-to-

blade variation in a flow steady in the rotor frame, from unsteadiness

in the rotating frame, as they both appear as a blade-to-blade

variation in the stationary frame.

Introducing convenient non-dimensional variables into Euler's

equation yields:

$$\frac{T_{t_2}}{T_{t_0}} = 1 + \frac{r_+\omega}{\sqrt{\gamma RT_{t_0}}} (\gamma-1)(\frac{r}{r_+}) M_{\theta_2} \left[1 + \frac{\gamma-1}{2} M_2^2\right]^{-.5} \sqrt{\frac{T_{t_2}}{T_{t_0}}} \qquad (3.1)$$

Here subscript 0 refers to conditions far upstream in the supply tank and is assumed to be at the stagnation condition. Figure 3.I.J shows the computed total temperature ratio; an additional energy input in the wakes is evident. The calculated adiabatic efficiency is plotted in Fig. 3.I.K. It is observed that the local efficiency in the "inviscid" flow is only about 75% at the tip and is very near 100% for $r/r_+ > 0.8$. This is an important source of inefficiency in transonic rotor and will be further discussed later. It should be noted that the efficiency computation depends mainly on the stagnation pressure and the peripheral flow angle, which are two nearly independent data from the probe. That the efficiency is so close to unity near the hub is an important consistency check on the probe and data reduction system. It also adds confidence that the low values near the tip are meaningful, not due to an error.

Frequency spectrum of all of the above signals are also presented in Fig. 3.2.A-F. for future reference.

Time averages of several flow variables are illustrated in Figs. 3.3.A - F together with the design value and measurements taken at NASA Lewis Research Center under steady state conditions (from Reading No. 1283, Ref. 3). These two sets of data are not strictly comparable. The MIT data are from a probe traverse just behind the rotor, as described above. The NASA data on the other hand, are computed by means of a streamline-curvature theory from measurements made

behind the stator, the rotor efficiency being taken from such data
in the stator gap. Because of the low aspect ratio of this stage,
it would be reasonable to expect a considerable amount of radial
smearing of the rotor outlet profile. This is in fact very good
agreement for relative flow angle and relative Mach number (Fig. 3.3.E).
Tangential angle and tangential Mach number is also in reasonably
good agreement (Fig. 3.3.C). Of considerable importance are the
differences in efficiency near the tip and at midspan shown in Fig.
3.3.A. In the Blowdown test it is observed that there is a region of
low efficiency between r/r_t of 0.72 to 0.8, which is manifested as an
increase in total temperature at the same radius. This doesn't appear
in the steady state test where the total pressure and total temperature
are both measured behind the stator. The local deficiency behind the
rotor may diffuse while passing through the stator. The origin of
this local region of low efficiency may be the shock termination
phenomenon described in Ref. 5. Fluorescence density pictures will
help to reveal the cause of this high loss region.

Efficiency at the tip is also lower in the Blowdown Test. Since
total temperature is about the same at the tip, the difference is due
to the total pressure ratio. Streamline curvature program predicts
a higher total pressure ratio at the tip, whereas direct measurement
at the Blowdown Tunnel gave a lower reading. This point will be
further examined in Section III.A.3, whre comparison of the data behind
the stator is made.

Time averages of Mach number components are presented in Fig.
3.3.D. Results presented in Ref. 3 are data at the trailing edge of

the blade. Since there is an area reduction of about 5% between the trailing edge of the rotor and at Port 3, static pressure and Mach number can be differed. Acceleration of the flow can lead to a lower static pressure and higher total Mach number at Port 3, as indicated in Fig. 3.3.B and Fig. 3.3.D. Despite this difference, Mach number components are still in reasonably agreement with steady state testing results.

III.A.2   Results of Contour Plots of High Response Data

Another way to present the high response data is to construct contour plots of flow variables in an r-θ plane. A continuous time record of data is broken into segments of 3 blade passing periods long, and the various quantities plotted as functions of peripheral distance (rθ) and radius.

Contour plots of various flow variables in the radial plane 0.5 chords downstream of the rotor are shown in Figs. 3.4.A to 3.4.M. The location of the blade trailing edge is shown on each plot. Because the blade is highly twisted (see Fig. 2.5) the blade trailing edge will not appear as a vertical line in the r-θ plane. The blade is moving from right to left and the view corresponds to that of an observer looking upstream.

It should be emphasized that these data are in a sense taken out of context since data from several different blades at different times are combined into a single blade passage. As was previously discussed, unsteadiness does exist and is important at larger radii. Moreover, the blades are not identical and blade-to-blade variation may be different for each blade passage. Therefore, some distortion and loss

of detail in these contour plots is inevitable. Ensemble averaging

of the data will suppress the blade-to-blade variation in these

contour plots and flow features common to all blades will be emphasized

by this procedure. Averages over 5 blade passages are presented.

A contour plot of the rotor total pressure ratio is shown in

Fig. 3.4.A. Between r/r_t of 0.90 to 0.70 the flow field can be seen

to have nearly constant total pressure except near the blade wakes.

However, there are islands of high total pressure which appear in the

core flow at about r/r_t = 0.88. They start from the suction surface

and extend to about mid-passage in the core flow. These islands

of high total pressure are responsible for the localized spots of high

efficiency at the same region. No clear explanation can be offered

yet as to the origin of these high total pressure regions. Near the

hub total pressure ratio increases to about 1.72 in the core flow

while decreasing more in the wakes.

A contour plot of the rotor static pressure ratio (P_{S2}/P_{TI}) is

shown in Fig. 3.4.B. It appears that static pressure ratio is higher

at the blade wake than at the inviscid flow.

The calculated temperature ratio is plotted in Fig. 3.4.C.

Additional energy input in blade wake and in the supersonic flow regions

is evident. The rotor adiabatic efficiency is also plotted in Fig. 3.4.D.

Some important conclusions can be drawn from this Figure. At r/r_t of

about 0.86, islands of high efficiency occur in the core flow, which

result in a local maximum in the time-averaged efficiency at that

radius (see Fig. 3.3.A). At a little smaller radius (r/r_t = 0.80),

efficiency in the blade wake becomes very low, whereas the core

efficiency remains unchanged. The time-averaged efficiency has a

minimum at this radius (see Fig. 3.3.A). Thus the low efficiency that

appears about mid-way between the sonic radius and the tip has its

origin from the low efficiency in the blade wake. It is suggested

that a shock termination phenomenon described in Ref. 5 produces strong

boundary layer interaction, and resulting in the region of very low

efficiency. Near the tip the efficiency is rather uniform in θ and in

general low, both in the core flow and in the wake. No island of

low efficiency is observed at the tip. If the tip clearance effect

were the major source of low tip efficiency, it would seem that the

high velocity jet that escapes from the pressure side to the suction

side should create regions of low efficiency in the core flow due to

mixing loss. No evidence of such low efficiency islands is observed,

although the fact that the measuring plane is about 0.5 chords down-

stream may have some effect on this observation.

Contour maps of total Mach number, axial Mach number, pitchwise

Mach number and radial Mach number are included in Fig. 3.4.E through

3.4.H. Since the radial and tangential components of the Mach number

on an r-θ plane are shown, we can calculate the vorticity component

perpendicular to the r-θ plane in cylindrical coordinates.

$$\vec{\omega} = \nabla \times \vec{V}$$

$$\omega_z = \frac{V_\theta}{r} + \frac{\partial V_\theta}{\partial r} - \frac{\partial V_r}{r\partial \theta}$$

In terms of non-dimensionalized vorticity;

$$\frac{r_+\omega_z}{a} = \frac{M_\theta}{r/r_+} + \frac{\Delta M_\theta}{\Delta r/r_+} - \frac{1}{r/r_+}\frac{\Delta M_r}{\Delta\theta}$$

The result is presented in Fig. 3.4.I. Notice a region of strong streamwise vorticity exists at the trailing edge near the sonic radius. This seems to agree with the model described in Ref. 5. It is argued that the sharp pressure gradient produced by the shock termination phenomenon would lead to strong radial flows in the boundary layer, which is unable to withstand the pressure gradients produced in the transonic inviscid flow. The consequent shear would appear in the form of a streamwise vortex.

Finally, contour maps of tangential flow angle, radial flow angle, relative Mach number and relative flow angle are included as Fig. 3.4.J through 3.4.M for future reference. The large disturbances concentrated at blade passing frequency are clearly displayed in the relative Mach number and tangential angle contour plots (Figs. 3.4.I and 3.4.J). Also approximate location of blade trailing edge can easily be seen.

III.A.3 Results of Probe Survey Behind Stator

The 5-way probe was also traversed across the annulus behind the stator at Port 4. Time averaged total pressure ratio is illustrated in Fig. 3.5, together with the design value and steady state test result from NASA Lewis Research Center. Excellent agreement was observed in total pressure between the two tests. In all cases, total pressure ratio is decreasing towards the hub, due to increasing stator losses. Unlike the comparison made between NASA steady state test

and MIT Blowdown test for the rotor, total pressure behind the stator was actually measured directly and no streamline curvature program is involved. Thus at the station where measurements were actually taken for both tests, results are in good agreement. However, when the total pressure ratio was back calculated using a streamline curvature program to the station behind the rotor, a discrepancy was found. The directly measured total pressure ratio from the Blowdown Tunnel was about 6-7% lower than that calculated from NASA result at the tip. This leads to a lower efficiency at the tip for the rotor. It is difficult to determine which answer is correct. But aside from blockage effects, the direct measurement should be more accurate than using streamline curvature program to calculate the flow field behind the rotor.

A comparison for the time averaged total Mach number behind the stator is presented in Fig. 3.6. It is observed that the radially averaged total Mach number measured in the Blowdown Tunnel is in very good agreement with design and NASA steady state results.

Blade-to-blade variation in the flow field behind the stator are shown in Fig. 3.7.A through Fig. 3.8.E, in which various flow variables are plotted against radius ratio. Fig. 3.7.A to Fig. 3.7.E correspond to measurements at a plane which is only 0.4 stator chords downstream of the stator (Port 4). Figure 3.8.A to 3.8.E are from Port 7, which is about 1.5 stator chords downstream of the stator.

From Fig. 3.7.A, one can clearly see the passage of a stator wake, which appears as a minimum in total pressure and a small maximum in static pressures. Similar behavior in static pressure is found in the rotor wake, as can be seen from the contour plot of Fig. 3.4.B. Both total and static pressures are nearly constant in the stator outlet

"inviscid" flow. Because of the close proximity of the probe to the stator trailing edge, the stator wake is narrow and one of the diaphragms on the probe may reside in the stator wake whereas other diaphragms may still be in the inviscid region for several rotor passing periods. This insufficient spatial resolution of the probe results in erroneous measurements of the flow angles and pressures, thus give rise to the "spikes" in the wake region for the tangential and radial angles as well as the Mach number components. It is observed that the stator wake is deeper at the hub than at the tip. This measurement is consistent with the design intent and the measurements taken at NASA Lewis Research Center. In both cases, stator loss increases towards the hub.

The data in the mid-passage shows the state of the rotor wakes as they are convected out of the stator passage. One interesting feature is that near the tip, the rotor wakes as indicated by the total pressure, Mach number and radial flow angle still exist nearly undiminished in the flow downstream of the stator. However, close to the hub some of the rotor wakes seem to have been filled up and are hardly distinguishable.

Similar data from measurement at about 1.5 stator chords down-stream of the stator (Port 7) are shown in Fig. 3.8.A to 3.8.E. Referring back to Fig. 2.2, there is an area reduction of about 6% between Port 4 and Port 7. Moreover, Port 7 is only at 7.94 cm (3-1/8") from the throttle orifice. These two effects greatly accelerate the flow, which gives a higher Mach number and lower static pressure.

Comparison between data taken with the probe behind the rotor, 0.4 chords behind the stator and 1.5 stator chords behind the stator at the corresponding radii are presented from Fig. 3.9.A to Fig. 3.9.E. Here total and static pressure, tangential and radial flow angles and total Mach number at the corresponding radius ($r/r_+ = 0.77$) are plotted; with data taken out in between the stator gap (core flow). It is found that near the tip, the rotor wakes appear nearly undiminished in the exit of the stator, and remain so in the annular duct behind the stator. The stator wakes decay very rapidly so that at a distance of 1.5 stator chords behind they have virtually ceased to exist.

III.A.4. Results of Wall Static Measurements

High frequency pressure transducers were mounted in the casing in locations as shown in Fig. 2.11. Fluctuations of static pressure on those transducers on a blade-to-blade time scale were presented in Fig. 3.10 - 3.13. Because of limitations of the data acquisition system, high frequency wall static measurements at different locations along the test section were taken from more than one test, but with the rotor running at exactly the same conditions.

In Fig. 3.10 all signals from Port 2, Port 56 and Port 2.5 are plotted on the same scale so that a comparison between all three signals can be made. It is evident from the top two signals that the shock waves rapidly attenuate as they propagate upstream from the rotor. The bottom trace shows a strong low pressure region at each blade, evidently due to a tip vortex.

Each signal is also plotted individually. Fig. 3.11.A is the

signal from Port 2, which is about 0.4 rotor chords from the leading edge of the rotor. Fig. 3.11.B is the power spectral density of the same signal.

Figure 3.12.A is the measurement taken at Port 56, which is at 5/8" upstream from the leading edge of the rotor. An inlet relative Mach number of 1.14 is inferred basing on the ratio of the static pressure across a normal shock. It may seem low when compared to the design value of 1.38, however we must account for the existence of the boundary layers on the casing. Moreover, the measurement was taken 5/8" upstream from the leading edge. Besides, the low shock need not be normal at the tip, thus the inlet relative Mach number could well be higher than 1.14. In Fig. 3.12.B the signal at Port 56 from three successive rotations of the rotor is plotted on the same page. Notice one can identify some blades from their relative shock strength. If desired, this signal can be used as a measure of the rotational speed of the rotor. The small upspike between each blade passing has an unknown origin. The power spectral density of this signal is plotted in Fig. 3.12.C.

The final wall static measurement was taken at Port 2.5, which is at about mid-chord in the rotor passage. Figure 3.13.A shows the blade-to-blade variation of this signal. The sharp decrease in static pressure may be due to the tip vortex associated with each blade. Notice the magnitude varies slightly from blade-to-blade. This may be due to the variation of tip clearance from one blade to another. Theoretically this signal can be used to predict the location of the passage shock. However, the highly unsteady nature of the flow made this almost impossible. In Fig. 3.13.B, data from three successive

rotations of the rotor are plotted on the same page. Notice how the

pressure field between any two blades changes from one rotation to

another. Also there is a large variation from blade-to-blade. This

variation strongly suggests an unsteady shock pattern. An unstable

oscillating shock system may exist in the passage, which gives rise

to the large fluctuation in the inviscid flow from blade-to-blade.

Figure 3.13.C is a comparison between the original signals and a

5-cycle ensemble average of the same signals.

Due to relative motion of this moving shock, the rotor shocks

may see a higher approaching Mach number than they would if the

shocks were stationary. Increasing Mach number can increase

shock losses significantly, thus giving rise to a lower efficiency

in the inviscid core flow. It is still unclear at this point whether

the unsteady flow is an intrinsic feature of transonic compressors,

or whether it is due to fluctuations in the quasi-steady flow generated

in the Blowdown Tunnel.

III.B. Discussion of Results

III.B.1 Mass Flow Determination and Mach Number Measurements

Based on the rate of change of supply tank pressure, the

corrected mass flow of the rotor with respect to air is calculated to

be 33.0 Kg/s. This agrees very well with the design value of

33.248 Kg/s. The rate of change of supply tank pressure was determined

by curve fitting an exponentially decaying function to the original

measured supply tank pressure. This avoided differentiating the

original data and thus gave more accurate results. Basing on this

method, corrected mass flow changed by less than 1% during the test time.

By traversing the 5-way probe upstream of the rotor at Port 1, it was found that the inlet static pressure is not uniform across the annulus, being lower near the hub. Measurements from the total pressure probe at different radii showed that the inlet total pressure is uniform. Thus the non-uniformity in static pressure will give a variation in inlet Mach number along the radius. This implies the rotor is pumping harder near the hub, thus drawing more fluid and hence higher Mach number. According to Ref. 4, mass flow can also be determined by wall static pressure measurements if the flow is one-dimensional. However, since static pressure is not uniform across the annulus, mass flow determination based on casing static pressure measurement either upstream or downstream could give misleading results.

Mass flow can also be calculated from the integration of the flow quantities measured by the 5-way probe along the radius. However, the accuracy of determining mass flow by this method relies strongly on the Mach number measured, which is also a function of the static pressure. Since the calibration for static pressure strongly depends on the geometry of the probe, a slight difference between the model probe used for calibration and the actual probe can lead to a large error. It was decided to calibrate the actual probe by shifting the calibration curve for static pressure ($K_{P_{2,3}}$) such that it gives the same mass flow as determined by the rate of change of supply tank pressure. Based on this method, the corrected mass flow was determined to be 33.2 Kg/s at Port 3 (behind rotor) and 33.9 Kg/s at Port 4

(behind stator).

An important consistancy check on the 5-way probe and the data
reduction program is in the torque balance calculation on the rotor.
The torque acting on the rotor should balance with the changes in the
fluid's angular momentum. The torque acting on the rotor calculated
from the rate at which the rotor slows down as it does work on the
fluid during the test time is 303.0 N-m (223.5 lb-ft) and from the
change in the angular momentum across the rotor the torque is
calculated to be 301.1 N-m (222.1 lb-ft). The close agreement of
the two numbers adds confidence to the data measured by the 5-way
probe.

III.B.2 Rotor Overall Performance

The efficiency of the rotor can be calculated from the rotor
deceleration and mass flow. The moment of inertia of all rotating
parts was determined by a torsional pendulum technique to be 0.293 $Kg-m^2$
(0.216 $lb-ft-sec^2$). Rotor deceleration was measured by a one pulse-
per-revolution tachometer. Using

$$\dot{m} \ C_p \ \Delta T_T = I \ \omega \ \frac{d\omega}{dt}$$

where $\dot{m}$ = actual mass flow, C_p = gas constant for Ar-Fe, I = moment
of inertia of rotor, ω = angular speed, $d\omega/dt$ = angular acceleration.
The overall temperature ratio across the rotor was determined to be
1.174. From the total pressure probe, the rotor time-averaged total
pressure ratio was measured to be 1.677. Thus giving an average
total-to-total isentropic efficiency of 89.5%. This agrees very well
with the measurement taken at NASA Lewis Research Center, which gives

a rotor peak adiabatic efficiency of 90.6%.

Although the time-resolved efficiency can be calculated by using Euler's equation, this method involves several approximations. Eq. (3.1) was reproduced here.

$$\frac{T_{t_2}}{T_{t_0}} = 1 + \frac{r_+\omega}{\sqrt{\gamma RT_{t_0}}} (\gamma-1)(\frac{r}{r_+}) M_{\theta_2} \left[1 + \frac{\gamma-1}{2} M_2^2\right]^{-.5} \sqrt{\frac{T_{t_2}}{T_{t_0}}} \qquad (3.1)$$

Careful examination of this equation reveals that M_2 has a second order effect on the total temperature ratio calculated. However, both M_θ and r/r_+ have a strong influence on the calculated total temperature ratio. The probe position (r/r_+) can be measured accurately during the experiment. However, the tangential Mach number, which depends on the total Mach number and tangential flow angle, can hardly be measured with an accuracy better than 3-5%. One reason is that the thermal drift problem can offset the D-C level of the total Mach number. More importantly, the tangential flow angle measured depends on the aerodynamics center of the sphere probe, which may differ from the geometrical center by one or two degrees due to asymmetry. It was found that the efficiency calculated using Eq. (3.1) is very sensitive to the tangential angle. One degree in tangential flow angle corresponds to almost 1% in efficiency. The level of the time averaged efficiency plot showed in Fig. 3.3.A was adjusted by varying the effective probe angle so as to give an overall efficiency of about 90%, as determined from rotor deceleration and mass flow calculation.

Other than the uncertainty in measurements of tangential Mach number, the application of Euler's equation to the highly unsteady flow is also questionable. In particular, for the portion of flow which

has undergone extensive viscous interaction; such as the hub and tip casing boundary layers and the blade wakes; the Euler's equation could be substantially in error, and this should be kept in mind when interpreting the results. Islands of efficiency higher than 100% in Fig. 3.4.D could be due to the above mentioned effects.

When interpreting probe data near the tip, we must also account for the influence of the outer casing on the probe measurement. Close to the casing the probe will no longer act as attached to a thin stem, but would rather appear as attached to a big block. Moreover, the flow field created by the cavity from which the probe emerges can also affect the data near the tip to a certain extent.

III.B.3 Stage Overall Performance

From the total pressure probe, the stage has an average total pressure ratio of 1.658. After accounting for the rotation of the stator, the overall total temperature ratio across the stage was determined to be 1.181, thus giving an average efficiency of 86.2%. This is based on radially averaging the circumferentially averaged flow behind the stator, including the stator wakes. The stage efficiency is calculated by finding the stage total temperature from the rotor deceleration and then accounting for the small stator rotation. Corresponding measurements at NASA Lewis Research Center have given a peak stage efficiency of 87.0%.

A comparison between measurements from the 5-way probe and the total pressure probe at different radii was presented in Fig. 3.14.A & B . Here the total pressure ratio and the corresponding power spectral density of each signal are plotted. Basic features of the flow field

are essentially the same in both measurements. The flow is highly

unsteady at a higher radius. At a lower radius, blade wake is more

clearly defined. Similarity in both signals adds confidence to the

measurements taken using the 5-way probe.

One of the more important results of this work is presented in

Fig. 3.15. Here the time-averaged efficiency in the inviscid core

flow as estimated from Fig. 3.1.K is separated from the efficiency

in wake flow. The difference between this core flow efficiency and

the overall efficiency is interpreted as a viscous profile loss and

is plotted in Fig. 3.15 as the half filled circles. The sum of these

plus shock losses based on normal shocks at the inlet relative Mach

number are also plotted, as the triangular points. One observation

is that the overall efficiency is well below the estimate based on

the sum of normal shock and profile losses, that is normal shock

losses do not account for the core flow inefficiency. Profile losses

are relatively small, accounting for only about 4% of the inefficiency,

and are relatively constant along the radius. Near the tip, normal

shock losses only account for less than 5% of the inefficiency. As

can be seen, there is at least a 5% increment in overall rotor or

stage inefficiency not explained by these mechanisms, with a much la-

rger discrepancy near the tip. Thus it is important to understand

the mechanisms which control the losses in the tip region.

CHAPTER IV

CONCLUSIONS

An investigation of the flow field produced by a transonic compressor stage has been completed. This study included time and space resolved flow measurements behind the rotor and stator, as well as tip casing wall static pressure measurements. Spatial and temporal resolution achieved by the 5-way probe was sufficient to determine velocity components and pressures inside individual blade wakes and in the surrounding flow. Large variations in both tangential and radial flow angles in the rotor wakes were observed, showing the highly three-dimensional structure of rotor wakes which is very different from two-dimensional models. Five-way probe data also showed that the flow is highly unsteady and has large blade-to-blade variation. Contour plot in an r-θ plane indicates a strong streamwise vortex near the sonic radius, which can represent a region of high losses.

Time and space resolved measurements of flow behind a row of stator blades downstream of the transonic rotor show that there is a significant total pressure defect associated with stator wakes. A small maximum in static pressure was also observed in the stator wake. The wakes from the rotor exist nearly undiminished in the exit flow from the stator and remain so in the annular duct behind the stator. The stator wakes decay very rapidly so that at a distance of 1.5 stator chords behind the stator they have virtually ceased to exist.

Wall static measurements from high frequency wall static trans-ducers at mid-chord of the rotor strongly suggests a highly unsteady shock pattern in the rotor passage. This could result in higher shock

relative Mach numbers which could increase shock losses significantly.
Though sufficient evidence cannot be obtained in the Blowdown Tunnel
to confirm this observation, this unstable oscillating shock system
can represent an important source of losses and deserve further
investigation.

Although the 5-way probe has excellent frequency response, it
is limited by its relative large size. Besides the blockage effects,
the probe also lacks sufficient spatial resolution to resolve data
inside the rotor wakes. These problems can be lessened somewhat if the
present probe can be reduced in size by a factor of two.

The viability of the Blowdown Compressor and its associated
instrumentation for providing the required experimental data has
been fully demonstrated. However, developing a technique to measure
total temperature becomes very desirable for this facility. As reported,
determining efficiency based on Euler's equation is by no means
accurate. Only with a very precise measurement of total temperture
can the performance of the rotor be fully evaluated. Since efficiency
is the most sensitive indicator of the quality of the aerodyanmic
design of the compressor, it is important to develop a technique to
measure the total temperature.
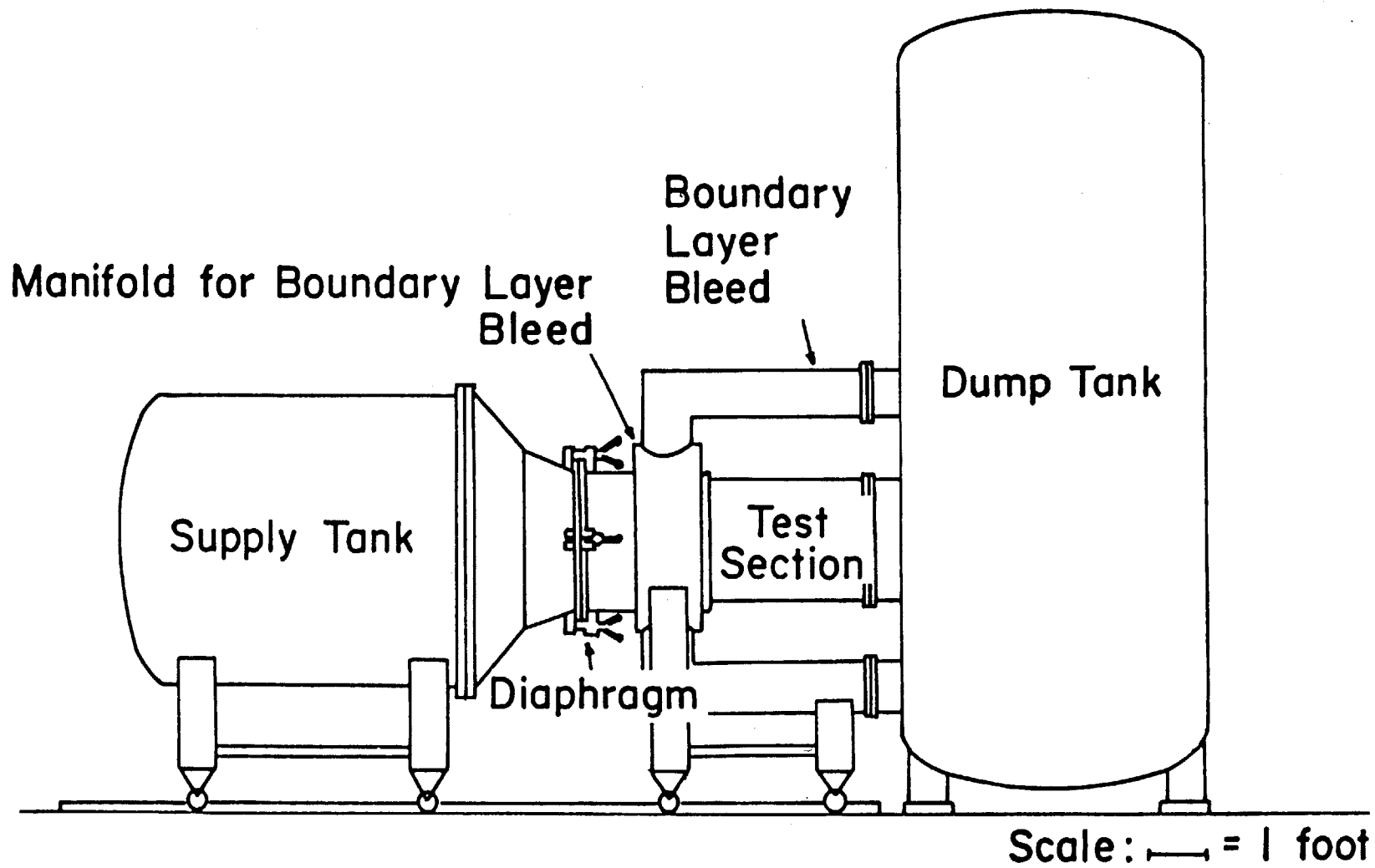
FIGURE 2.1 SCALE DRAWING OF BLOWDOWN COMPRESSOR FACILITY.

INSTRUMENTATION PORTS
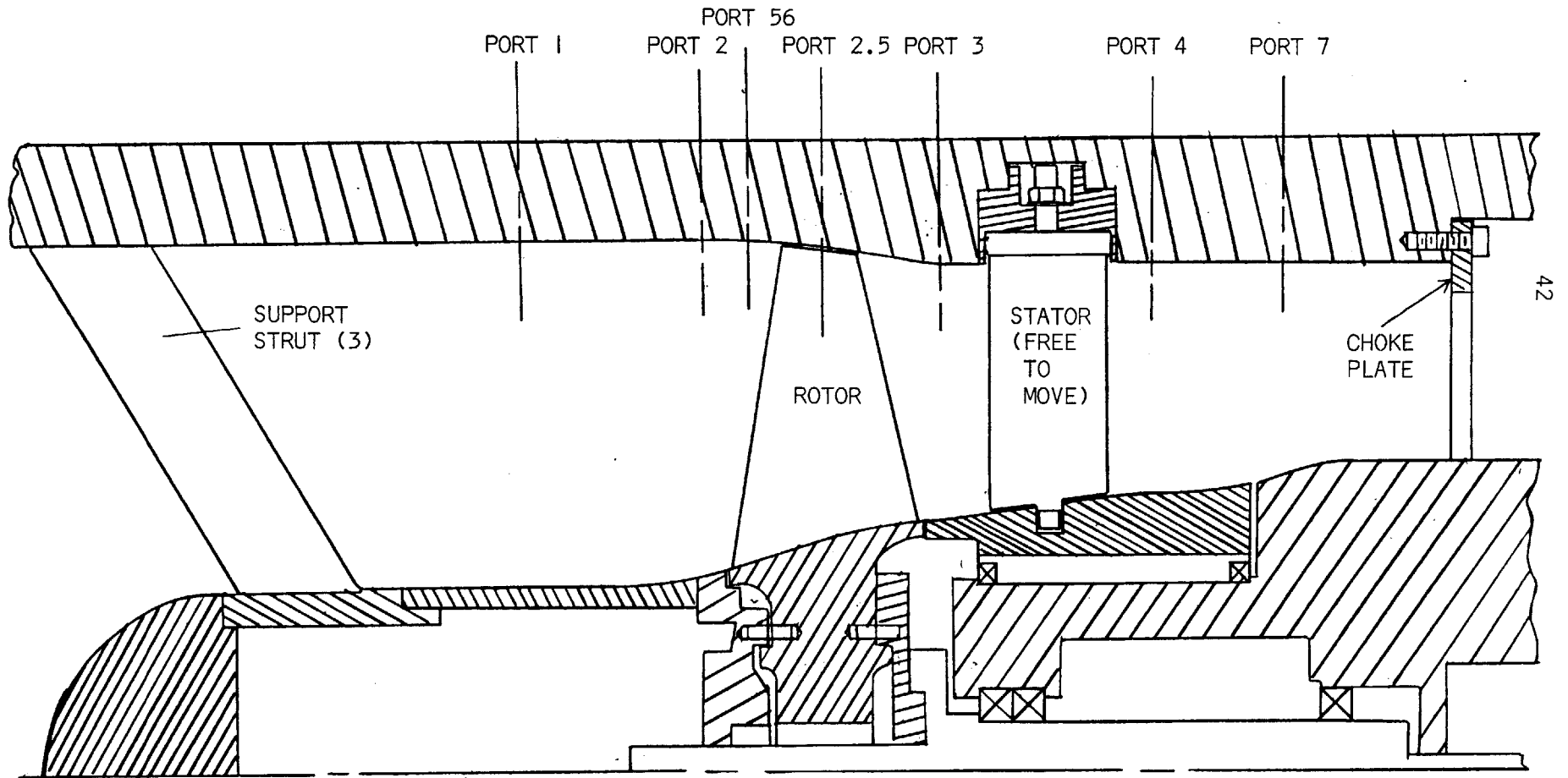
FIGURE 2.2 SCALE DRAWING OF TEST SECTION SHOWING LOCATION OF INSTRUMENTATION PORTS AND STAGE FLOW PATH.
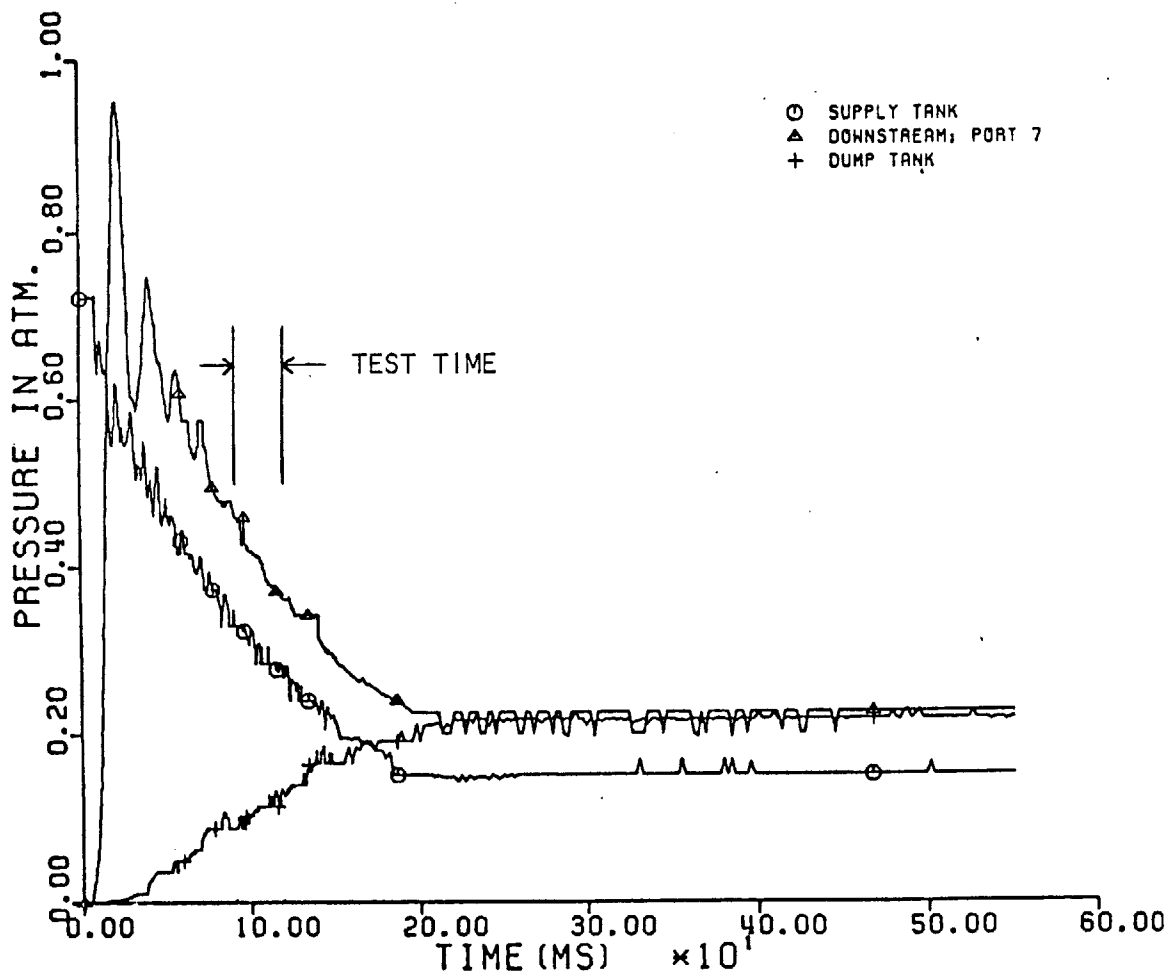
FIGURE 2.4   PRESSURE VARIATION IN BLOWDOWN FACILITY AT
DIFFERENT LOCATIONS
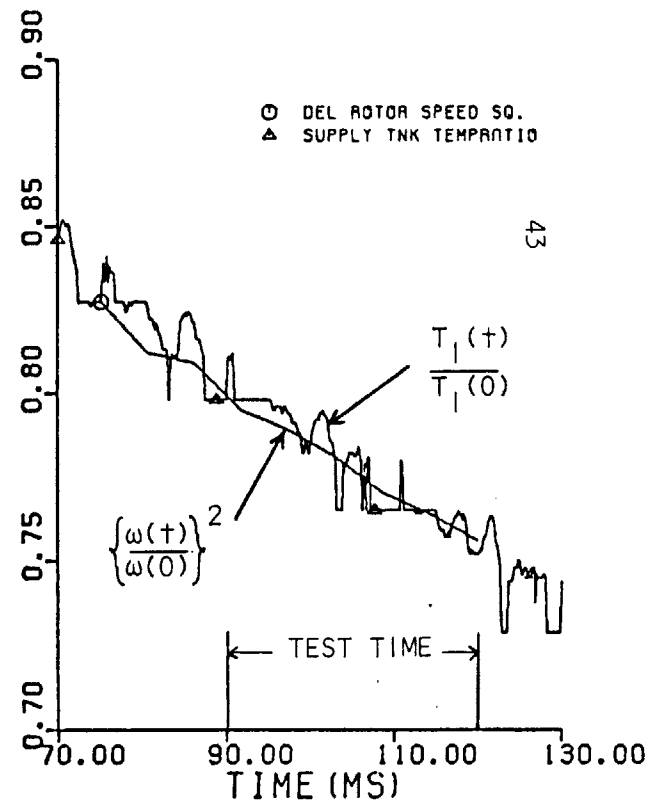
FIGURE 2.3   MATCHING BETWEEN ROTOR
DECELERATION AND CHANGE IN SUPPLY
TANK TEMPERATURE

FLOW

ROTATION

LEADING
EDGE
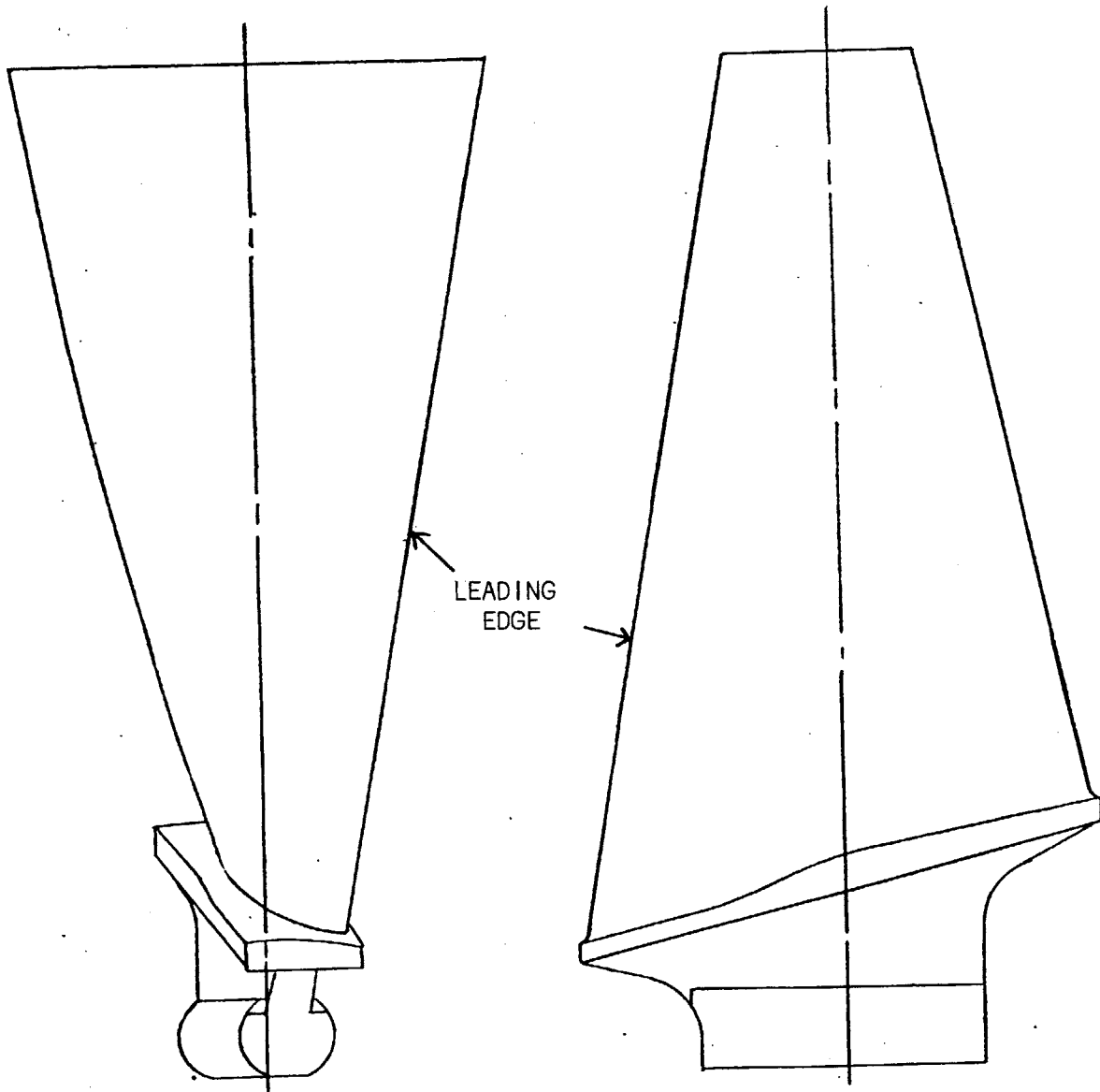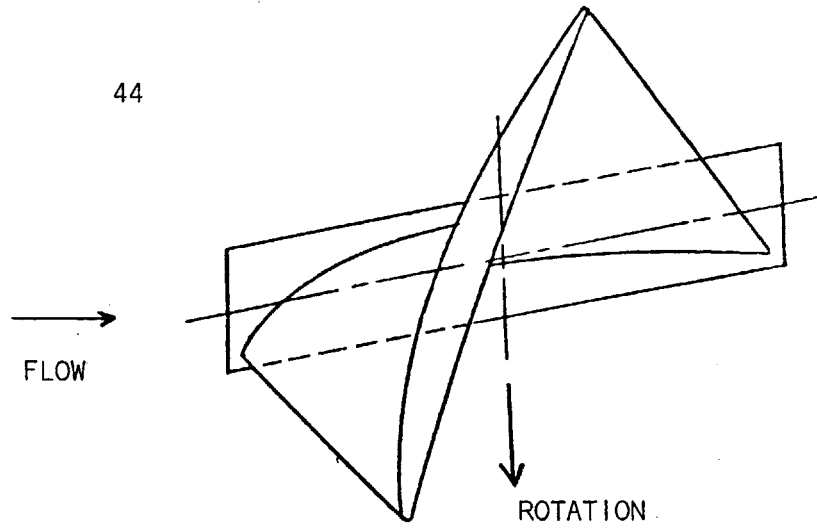
FIGURE 2.5   SCALE DRAWING OF ROTOR BLADE SHAPE
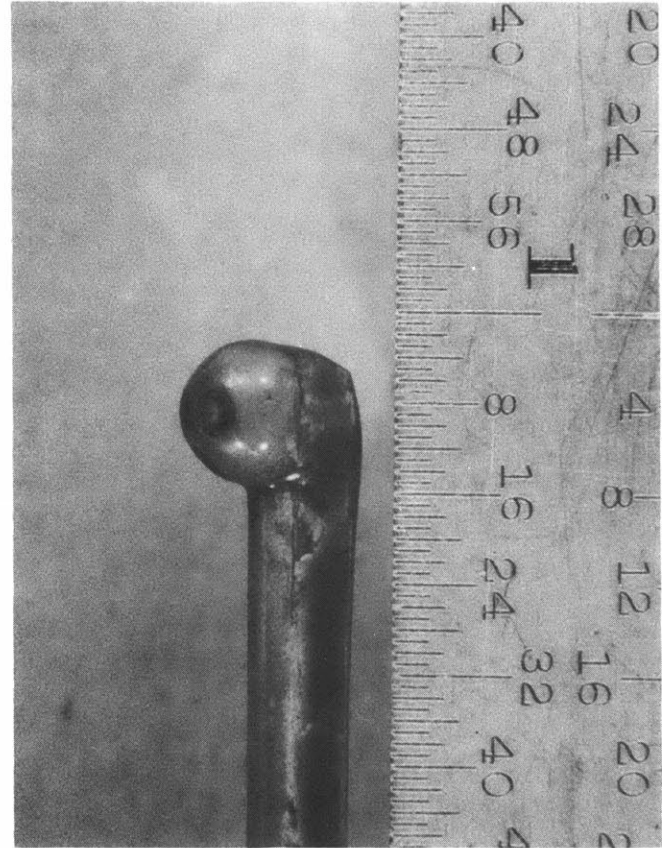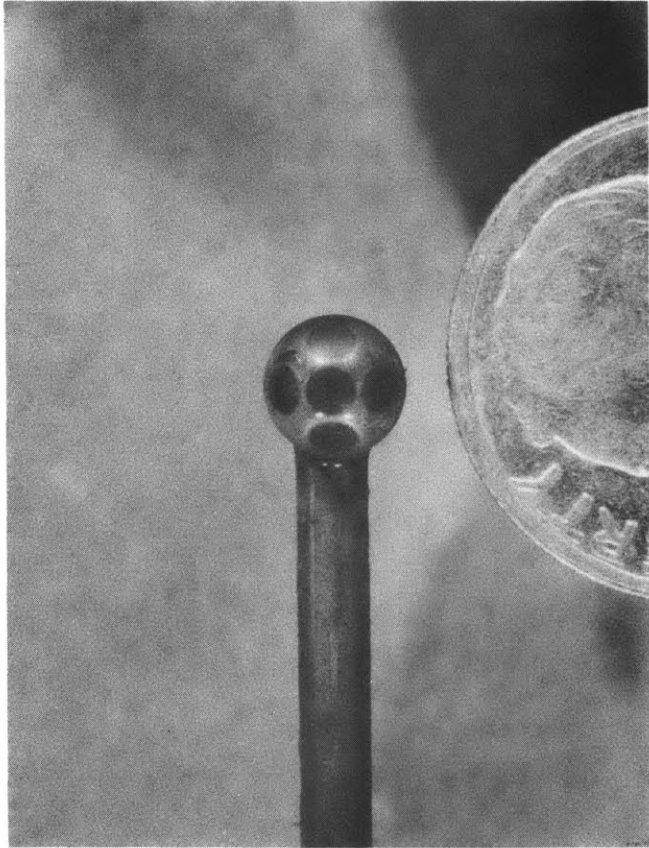
Figure 2.6.A   The 5-Way Probe
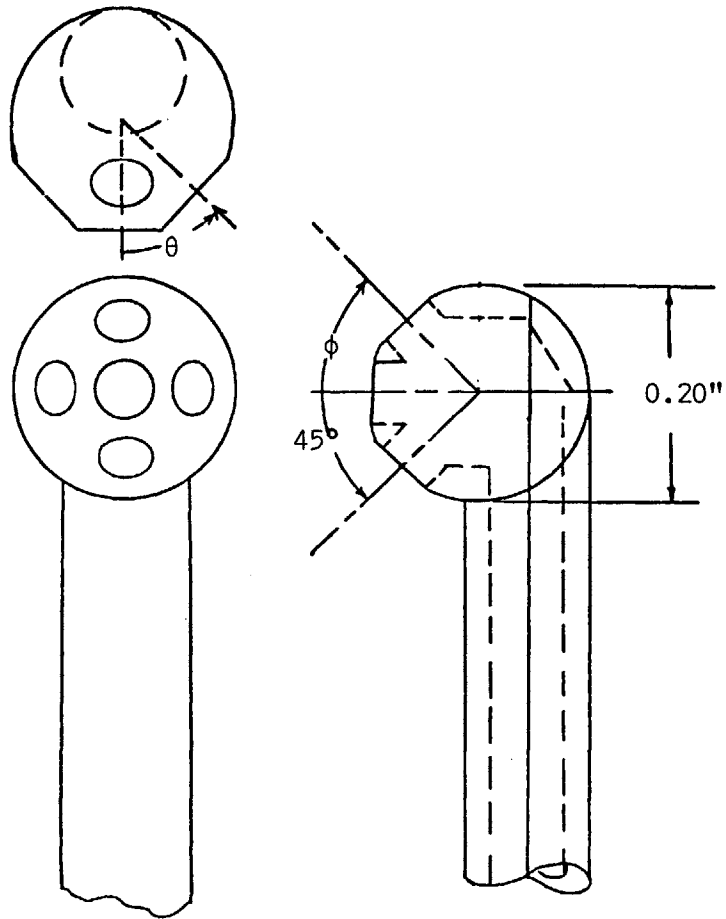
FIGURE 2.6.B   SKETCH OF 5-WAY PROBE SHOWING AIR
ANGLE DEFINITION.
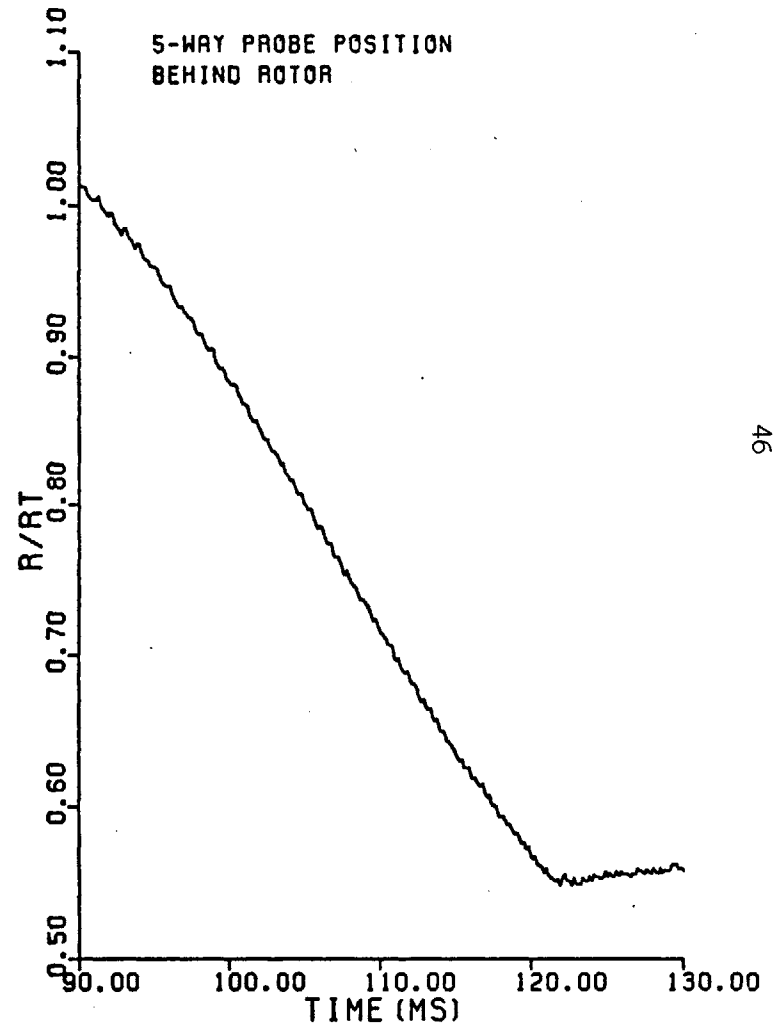
FIGURE 2.7   5-WAY PROBE POSITION VS. TIME
DURING THE TRAVERSE (PROBE BEHIND ROTOR)
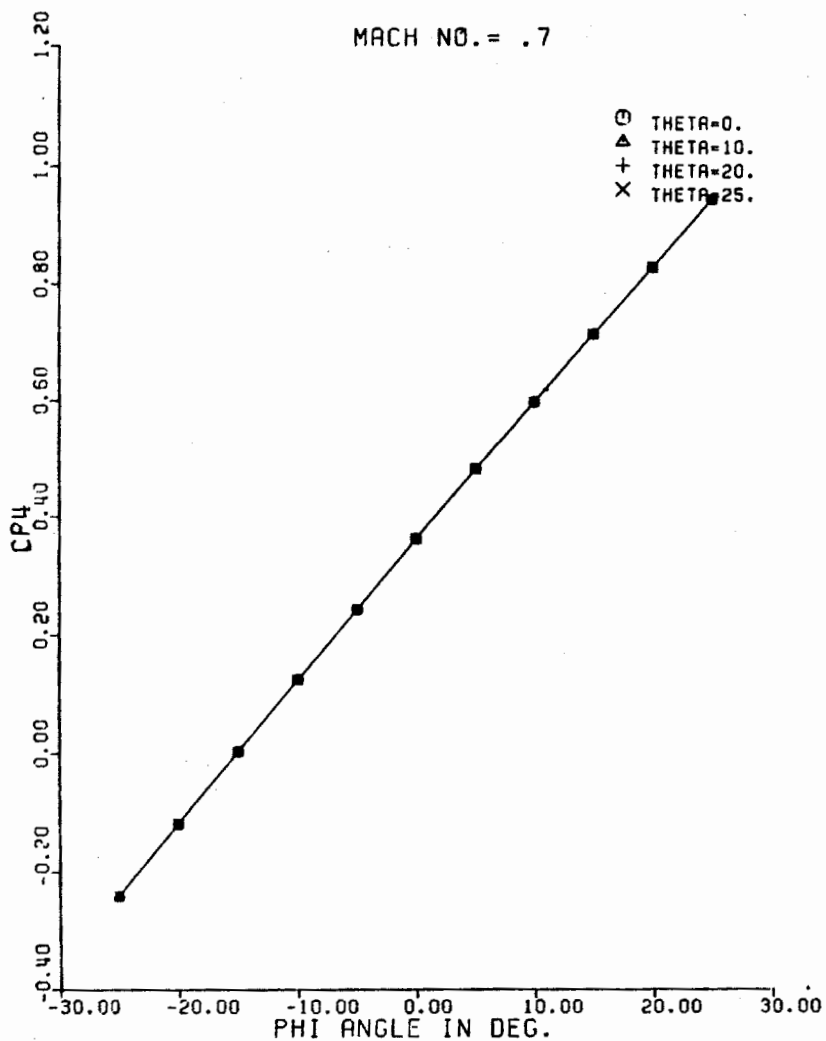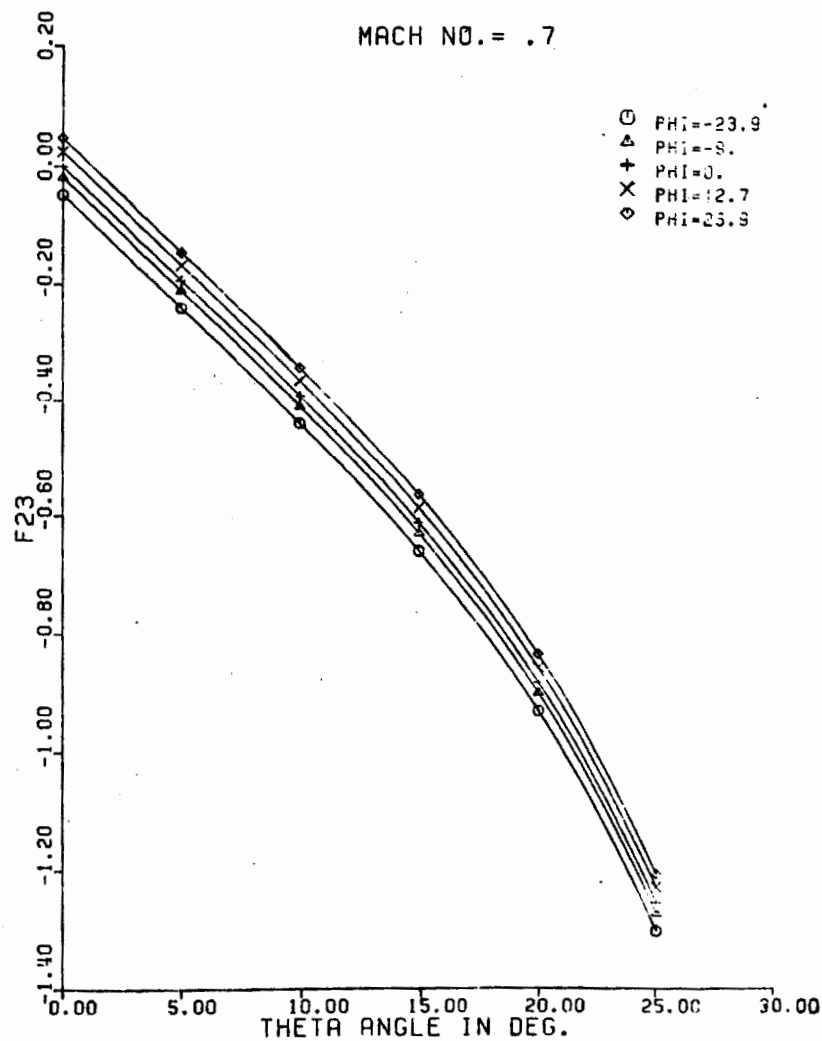
FIGURE 2.8.A 5-WAY PROBE CALIBRATION FOR RADIAL (C_{P4}) & TANGENTIAL (F_{23}) FLOW ANGLES.
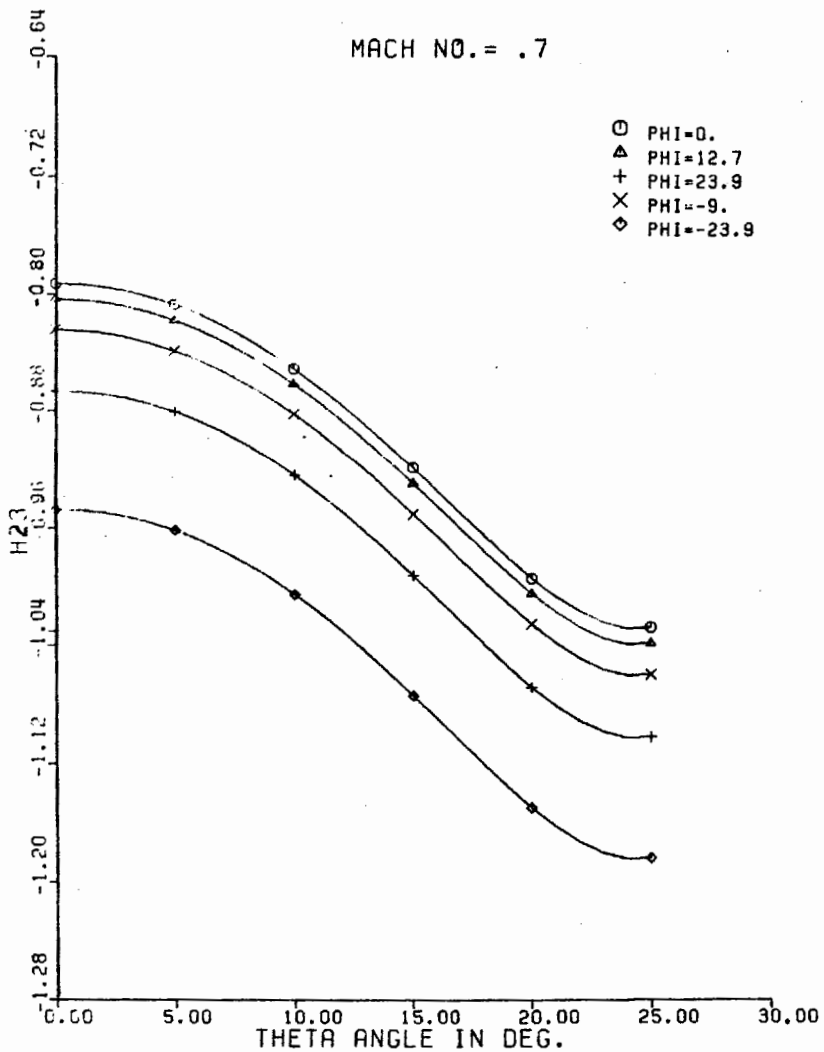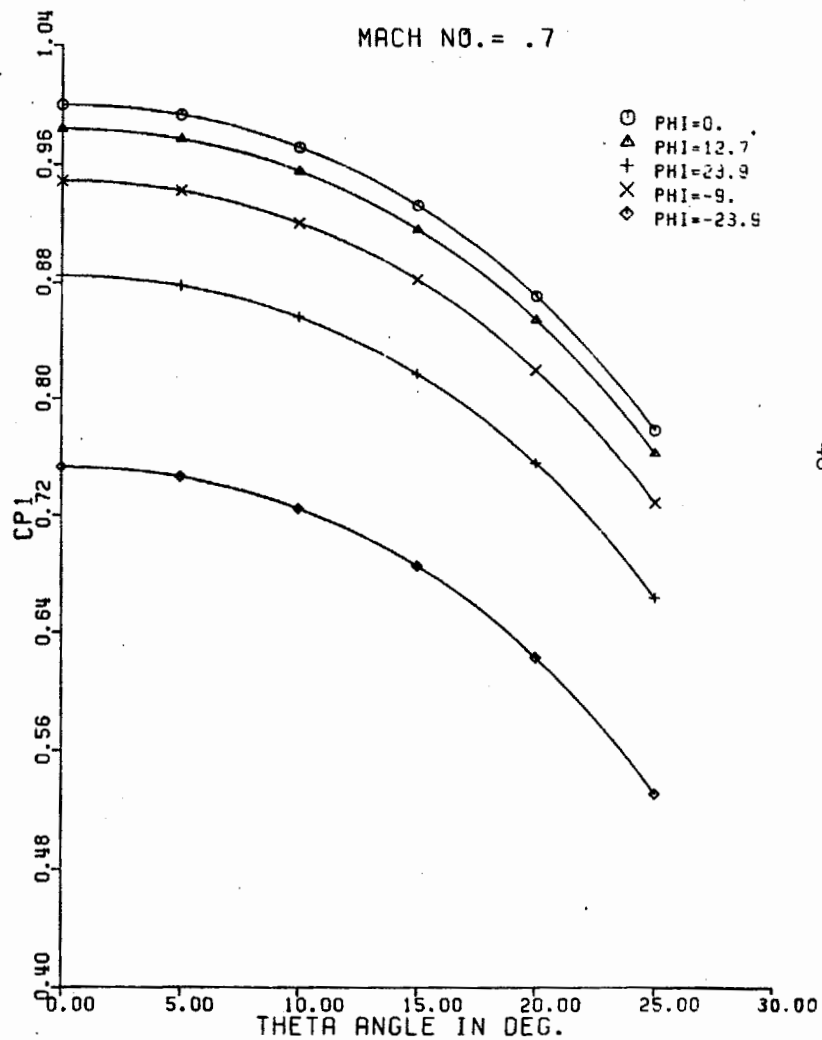
FIGURE 2.8.B   5-WAY PROBE CALIBRATION FOR TOTAL PRESSURE RECOVERY.
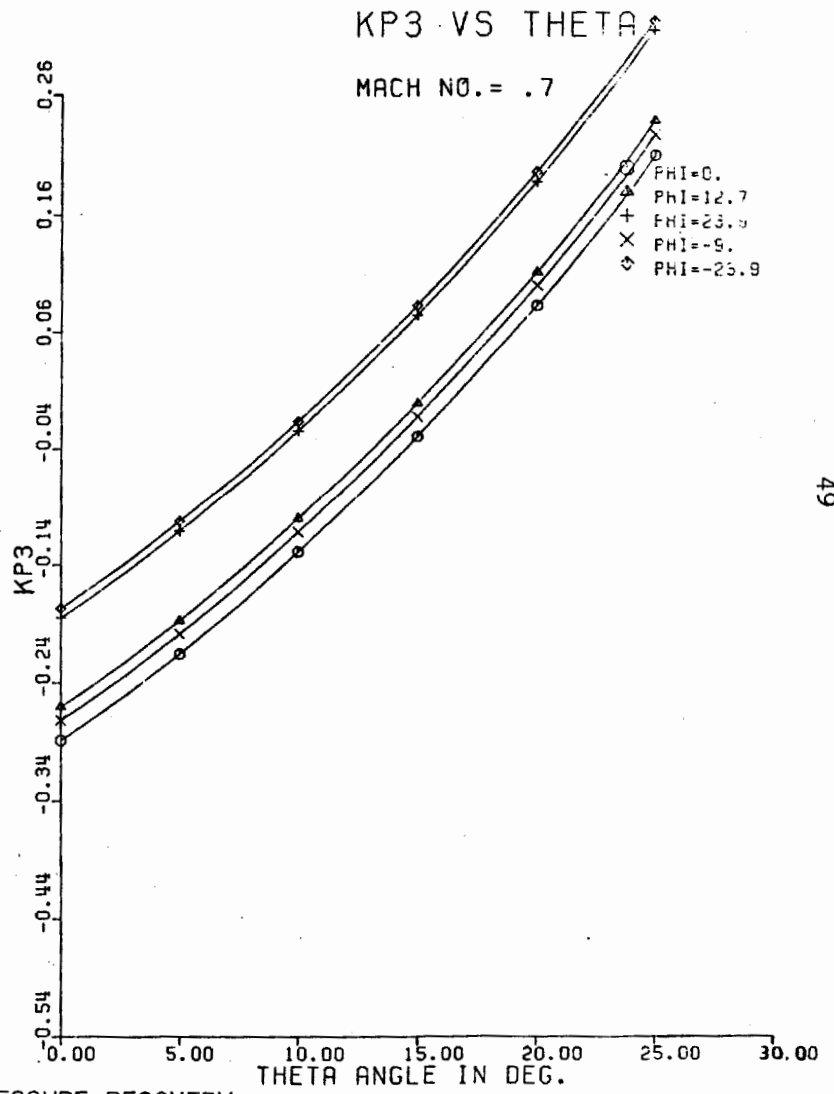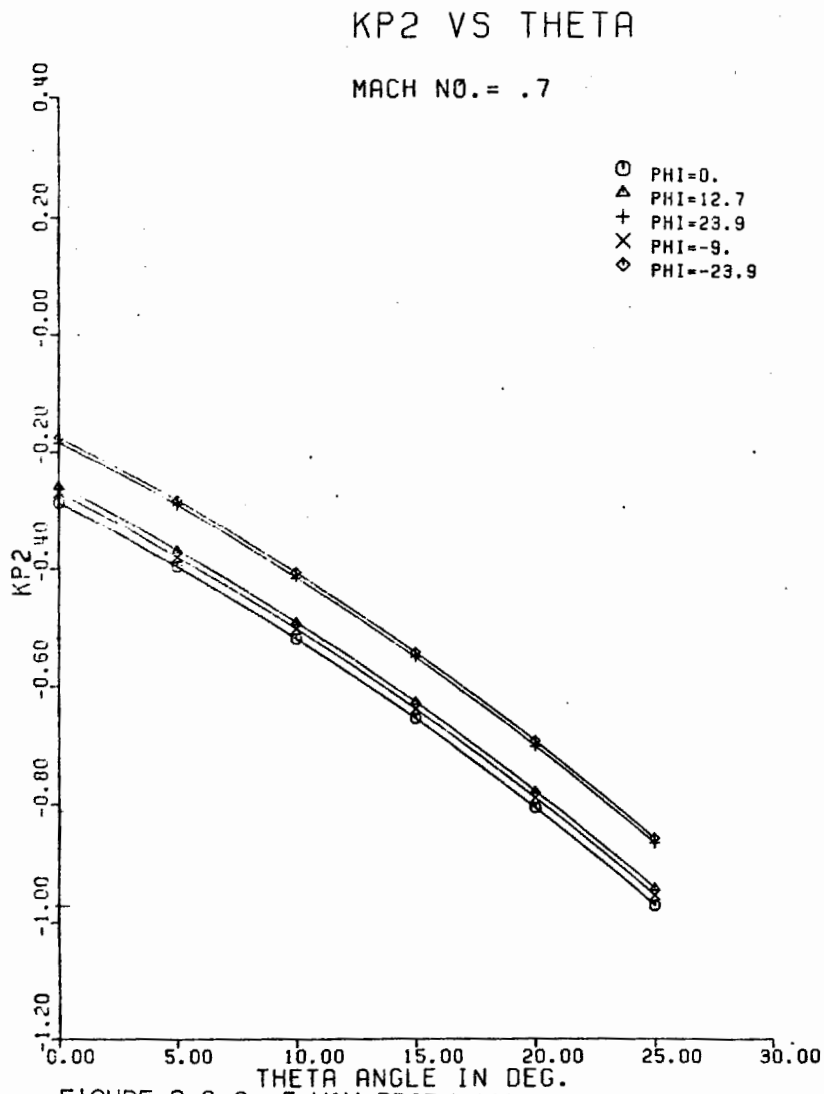
FIGURE 2.8.C 5-WAY PROBE CALIBRATION FOR STATIC PRESSURE RECOVERY

P_1, P_2, P_3, P_4

GUESS MACH NO.

GUESS TOTAL PRESSURE

GUESS STATIC PRESSURE

DETERMINE ϕ FROM C_{p4}

DETERMINE θ FROM F_{23}

DETERMINE P_S FROM K_{p2} AND/OR K_{p3}

DETERMINE P_T FROM C_{p1} and H_{23}

DO P_T & P_S CONVERGE? NO

YES

CALCULATE M, M_x, M_ϕ, M_θ

DOES M CONVERGE? NO

YES

P_T, P_S, θ, ϕ, M, M_ϕ, M_θ, M_x
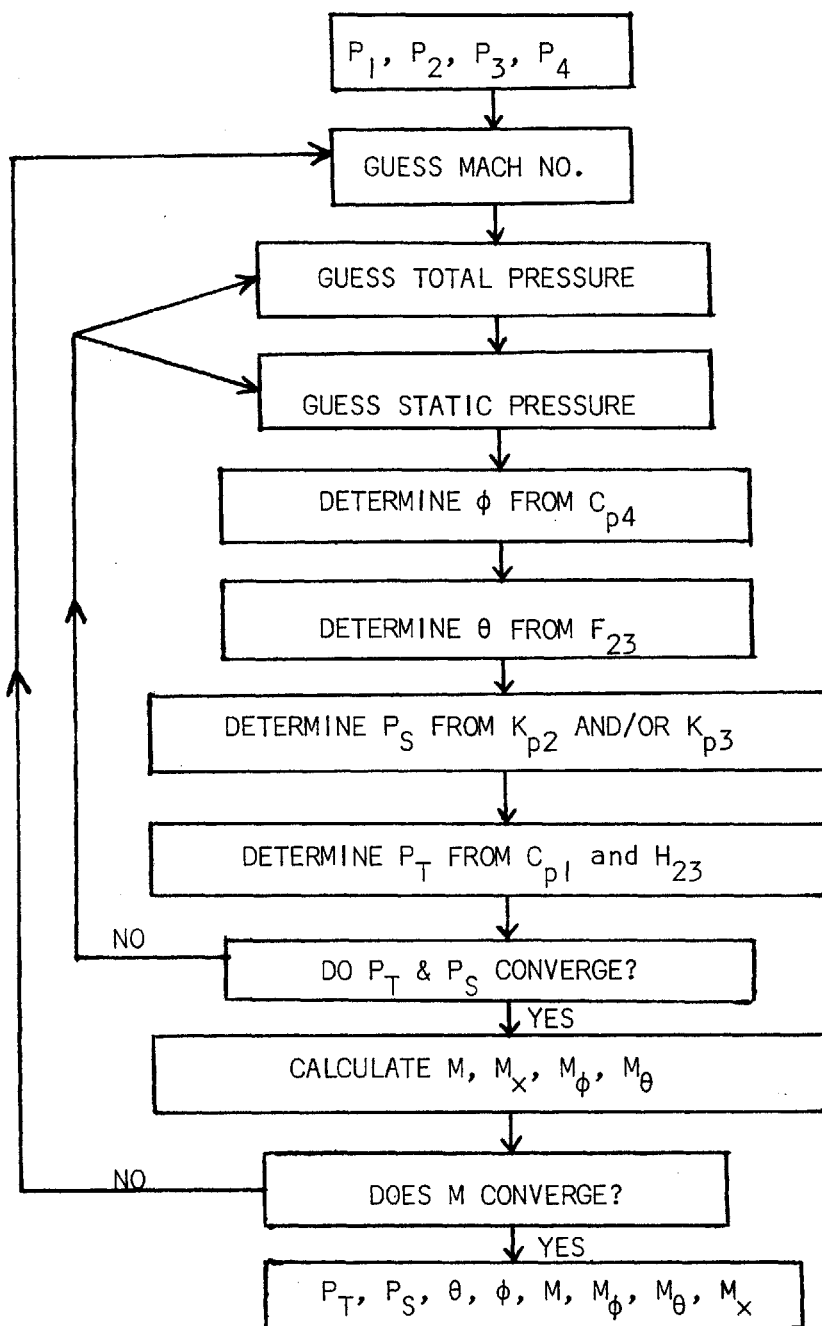
FIGURE 2.9   FLOW CHART FOR 5-WAY PROBE DATA REDUCTION
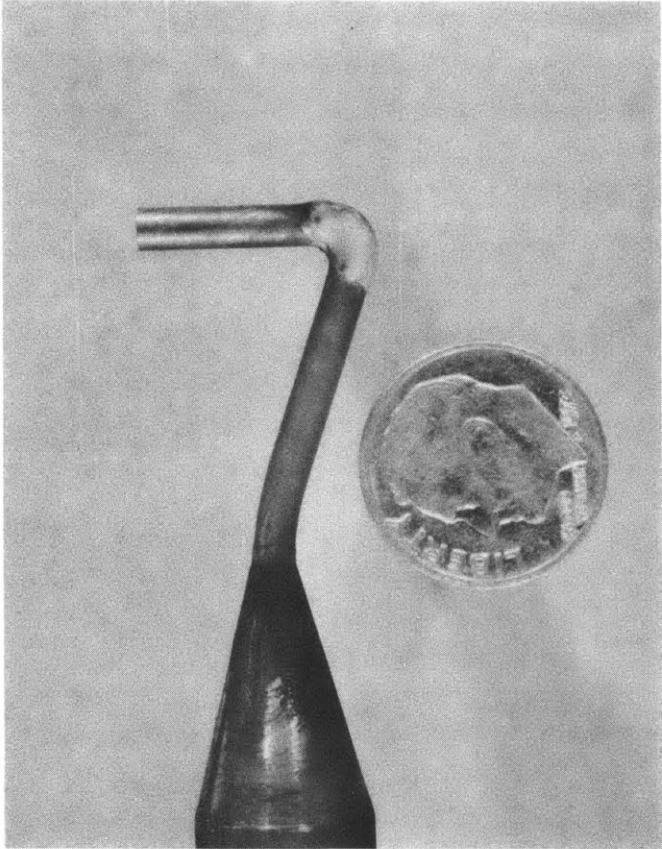
Kulite Transducer
Model CQ093

0.12"

Detail "A"

A

Scale 1:1
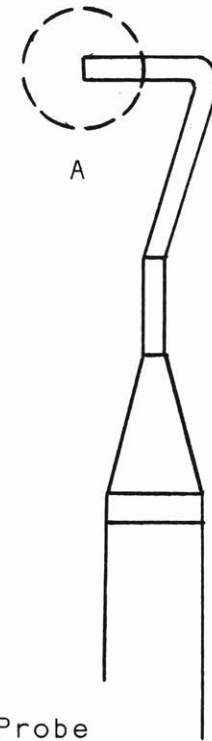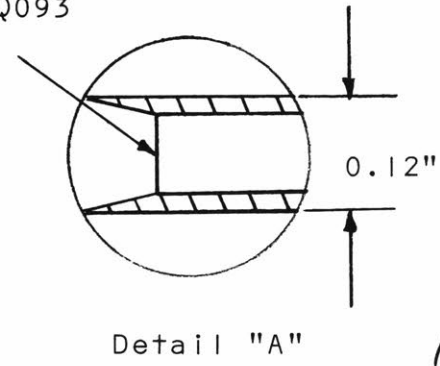
Figure 2.10   Scale Drawing and Picture of
Miniature Stagnation Pressure Probe
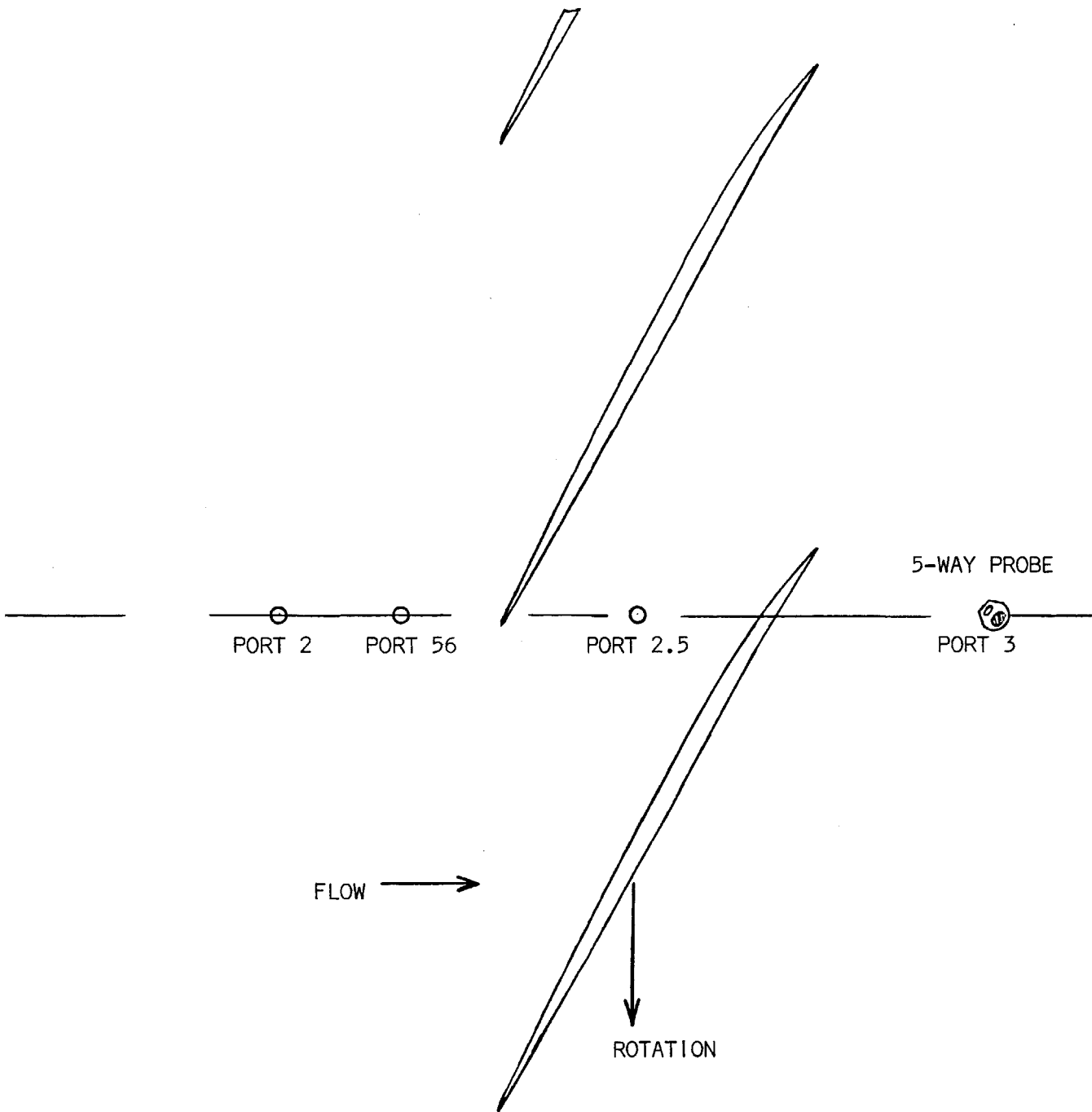
FIGURE 2.11   SCALE DRAWING OF ROTOR TIP SECTION & RELATIVE POSITION
OF INSTRUMENTATION PORTS.
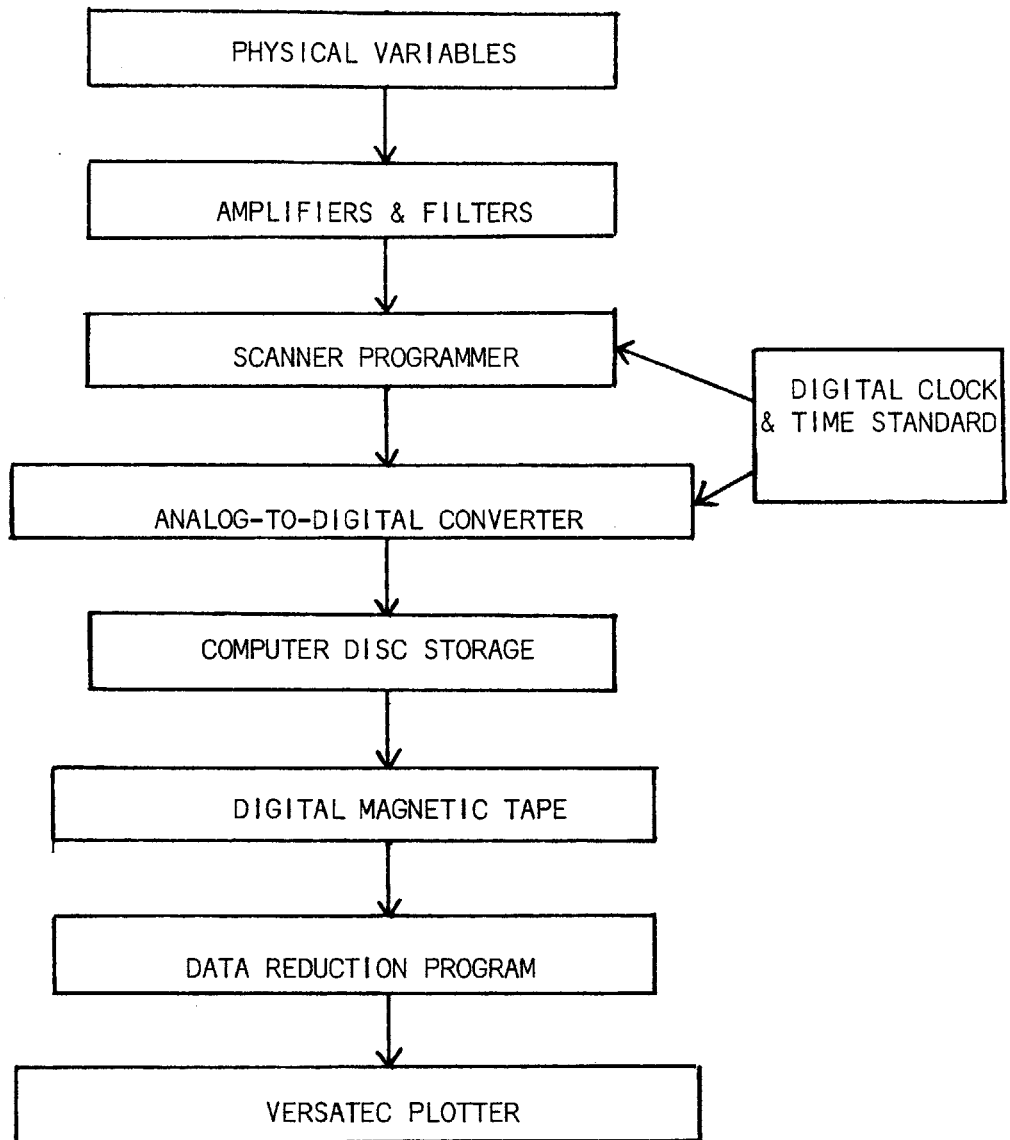
FIGURE 2.12 FLOW CHART FOR ANALOG-TO-DIGITAL CONVERSION AND DATA
STORAGE SETUP
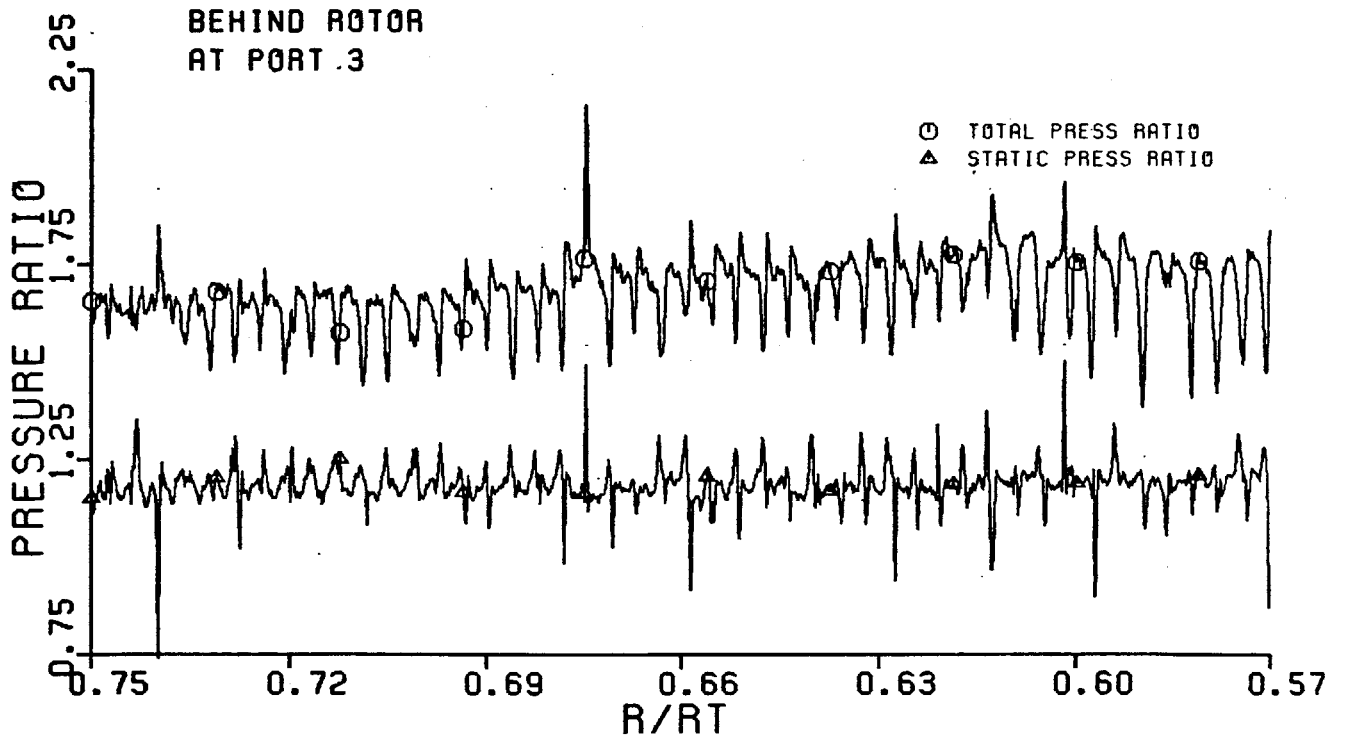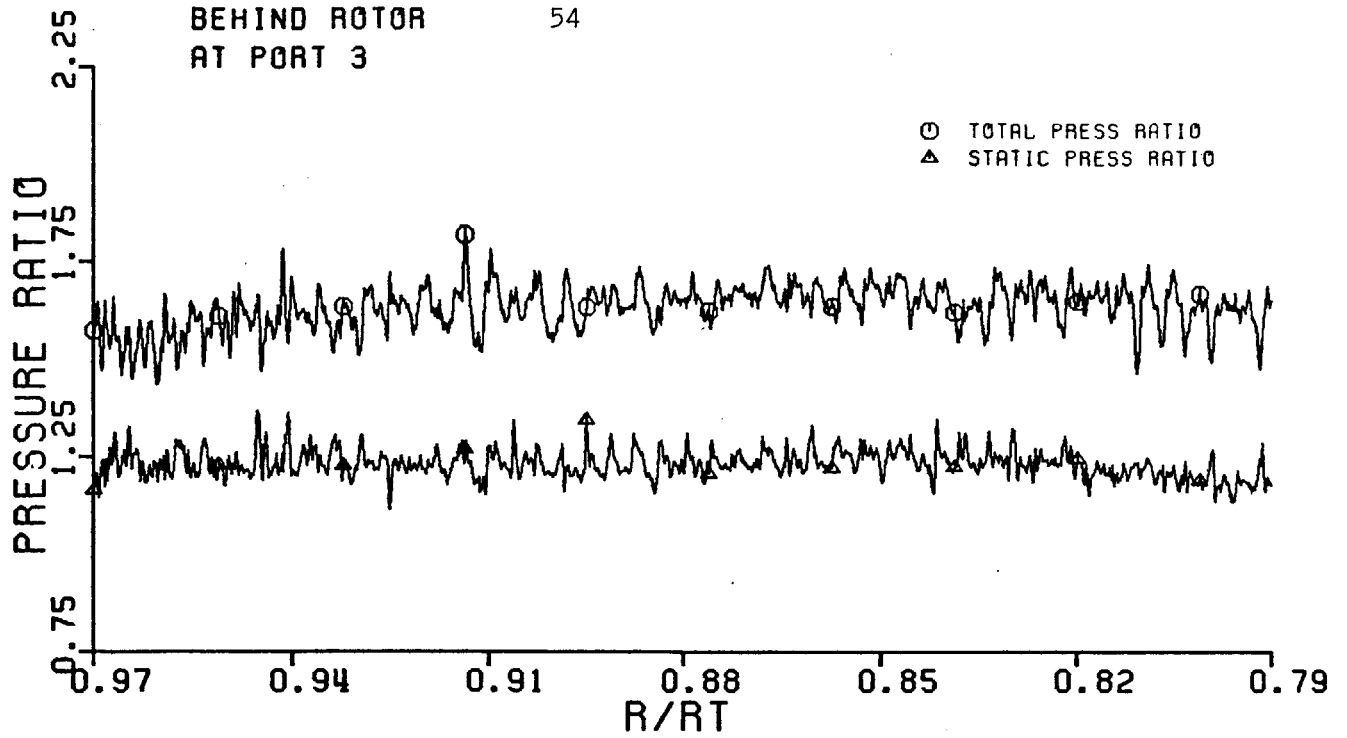
FIGURE 3.1.A   TOTAL & STATIC PRESSURE RATIOS BEHIND ROTOR VS. RADIUS RATIO
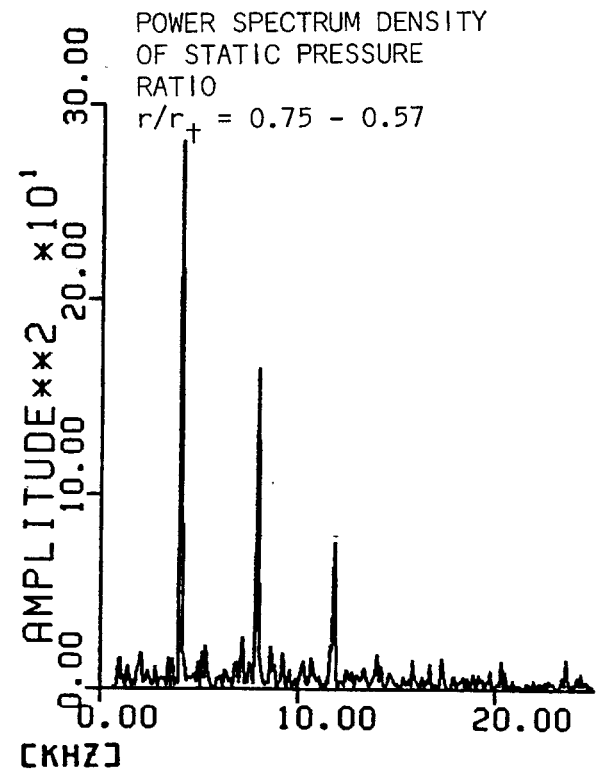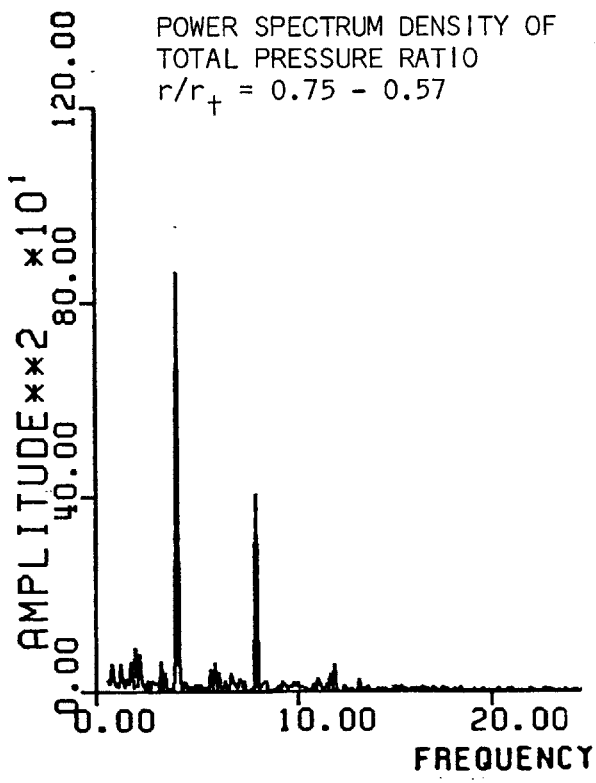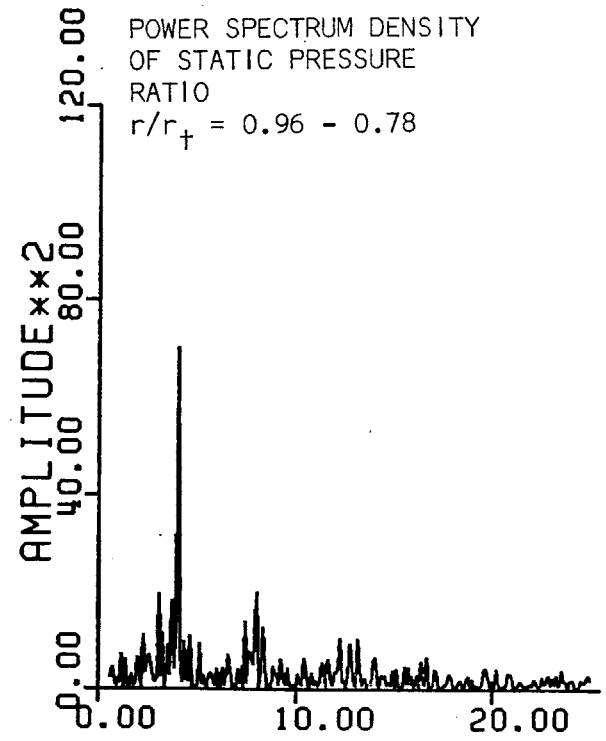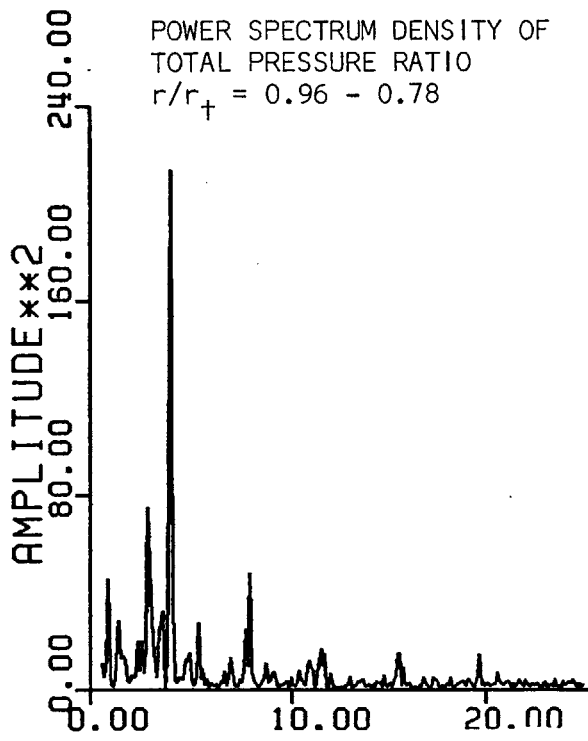
FIGURE 3.2.A   FREQUENCY SPECTRUM OF TOTAL & STATIC PRESSURE RATIOS
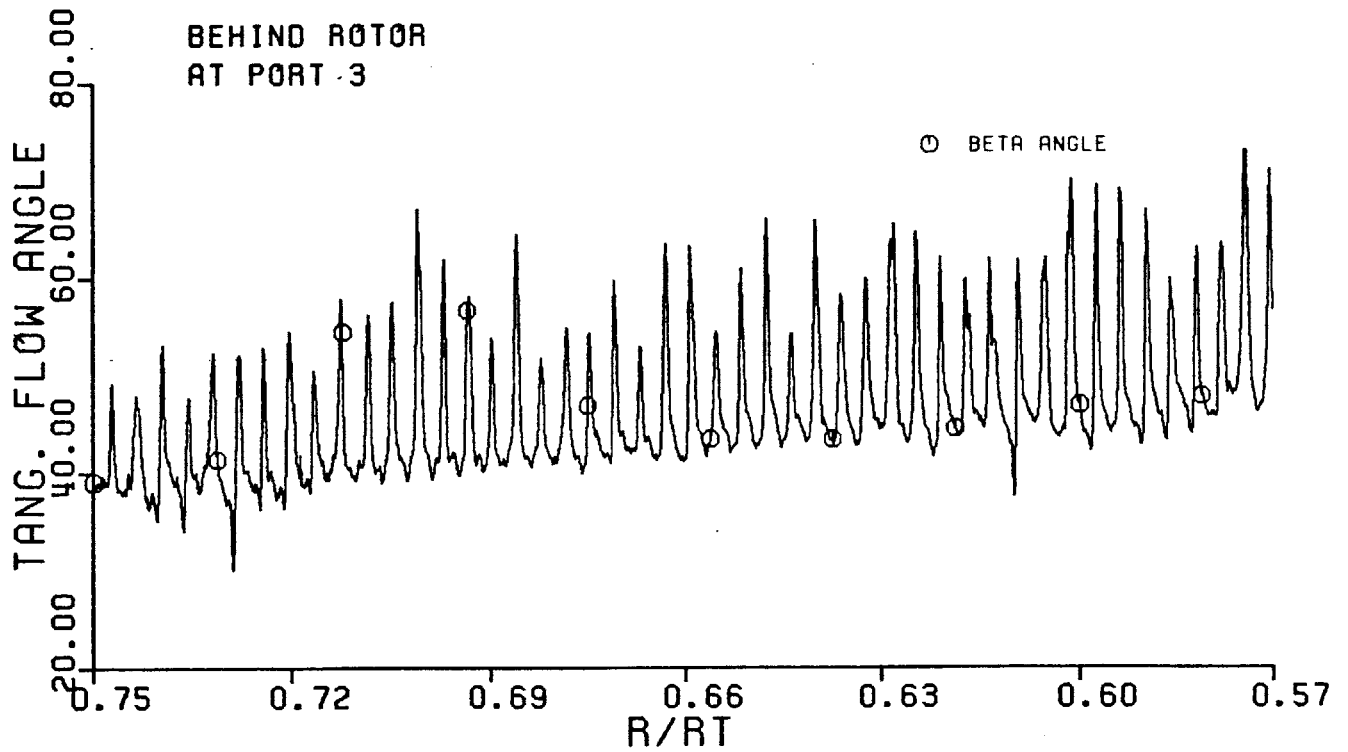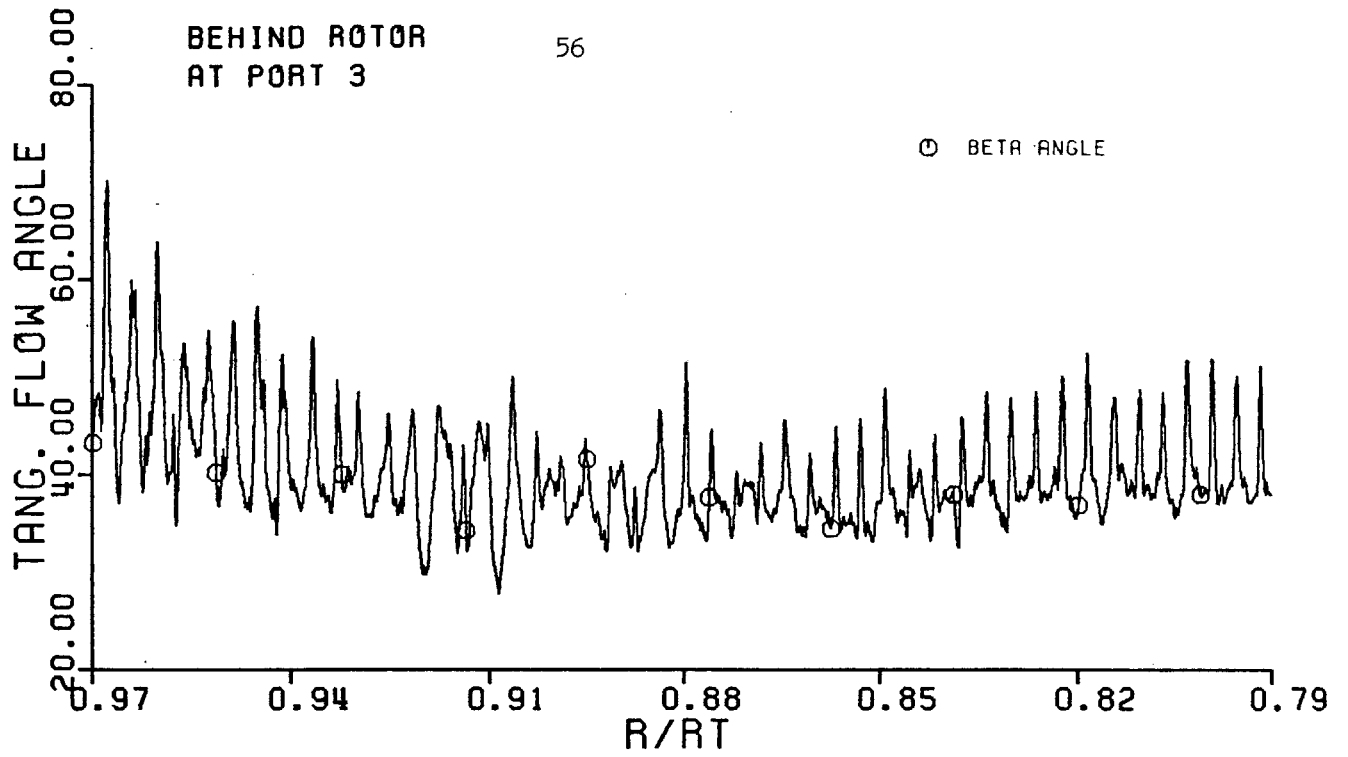
FIGURE 3.1.B   TANGENTIAL FLOW ANGLE BEHIND ROTOR VS. RADIUS RATIOS
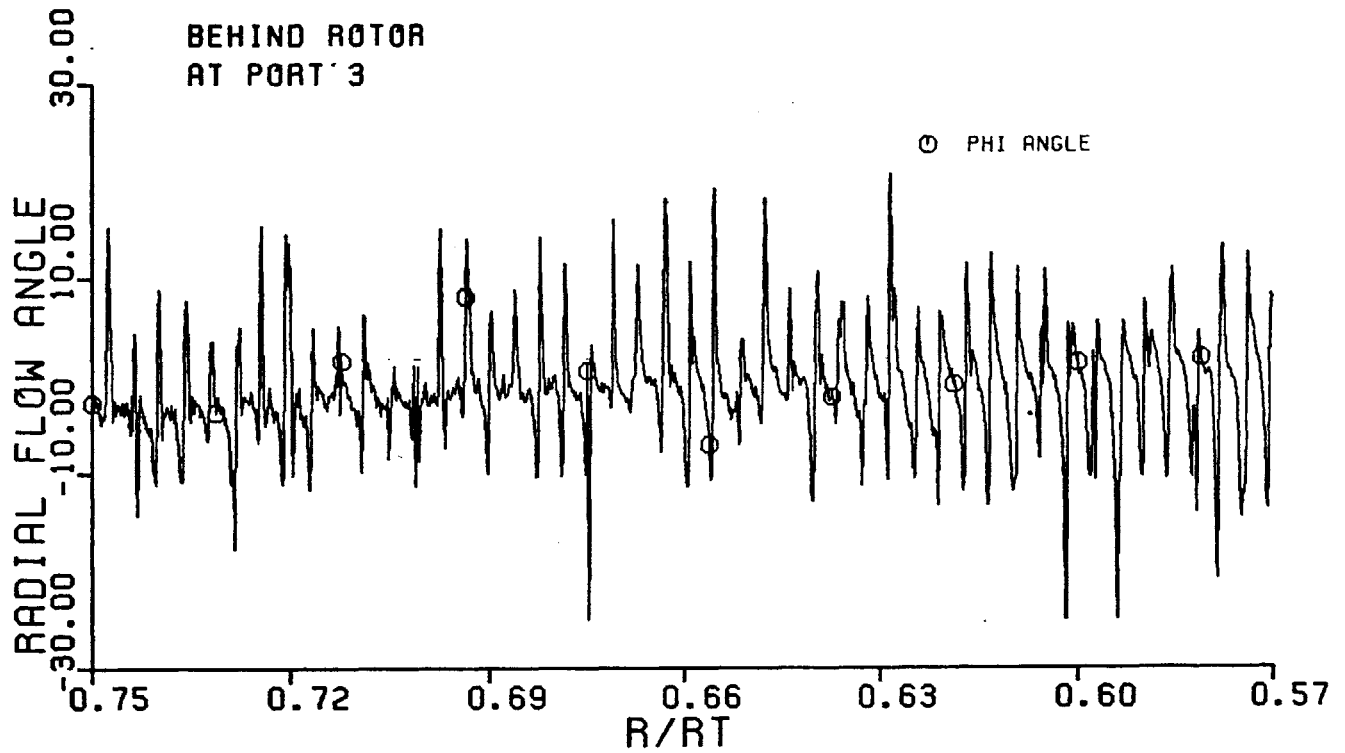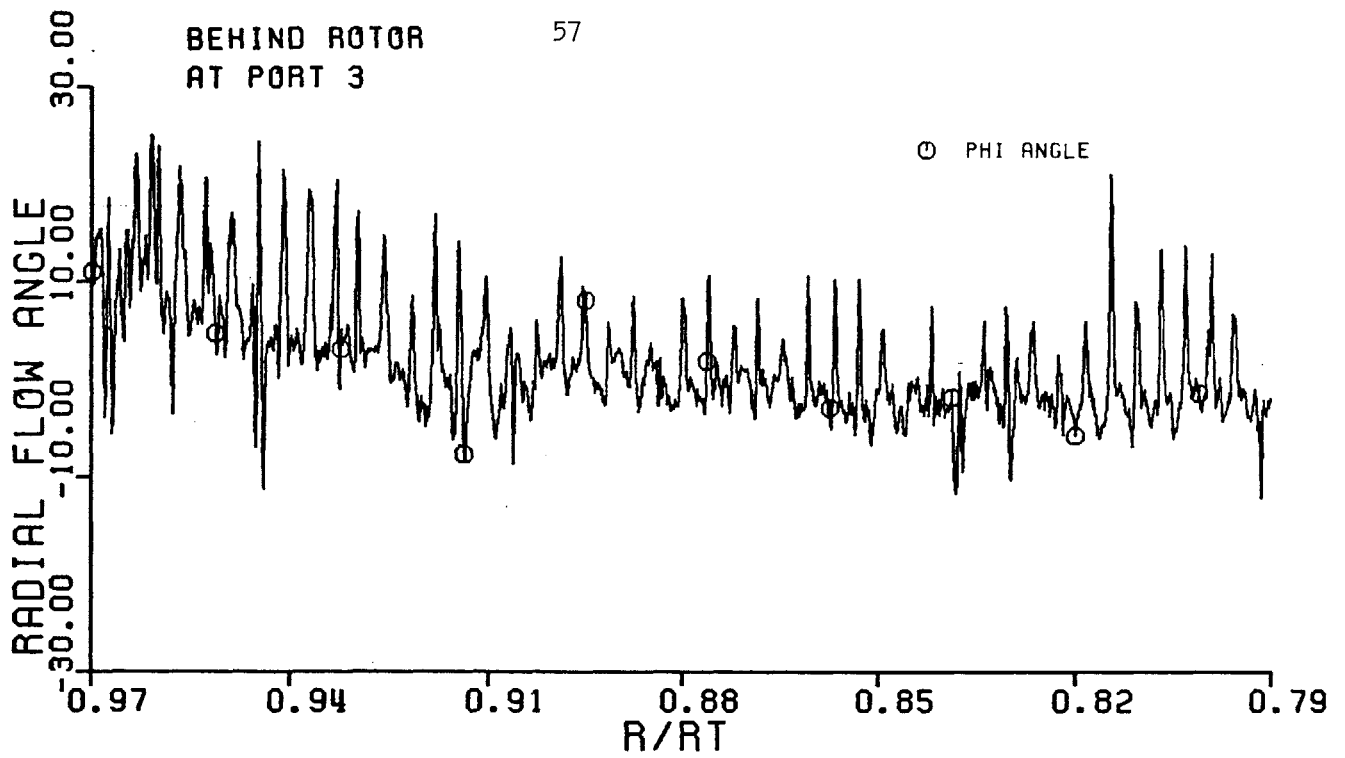
FIGURE 3.I.C RADIAL FLOW ANGLE BEHIND ROTOR VS. RADIUS RATIOS
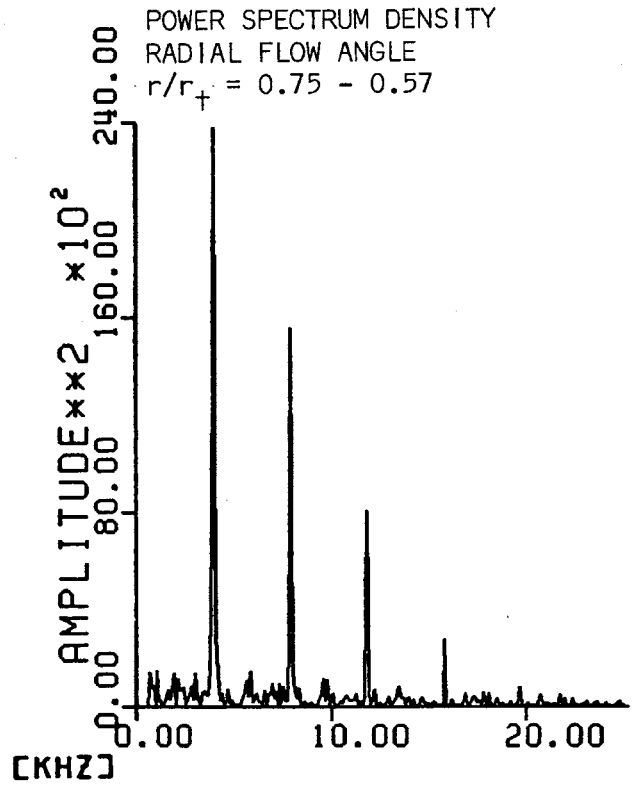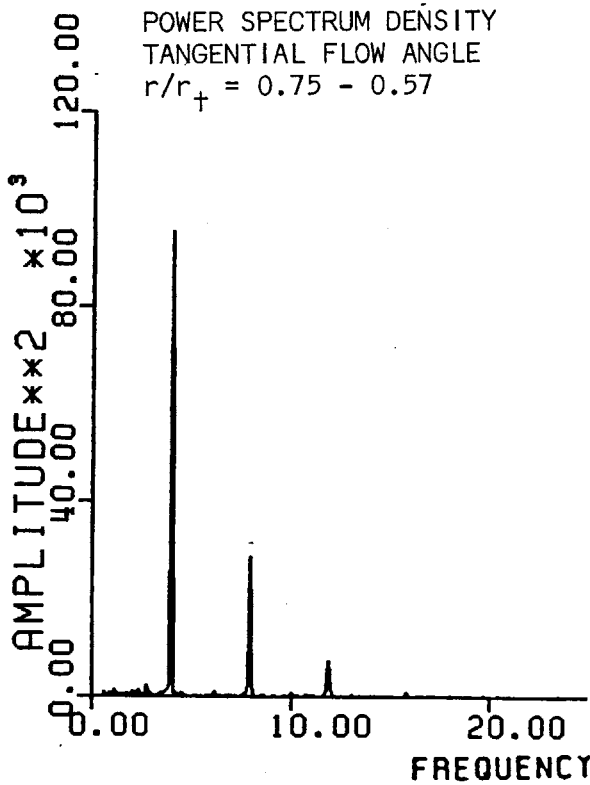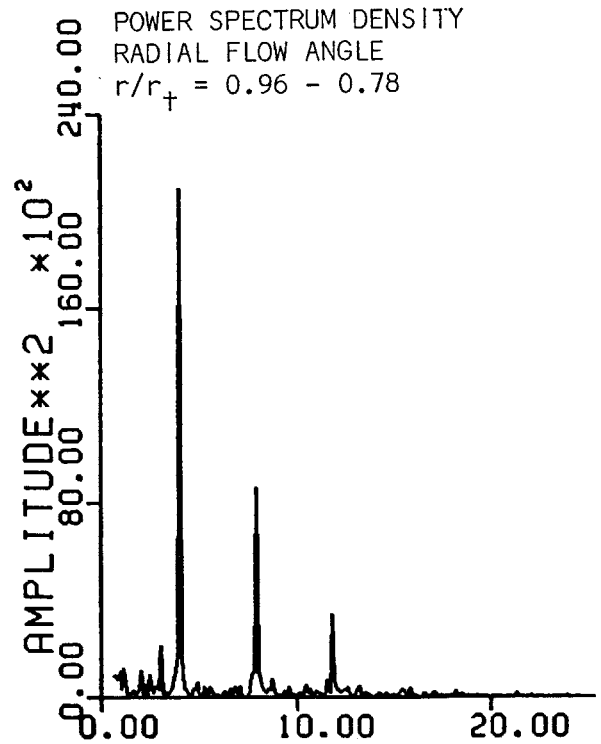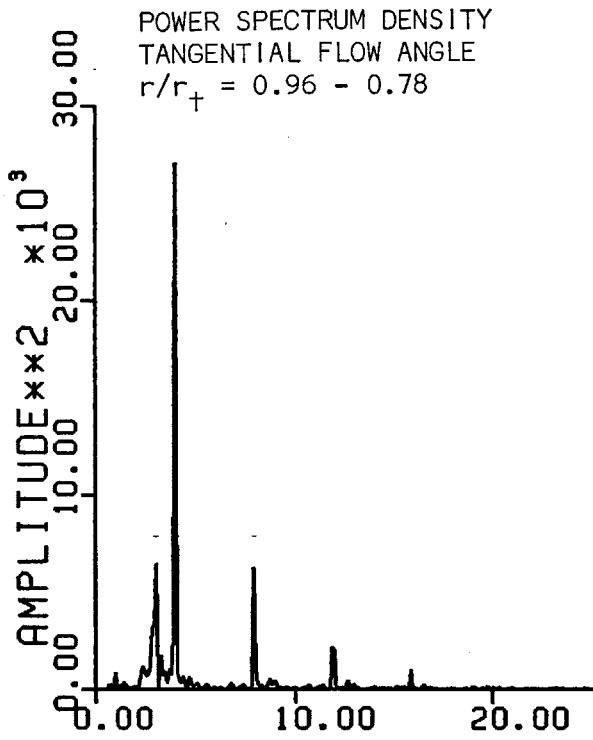
FIGURE 3.2.B   FREQUENCY SPECTRUM OF TANGENTIAL & RADIAL FLOW ANGLES
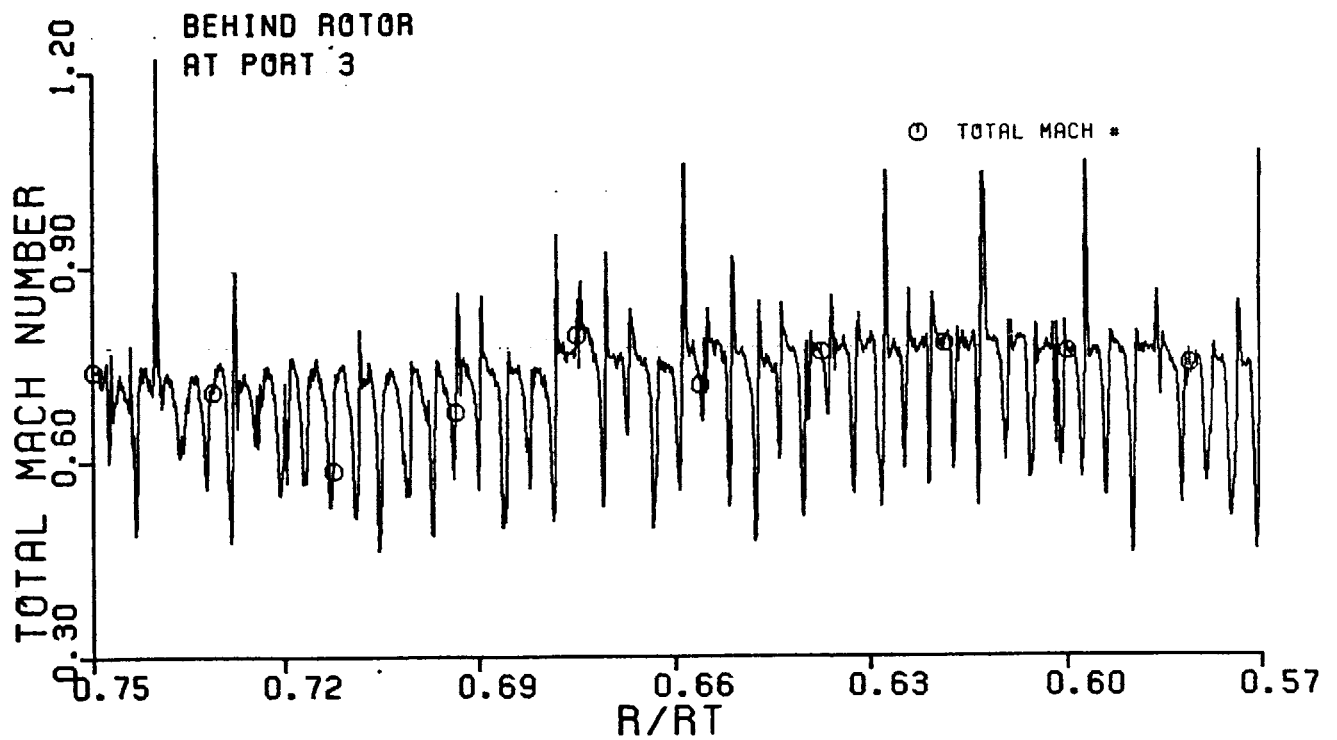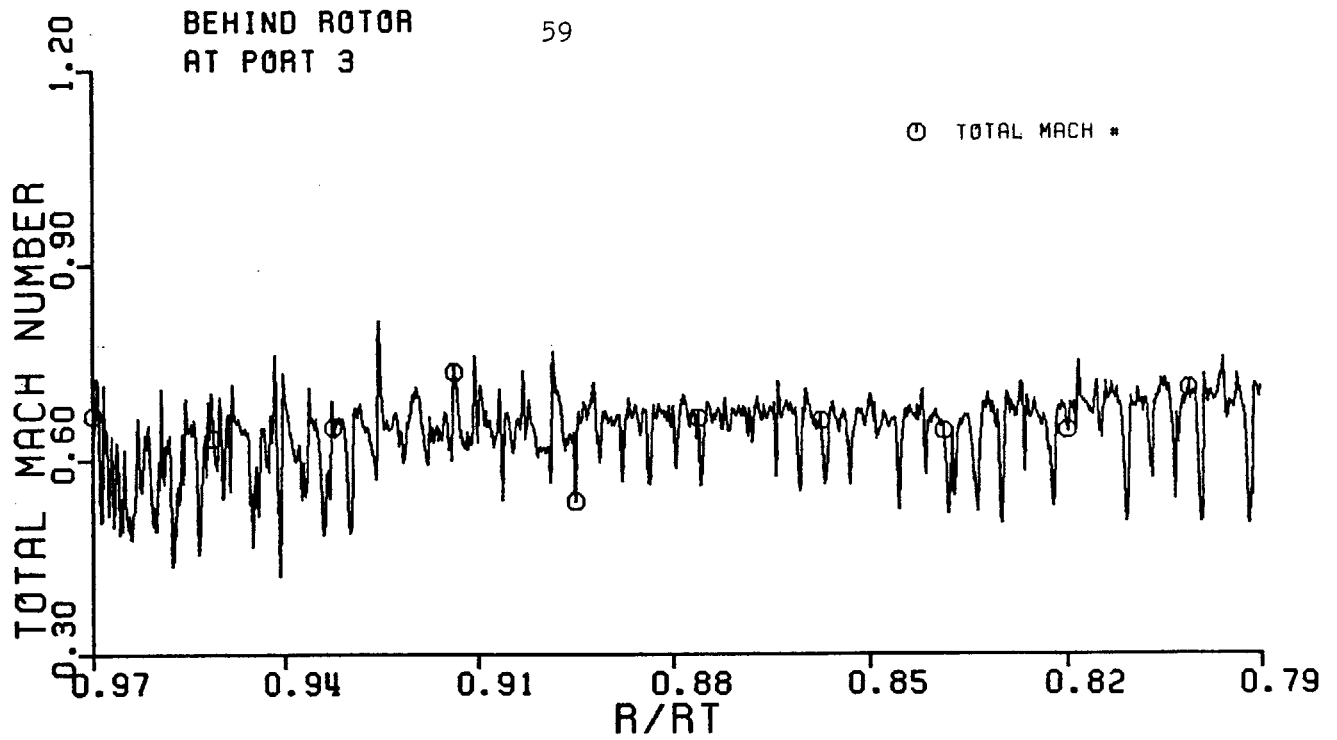
FIGURE 3.1.D TOTAL MACH NUMBER BEHIND ROTOR VS. RADIUS RATIO
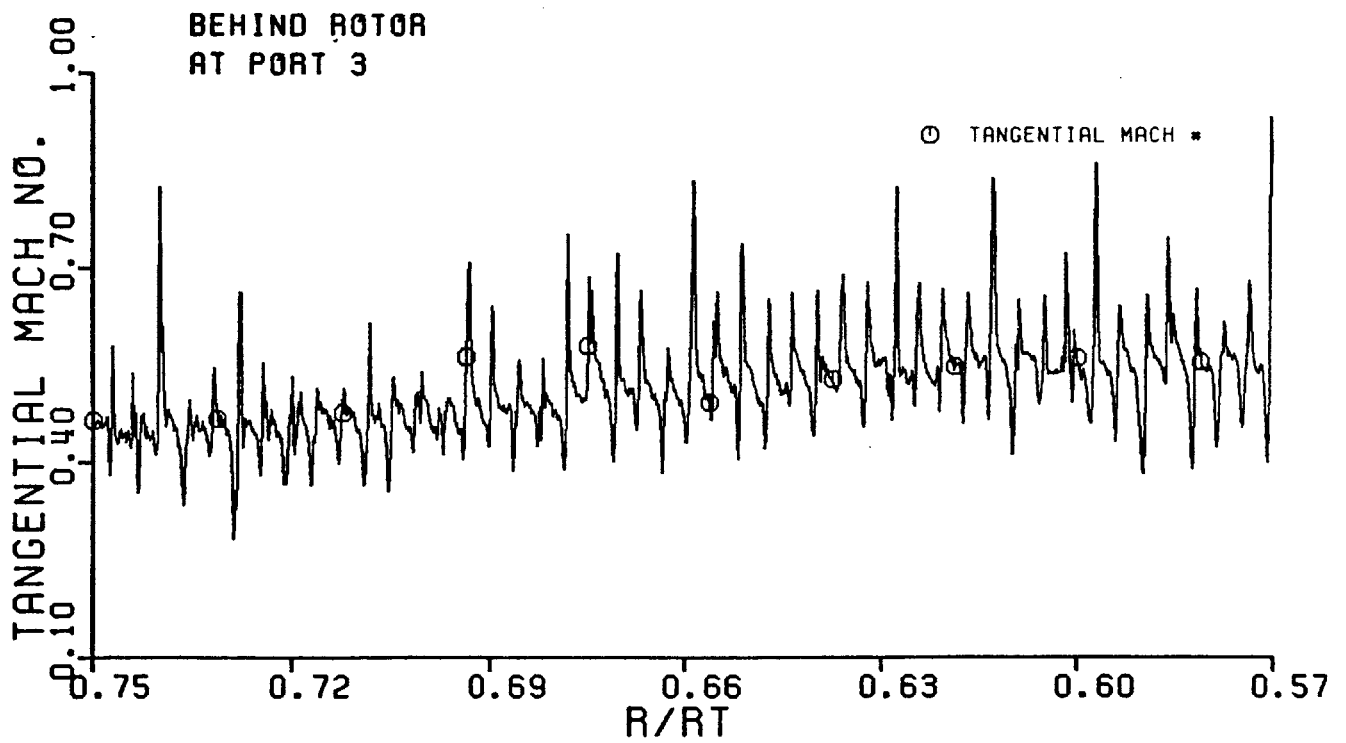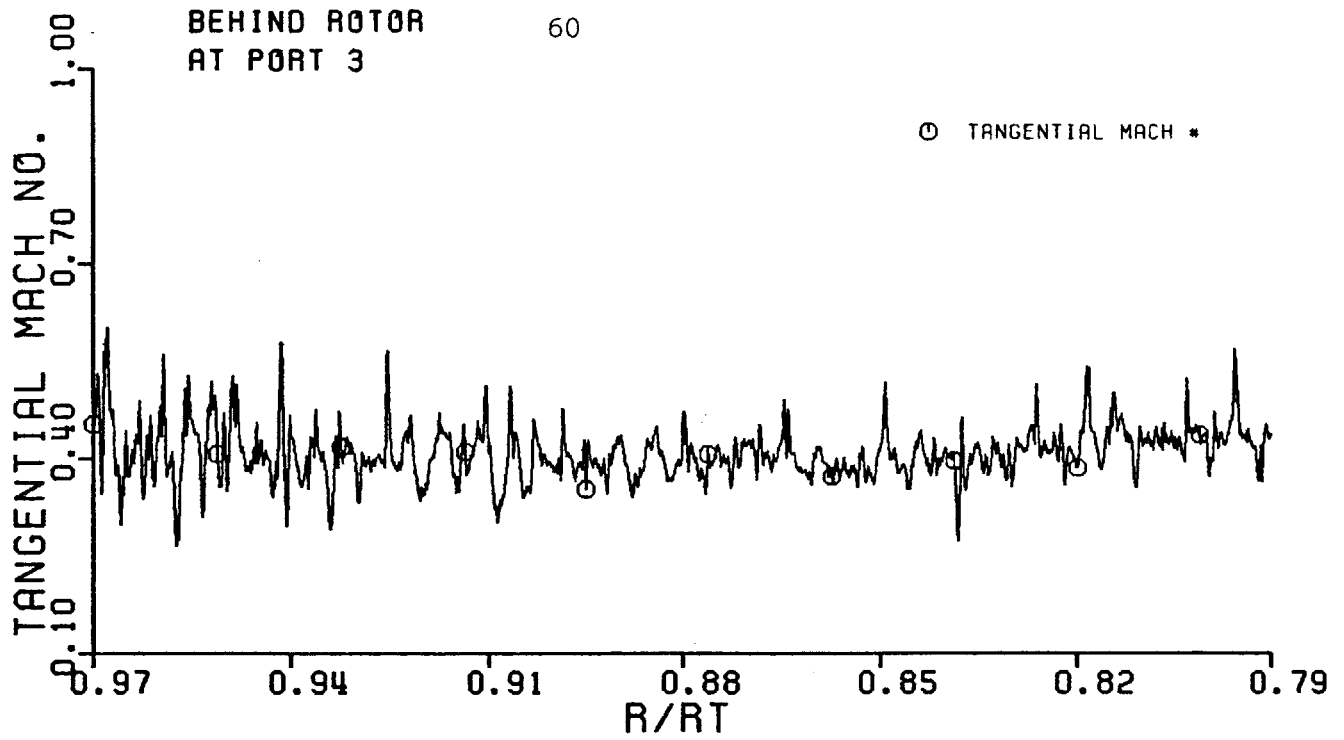
FIGURE 3.1.E   TANGENTIAL MACH NUMBER BEHIND ROTOR VS. RADIUS RATIOS.

POWER SPECTRUM DENSITY OF
TOTAL MACH NUMBER
r/r_+ = 0.96 - 0.78

POWER SPECTRUM DENSITY OF
TANGENTIAL MACH NUMBER
r/r_+ = 0.96 - 0.78

POWER SPECTRUM DENSITY OF
TOTAL MACH NUMBER
r/r_+ = 0.75 - 0.57

POWER SPECTRUM DENSITY OF
TANGENTIAL MACH NUMBER
r/r_+ = 0.75 - 0.57
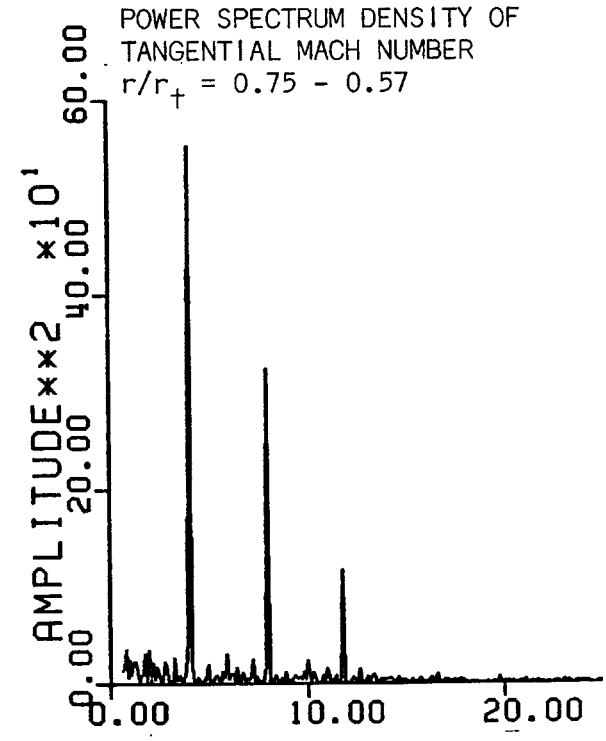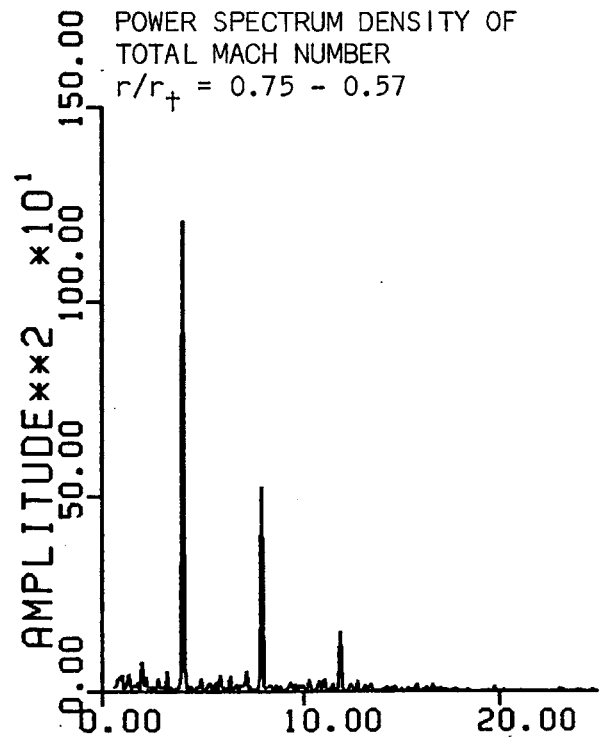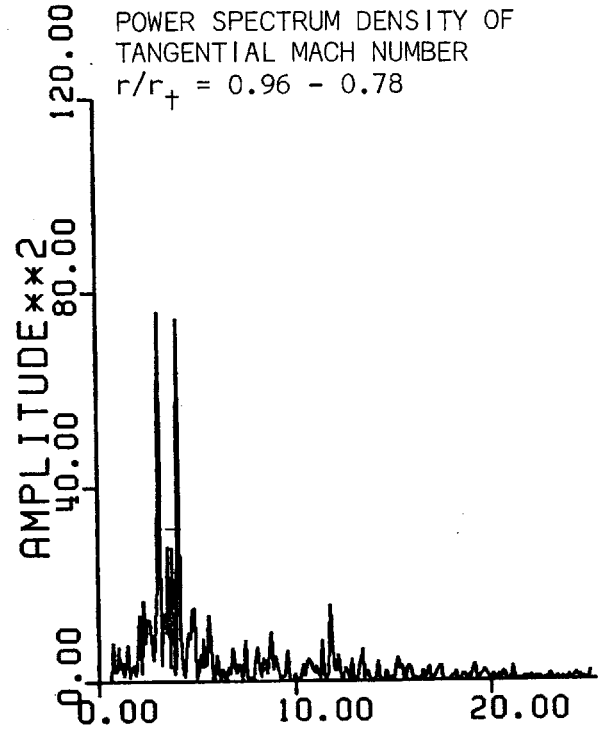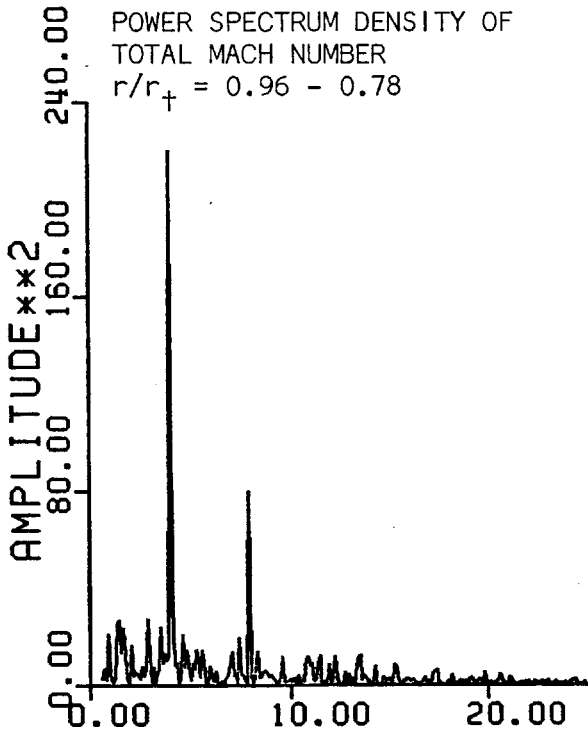
FREQUENCY [KHZ]

FIGURE 3.2.C.   FREQUENCY SPECTRUM OF TOTAL & TANGENTIAL MACH NUMBER
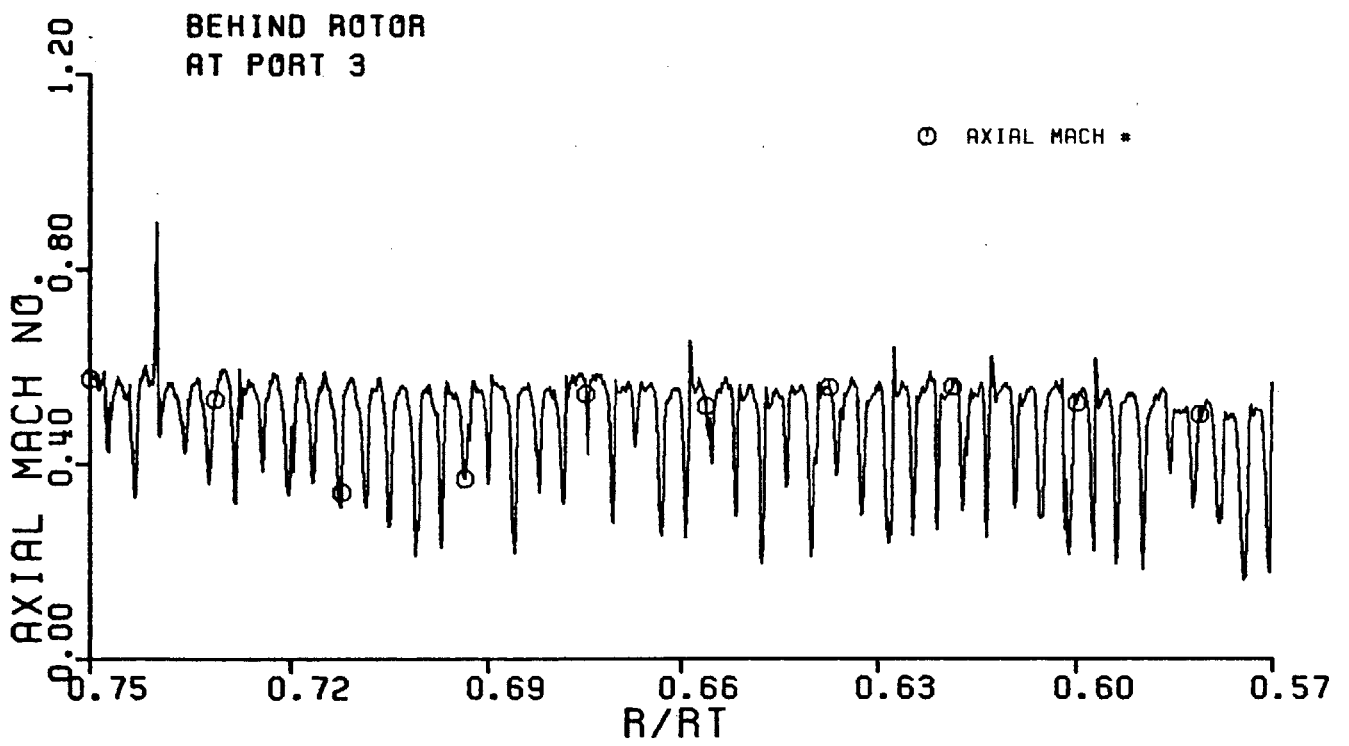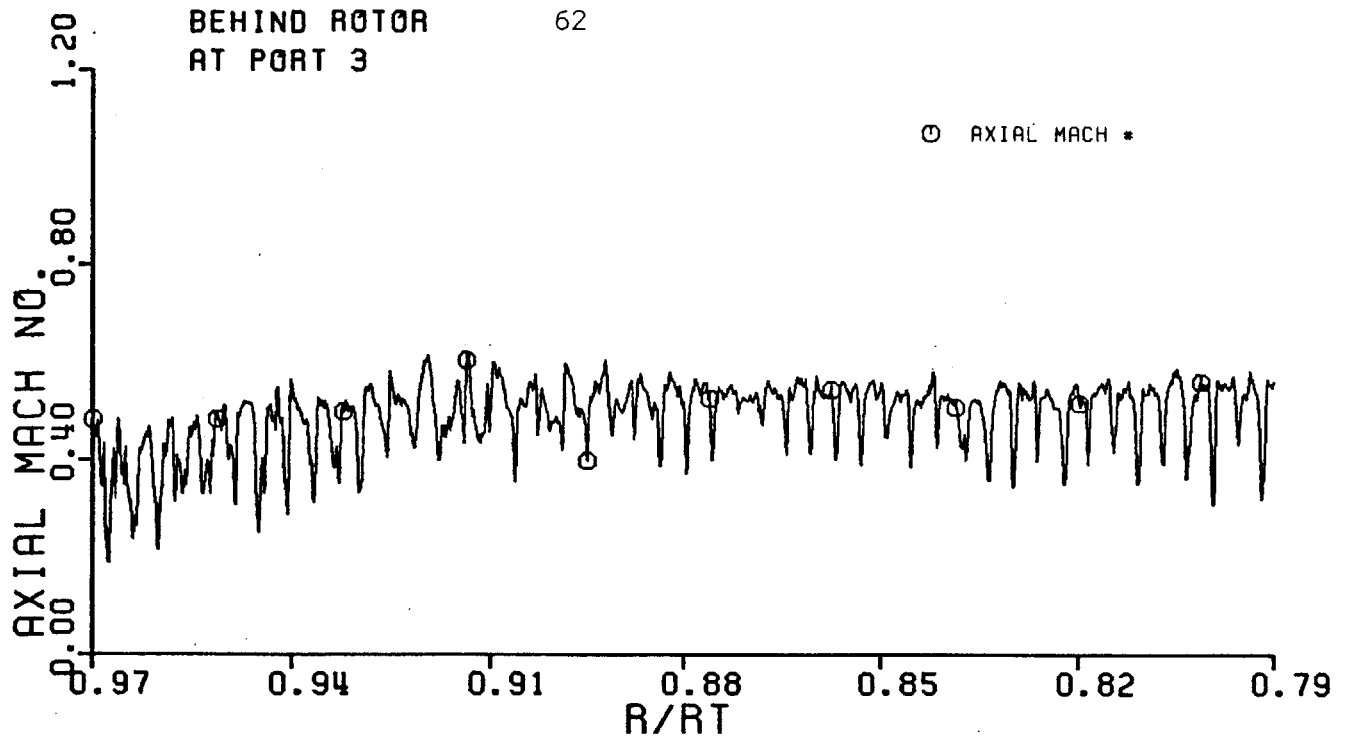
FIGURE 3.1.F   AXIAL MACH NUMBER BEHIND ROTOR VS. RADIUS RATIOS
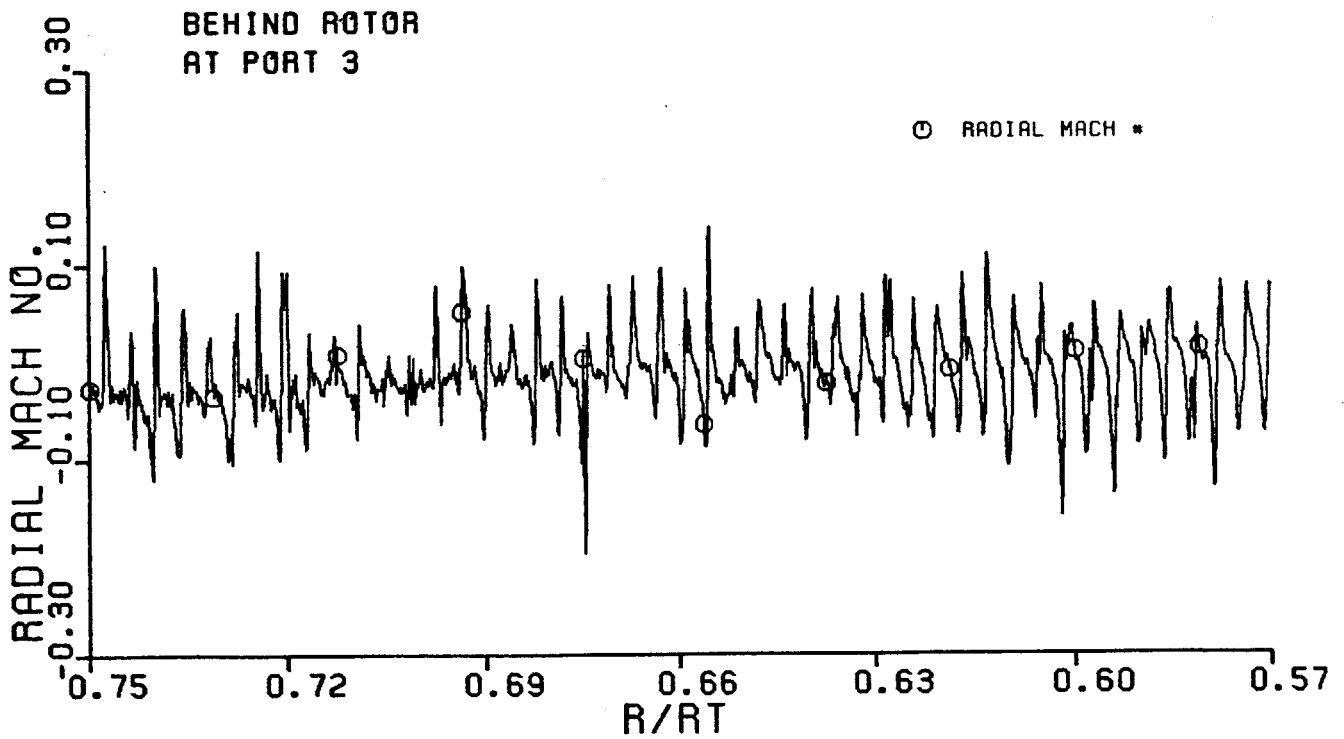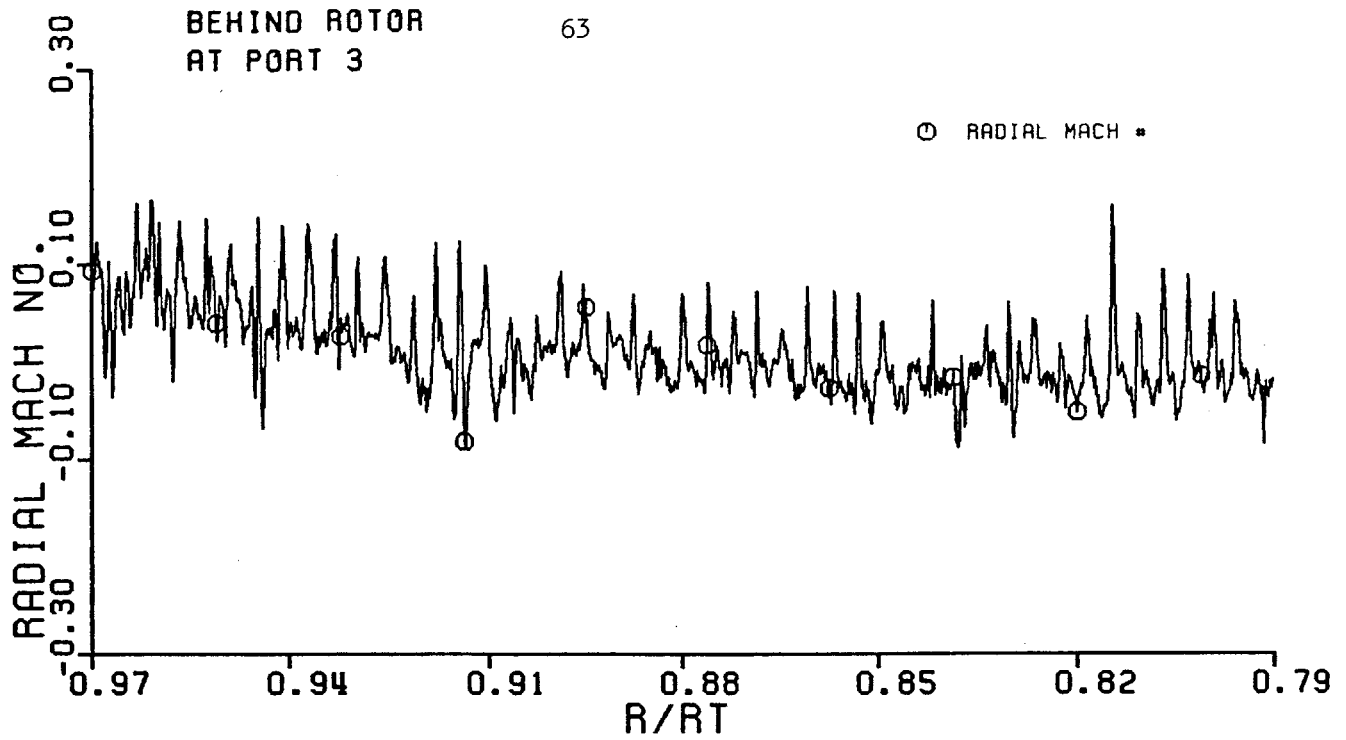
FIGURE 3.1.G RADIAL MACH NUMBER BEHIND ROTOR VS. RADIUS RATIOS.

POWER SPECTRUM DENSITY OF
AXIAL MACH NUMBER
$r/r_+ = 0.96 - 0.78$
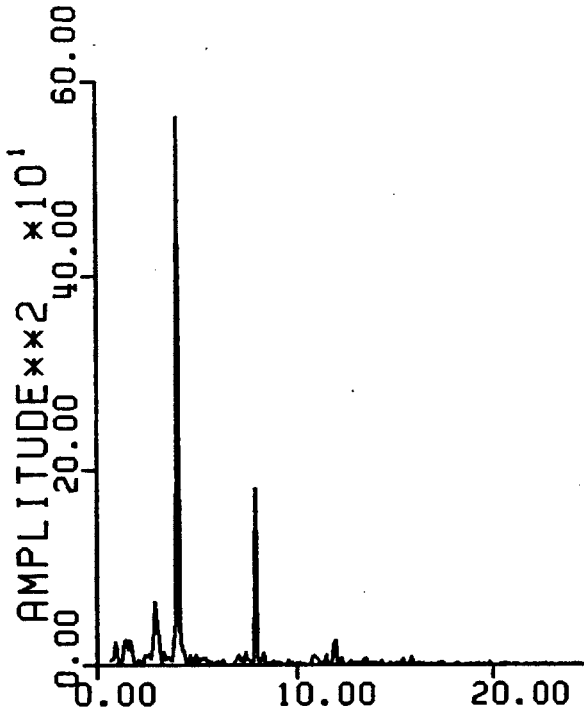
POWER SPECTRUM DENSITY OF
RADIAL MACH NUMBER
$r/r_+ = 0.96 - 0.78$
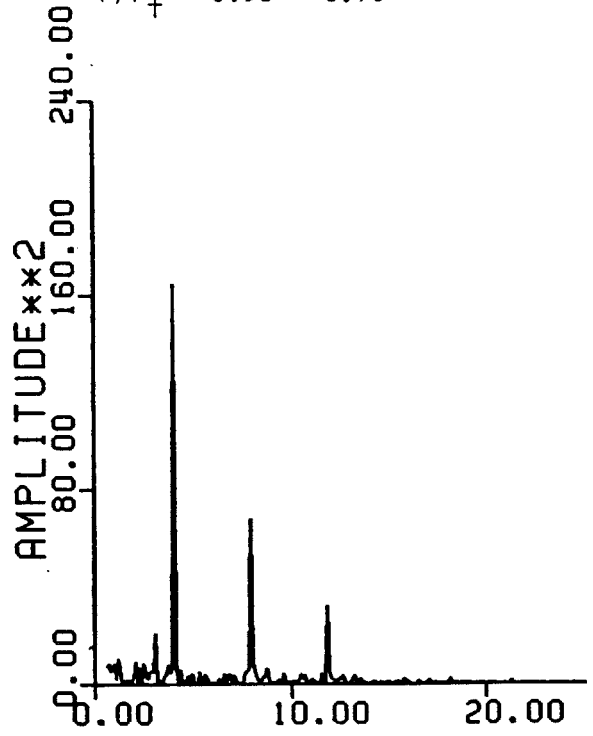
POWER SPECTRUM DENSITY OF
AXIAL MACH NUMBER
$r/r_+ = 0.75 - 0.57$
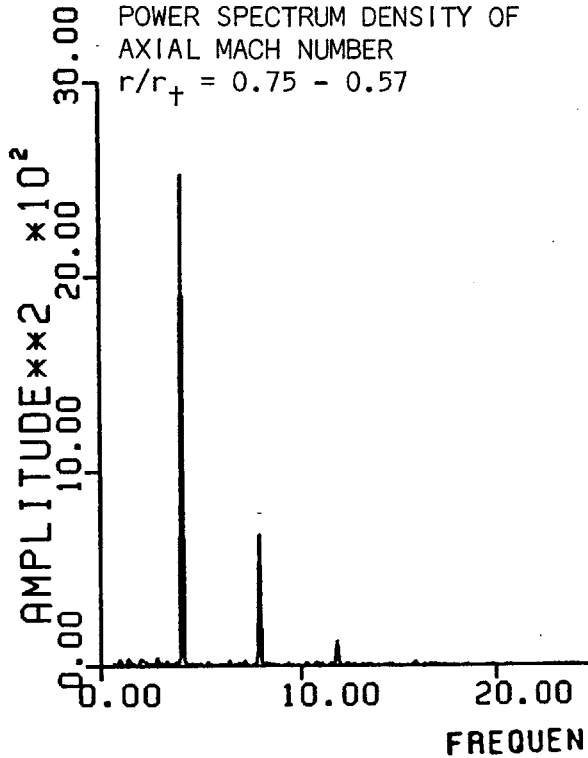
POWER SPECTRUM DENSITY OF
RADIAL MACH NUMBER
$r/r_+ = 0.75 - 0.57$
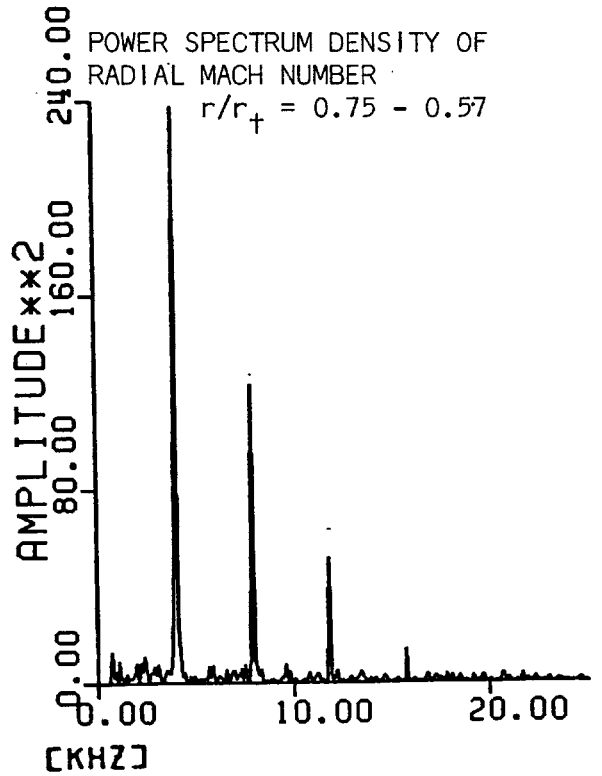
FREQUENCY [KHZ]

FIGURE 3.2.D   FREQUENCY SPECTRUM OF AXIAL & RADIAL MACH NUMBER
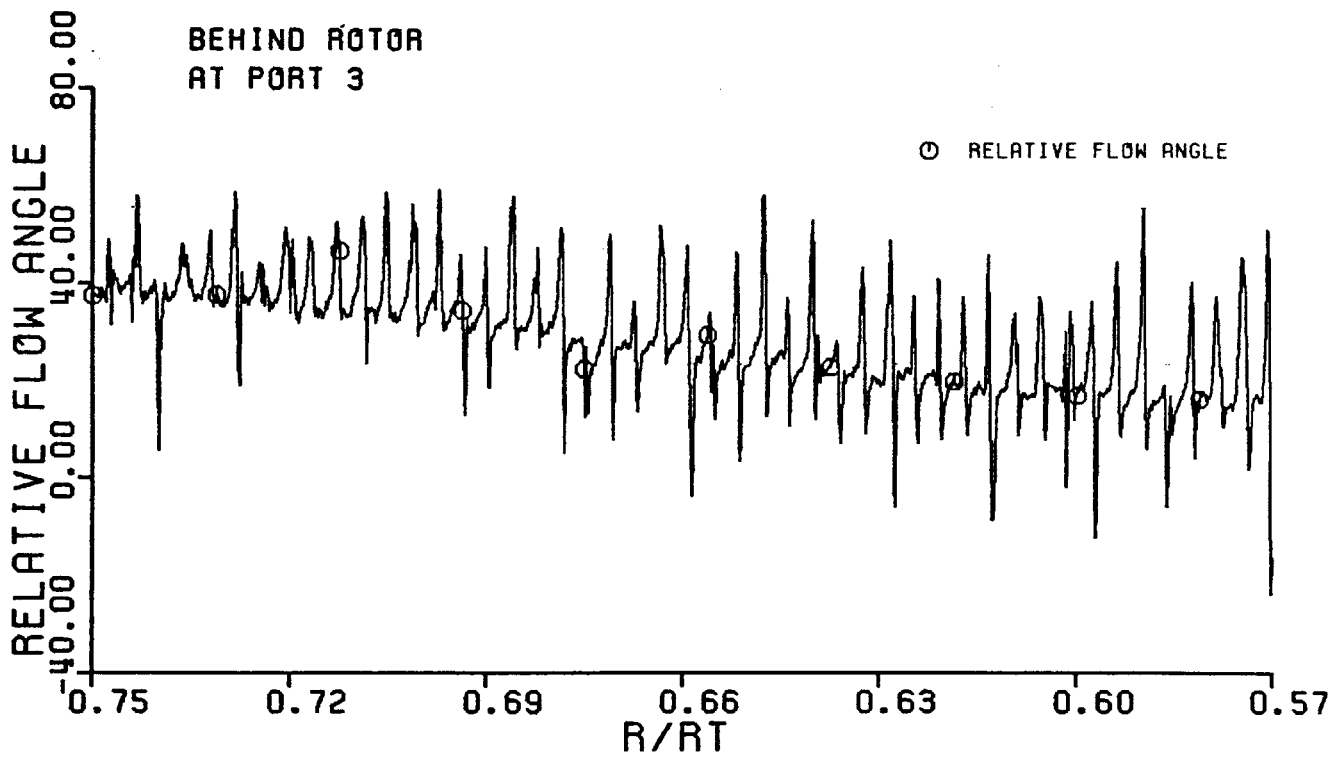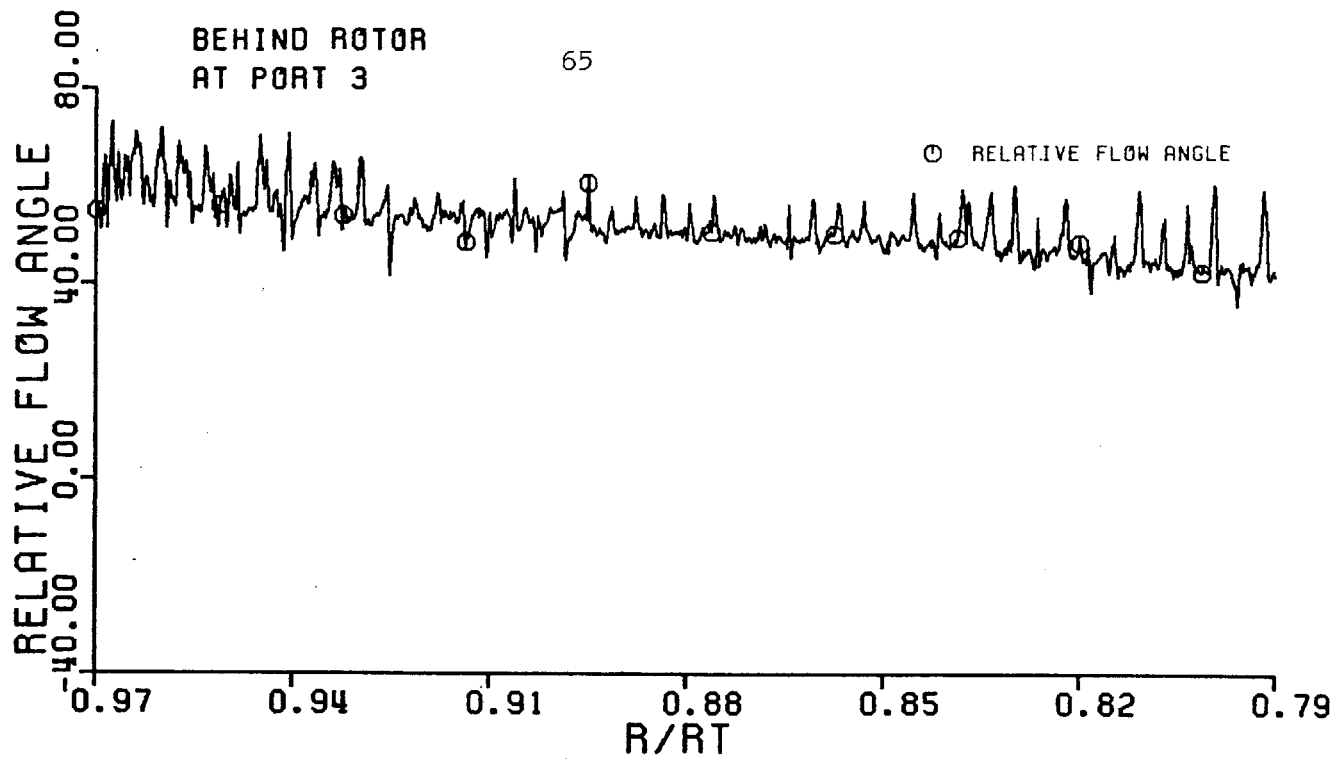
FIGURE 3.1.H   RELATIVE FLOW ANGLE BEHIND ROTOR VS. RADIUS RATIOS
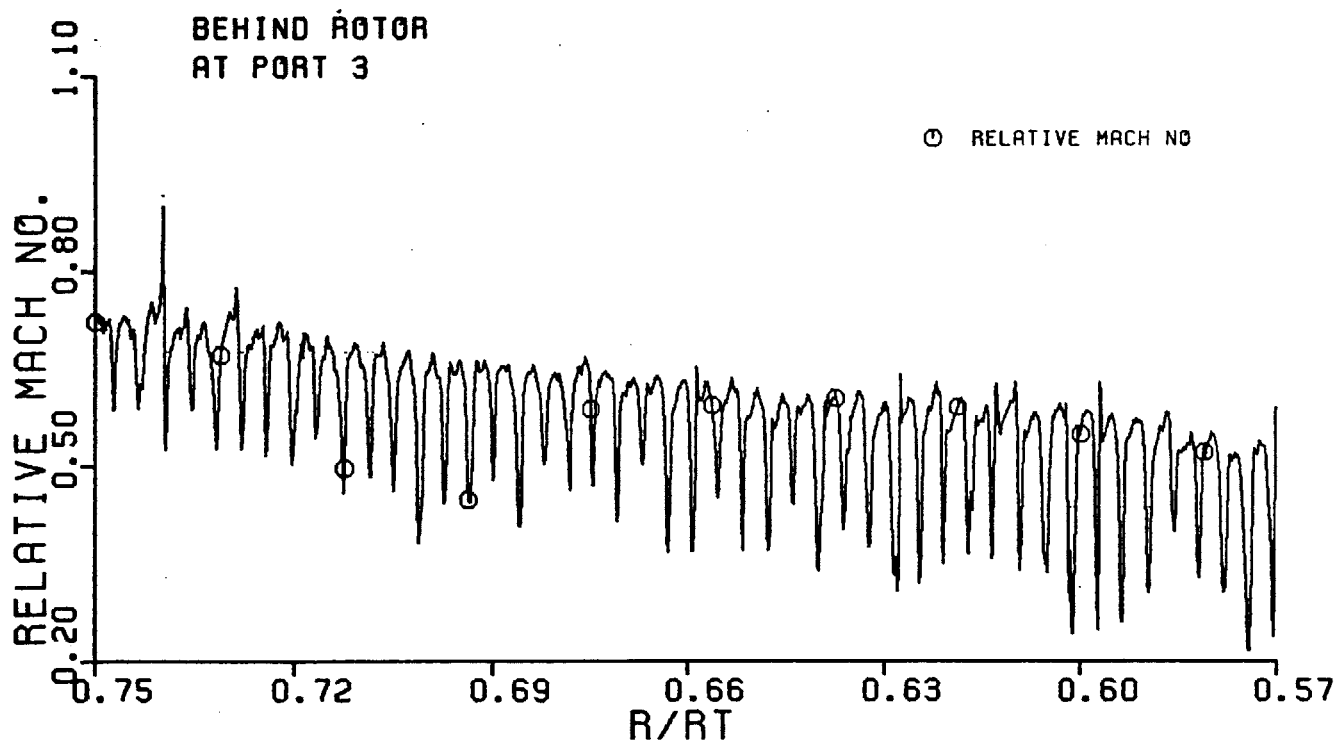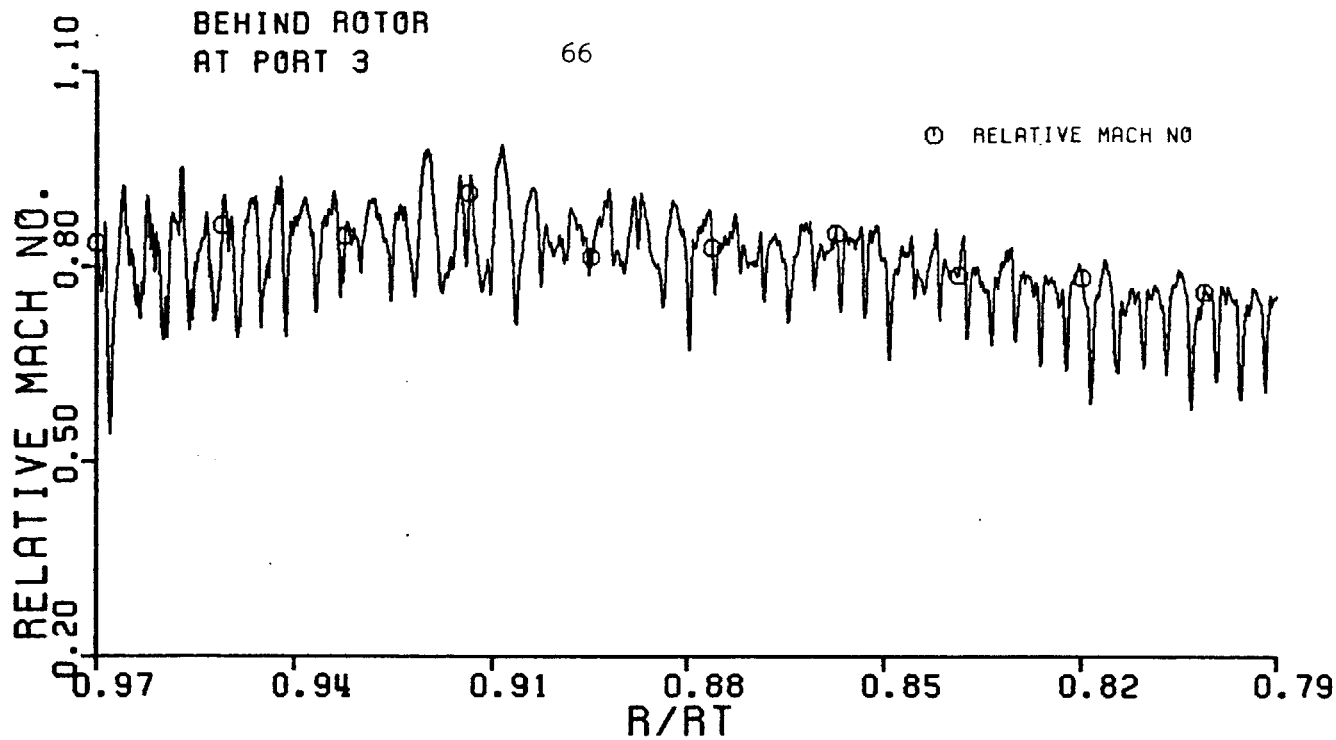
FIGURE 3.1.1 RELATIVE MACH NUMBER BEHIND ROTOR VS. RADIUS RATIOS
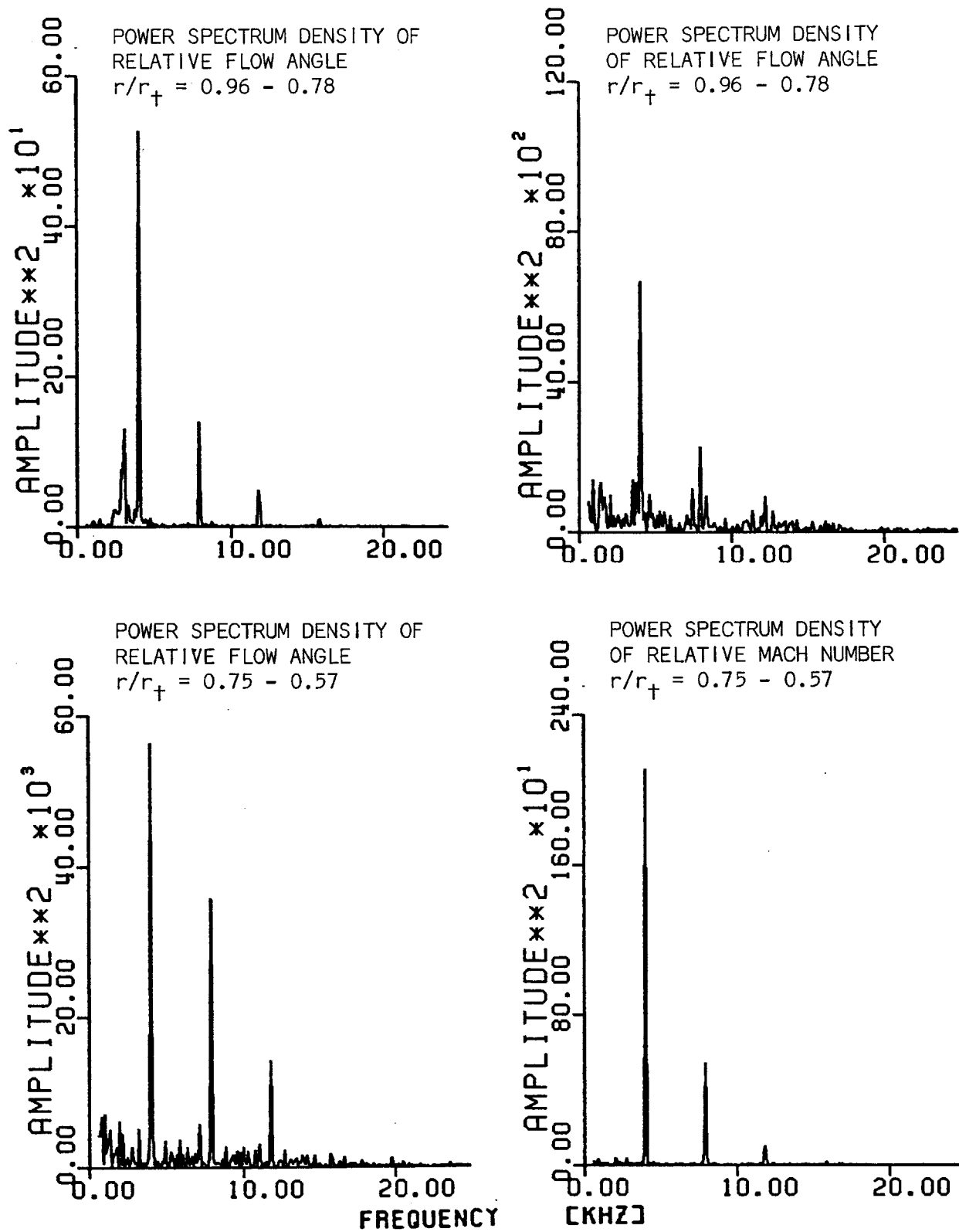
FIGURE 3.2.E   FREQUENCY SPECTRUM OF RELATIVE FLOW ANGLE & RELATIVE
              MACH NUMBER
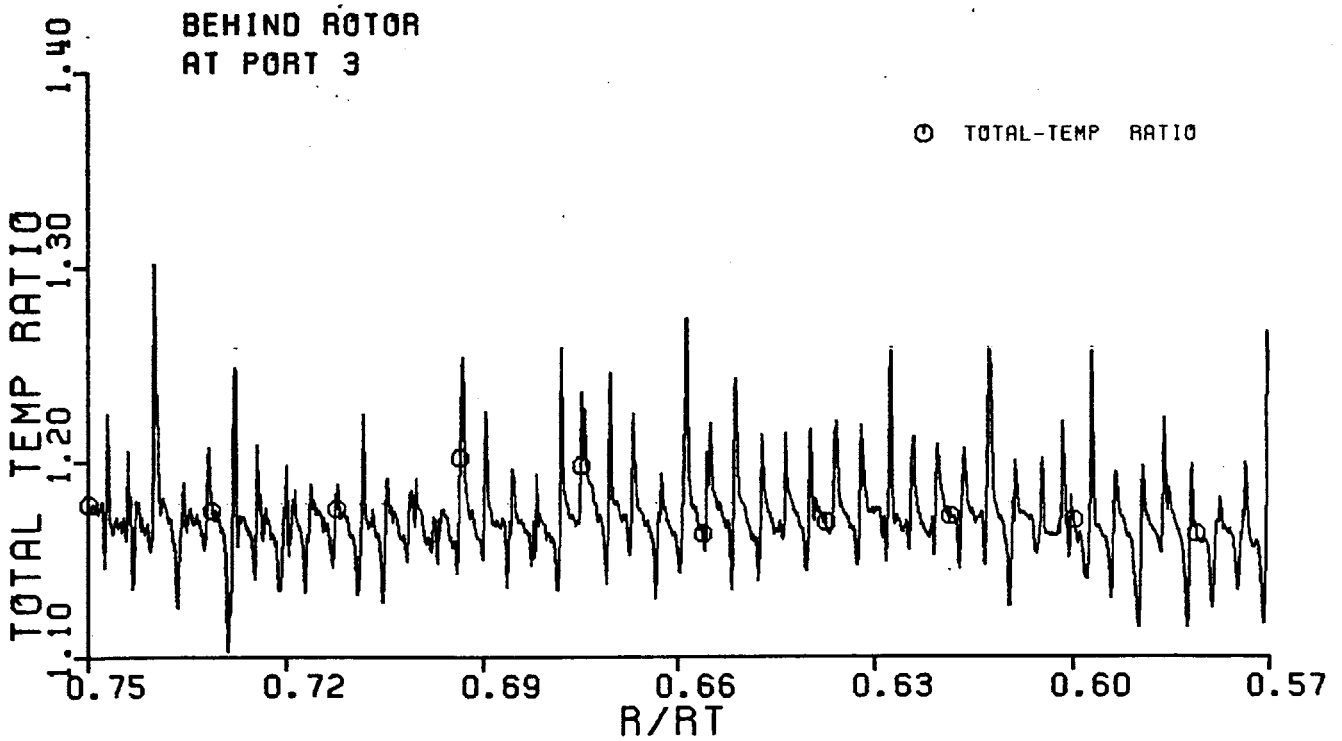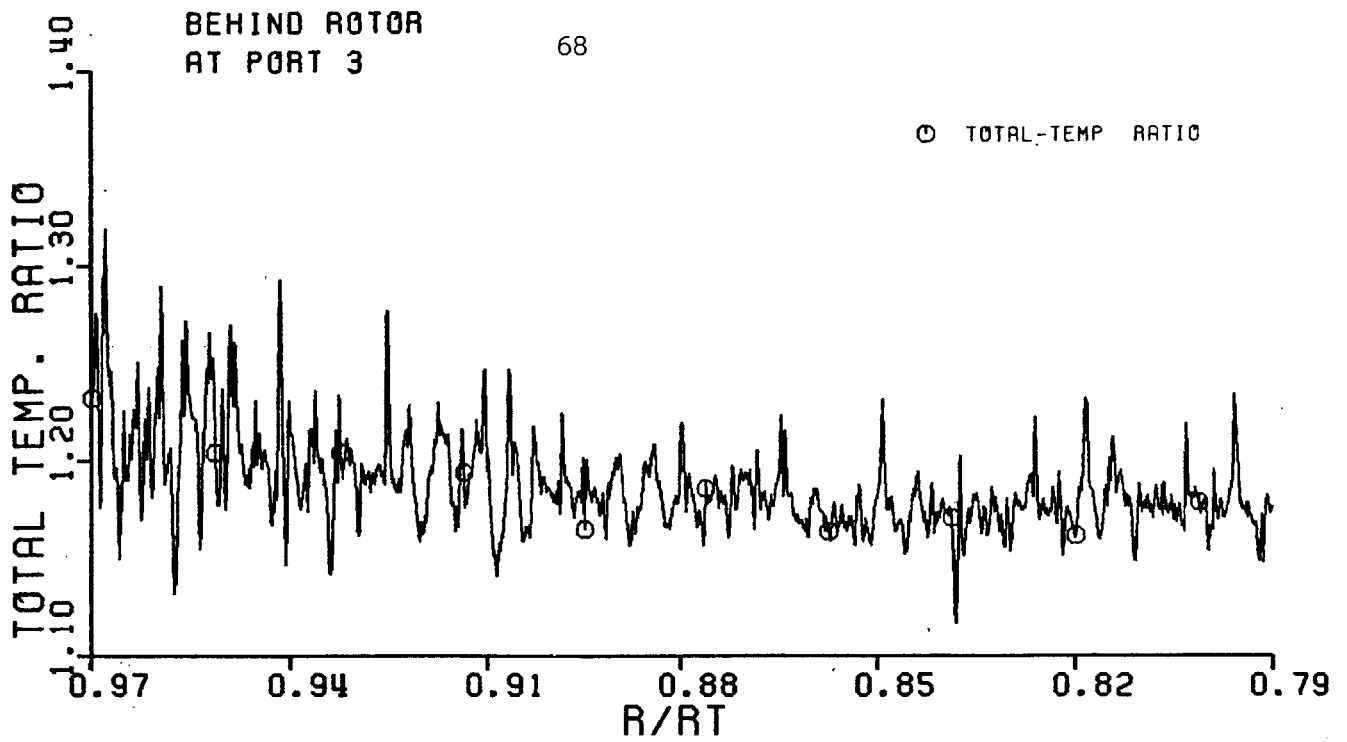
FIGURE 3.1.J   TOTAL TEMPERATURE RATIO BEHIND ROTOR VS. RADIUS RATIO
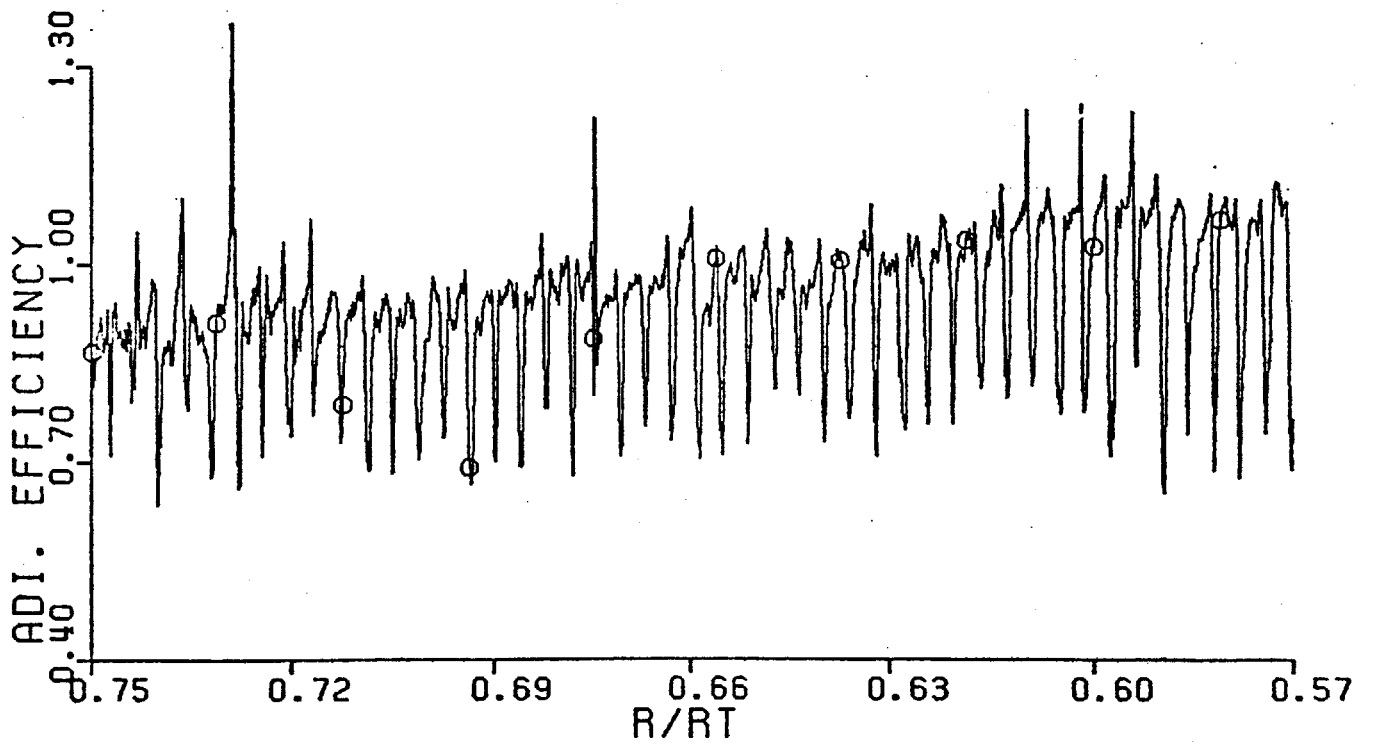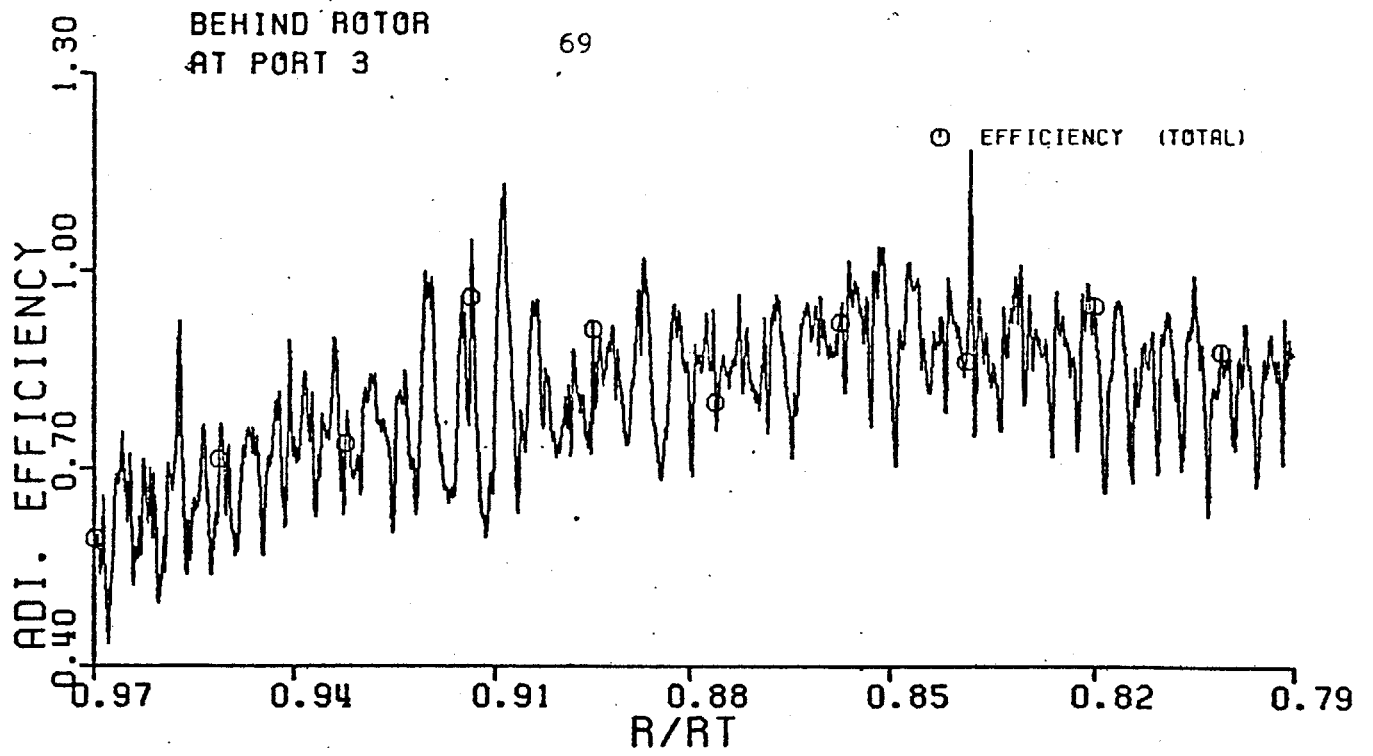
FIGURE 3.1.K TOTAL EFFICIENCY OF THE ROTOR VS. RADIUS RATIO.
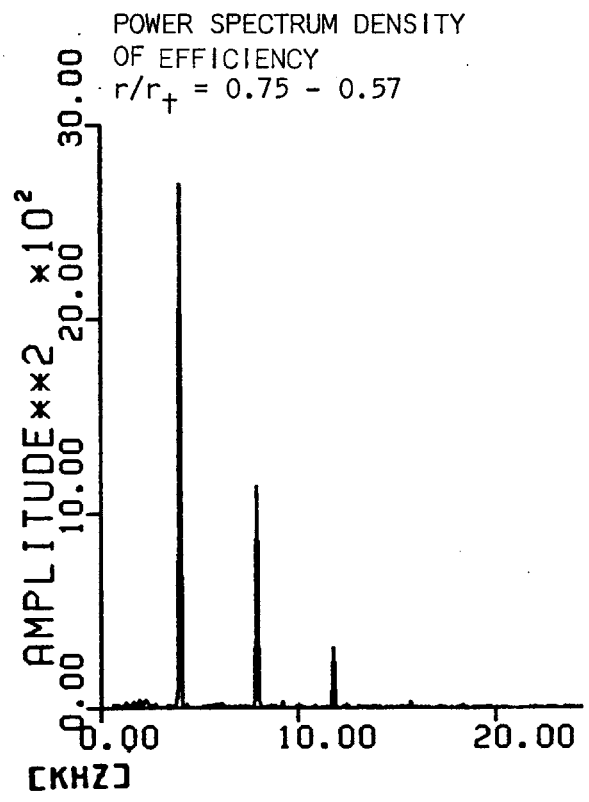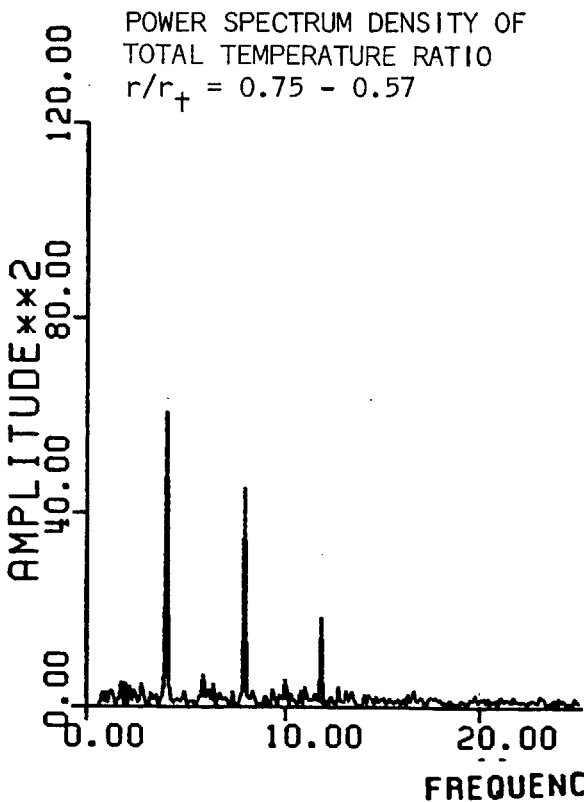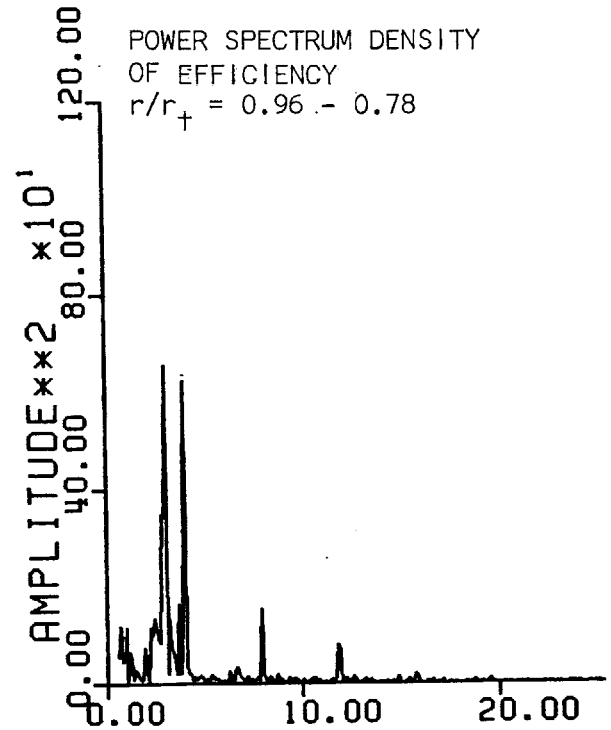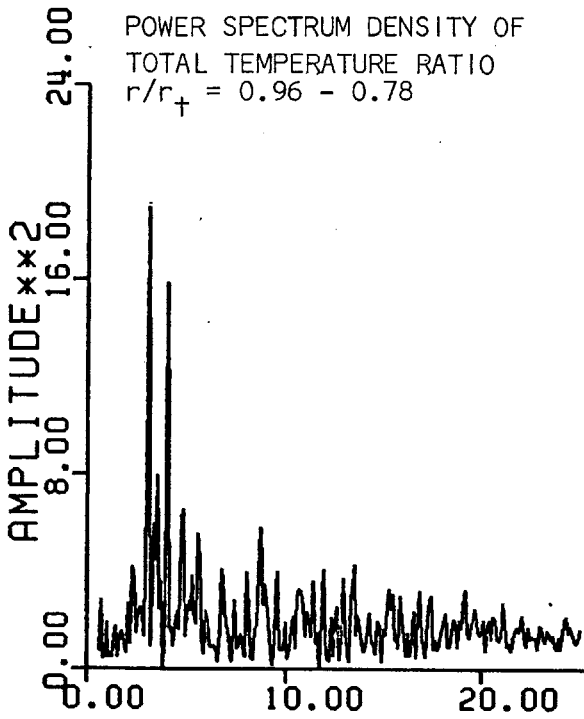
FIGURE 3.2.F   FREQUENCY SPECTRUM OF TOTAL TEMPERATURE RATIO & EFFICIENCY
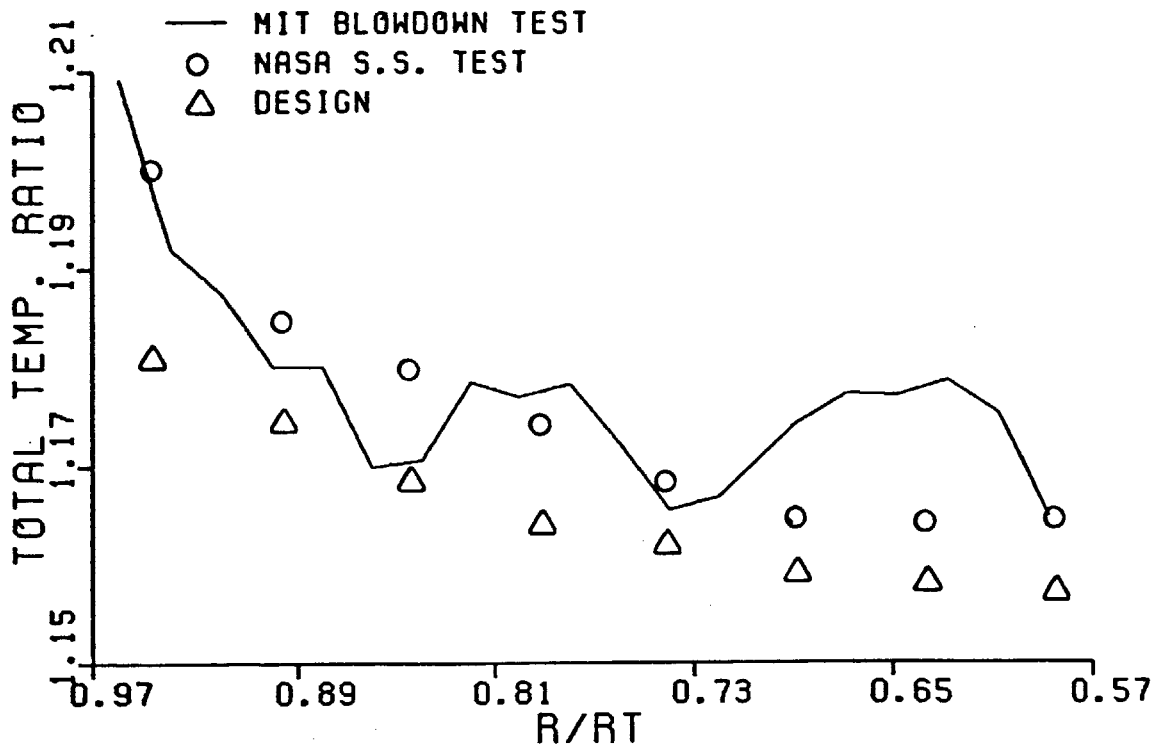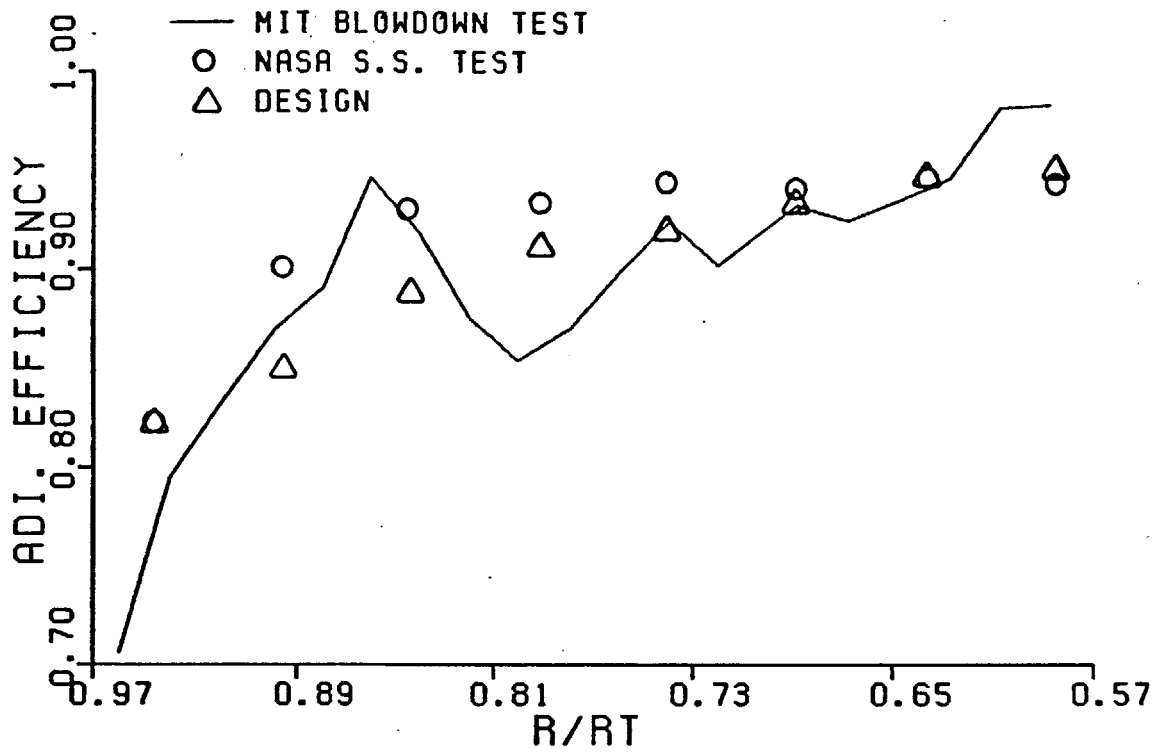
FIGURE 3.3.A   TIME AVERAGED EFFICIENCY & TOTAL TEMPERATURE RATIOS
      VS. RADIUS RATIO BEHIND THE ROTOR
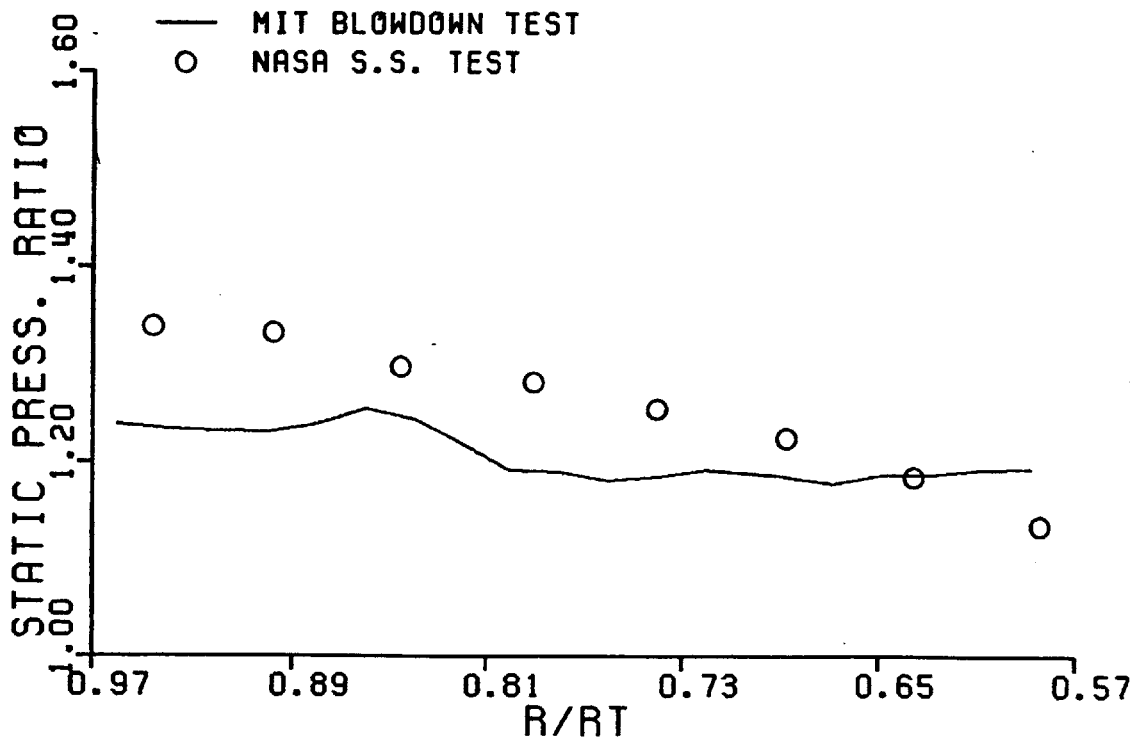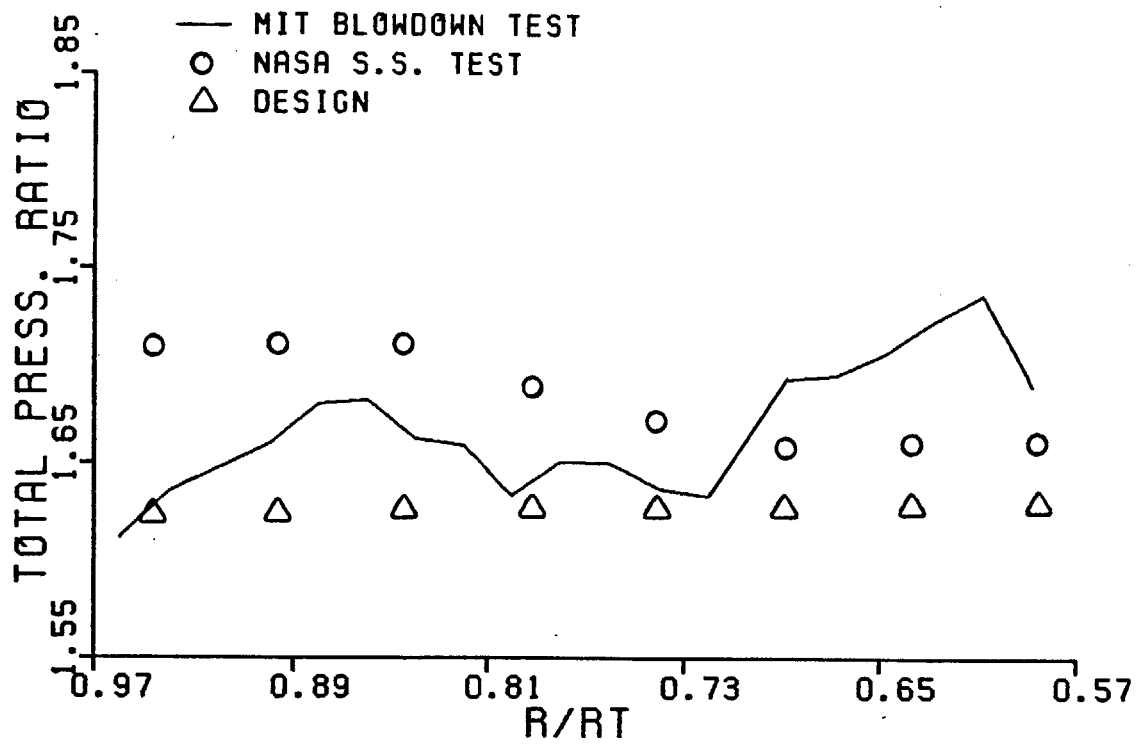
FIGURE 3.3.B   TIME AVERAGED TOTAL & STATIC PRESSURE RATIOS VS. RADIUS
RATIO BEHIND THE ROTOR
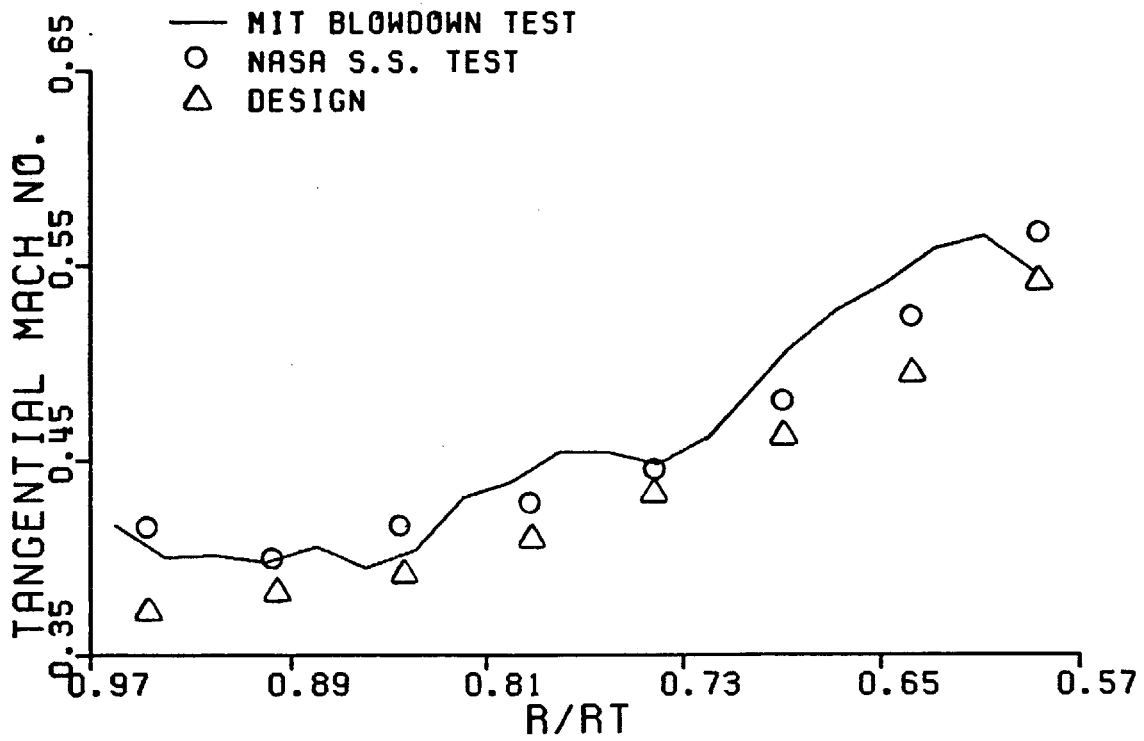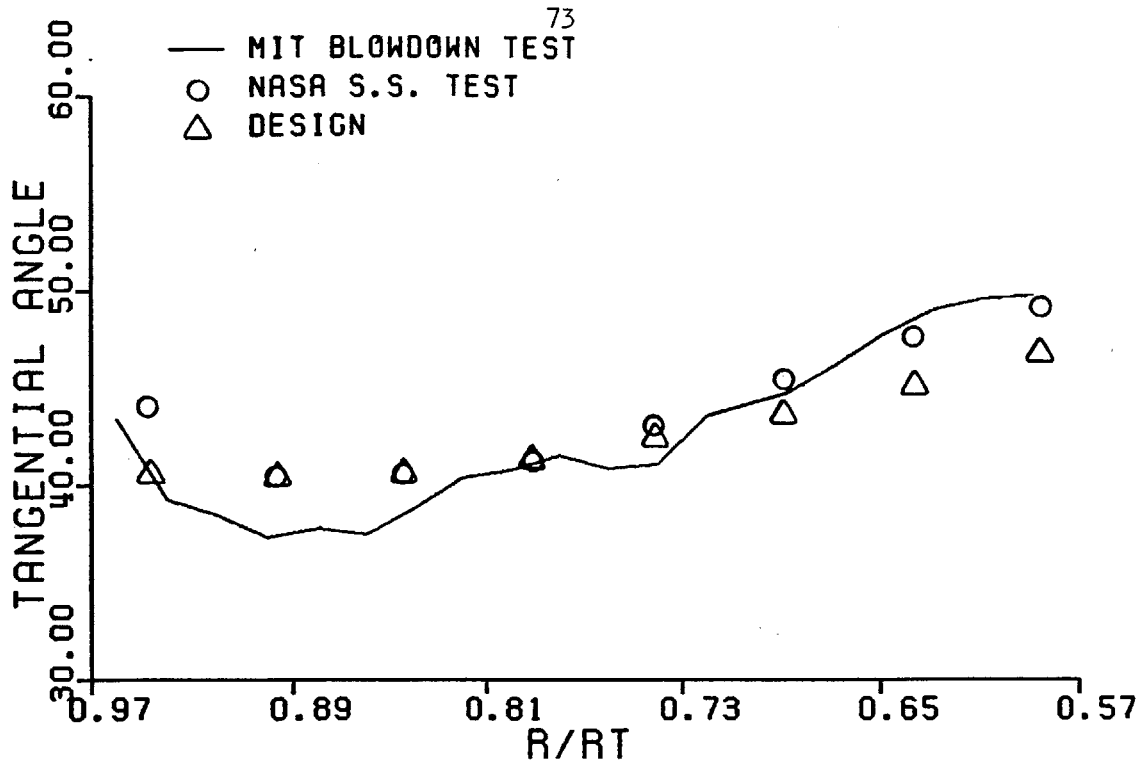
FIGURE 3.3.C   TIME AVERAGED TANGENTIAL ANGLE & TANGENTIAL MACH NUMBER
VS. RADIUS RATIO BEHIND THE ROTOR
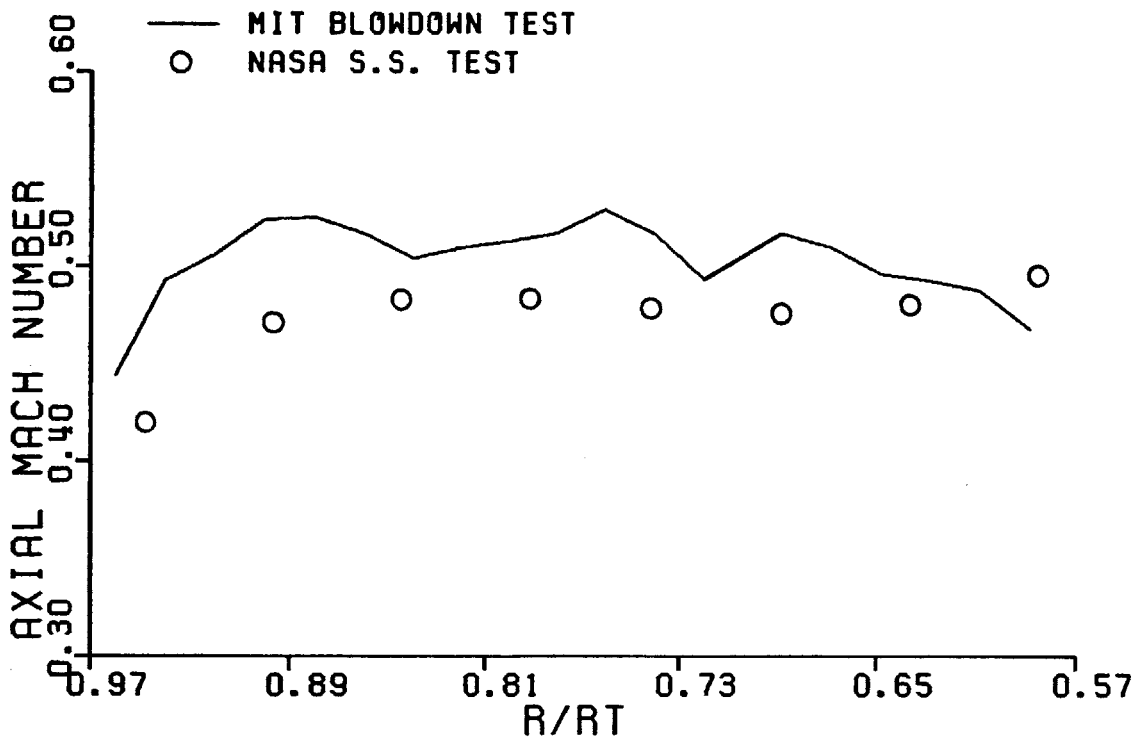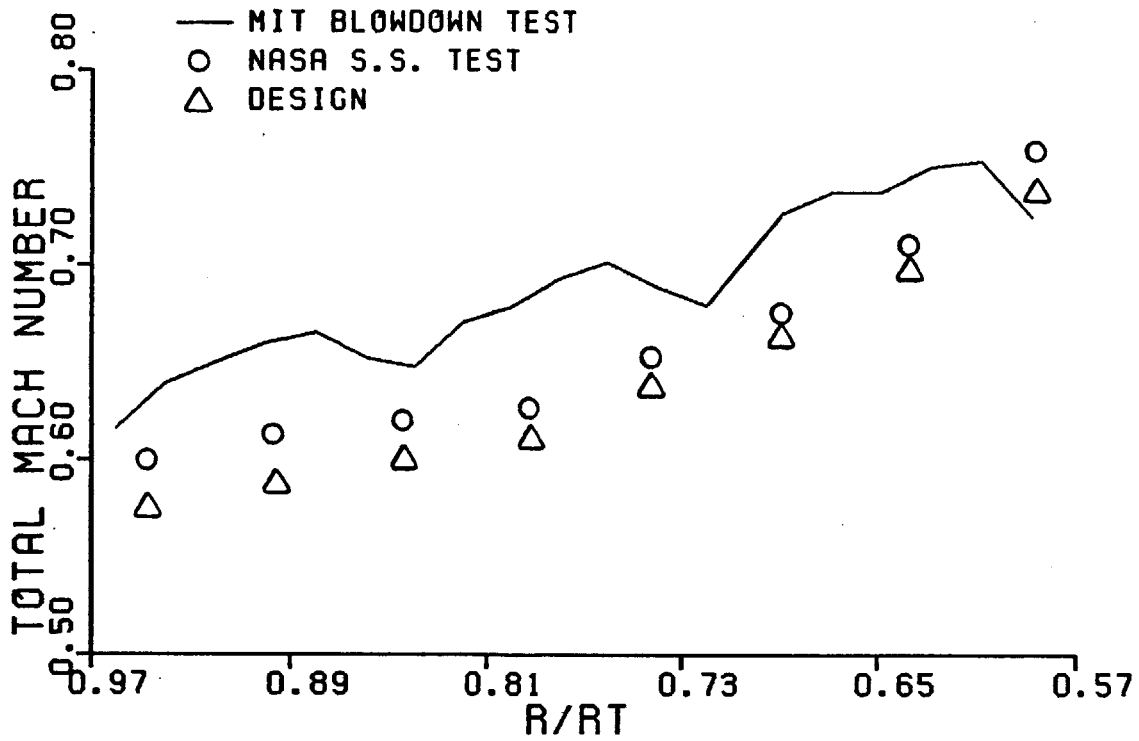
FIGURE 3.3.D   TIME AVERAGED TOTAL & AXIAL MACH NUMBER VS. RADIUS   RATIO
BEHIND THE ROTOR
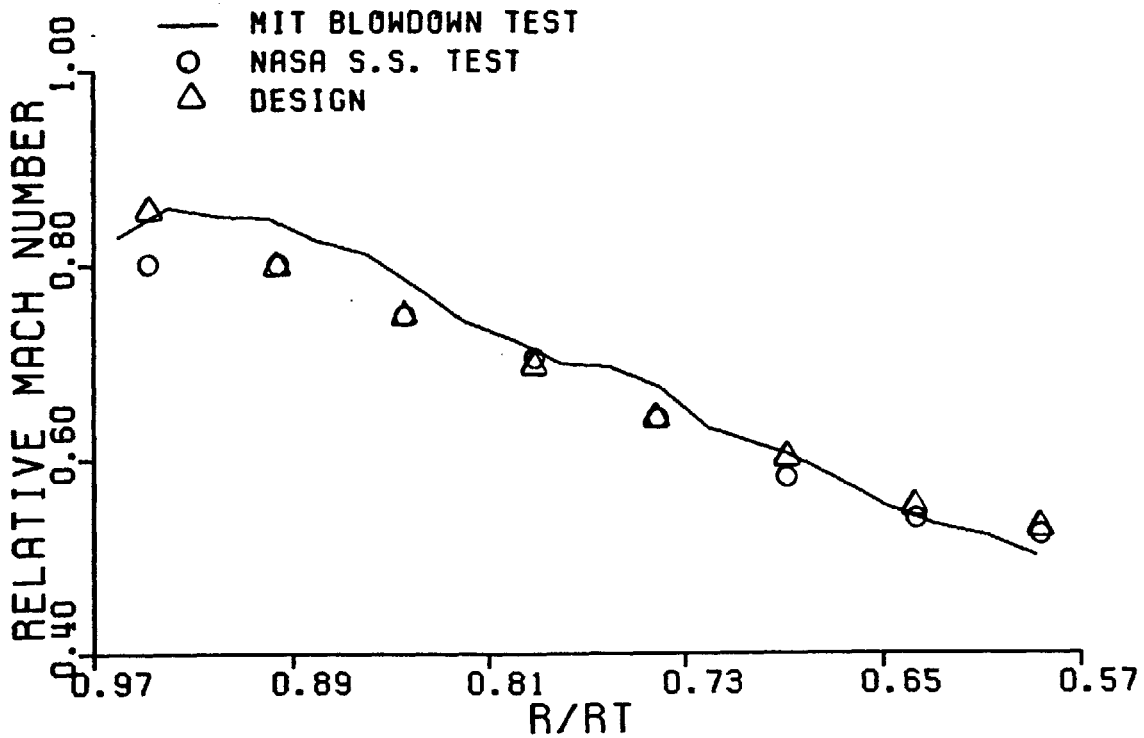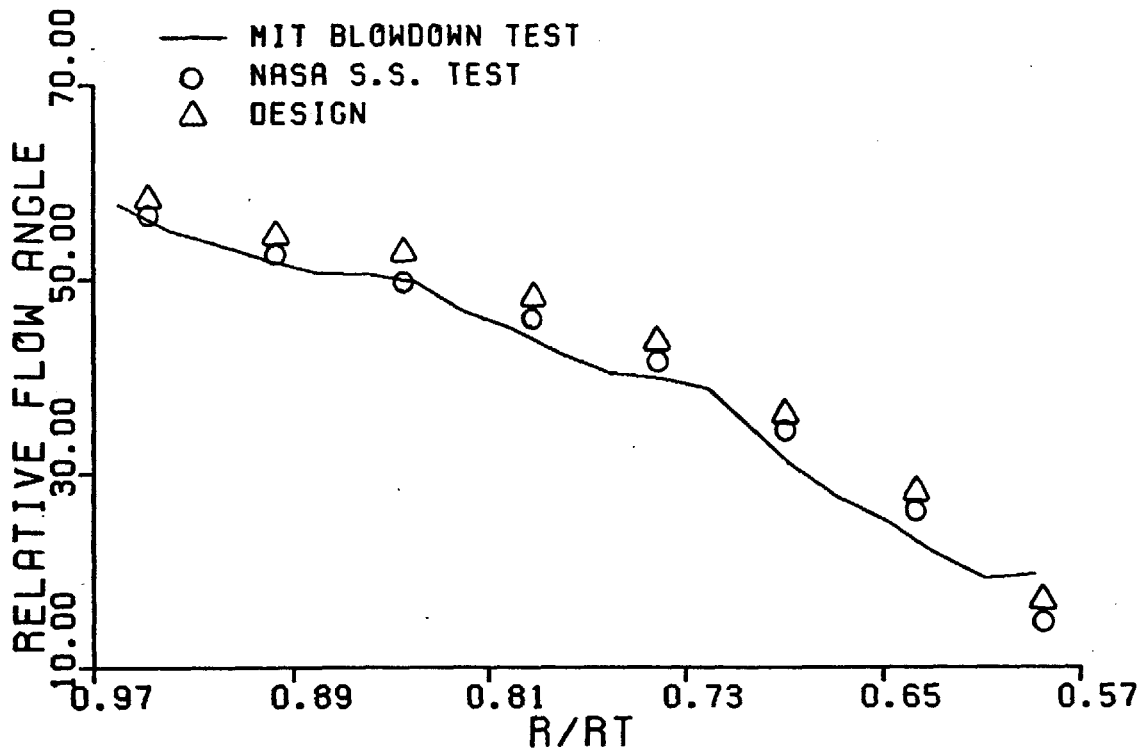
FIGURE 3.3.E TIME AVERAGED RELATIVE FLOW ANGLE & RELATIVE MACH NUMBER
VS. RADIUS RATIO BEHIND THE ROTOR
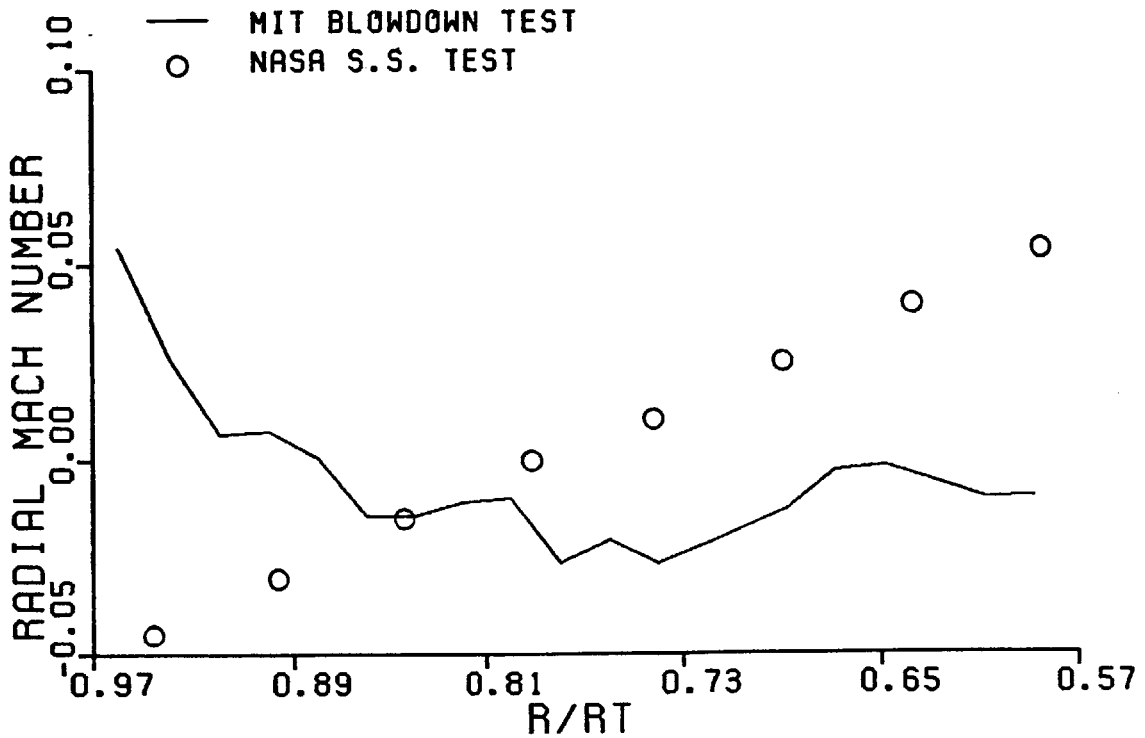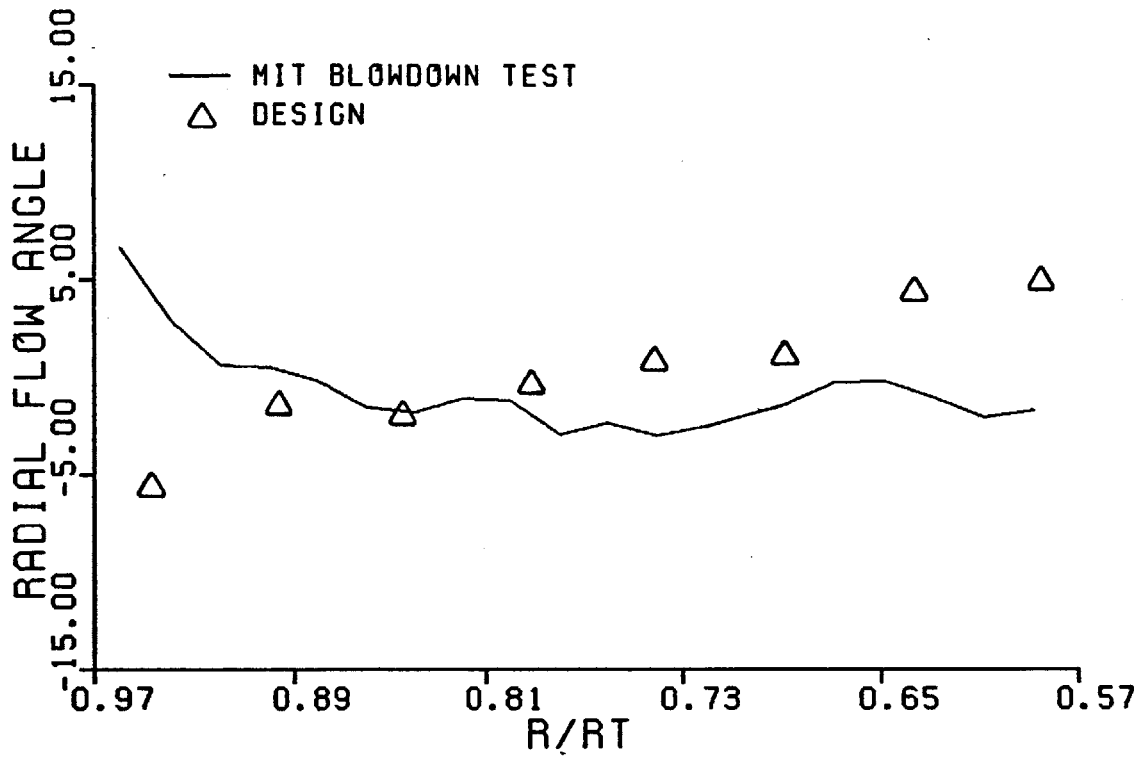
FIGURE 3.3.F   TIME AVERAGED RADIAL FLOW ANGLE AND RADIAL MACH NUMBER
VS. RADIUS RATIO BEHIND THE ROTOR

TOTAL PRESSURE RATIO MAP
BEHIND ROTOR, 5 CYCLE AVERAGED

Figure 3.4.A

77

STATIC PRESSURE RATIO MAP
BEHIND ROTOR, 5 CYCLE AVERAGED

Rotation

Figure·3.4.B

>1.30

1.30-1.26

1.26-1.20

1.20-1.16

1.16-1.13

1.13-1.10

<1.10

78
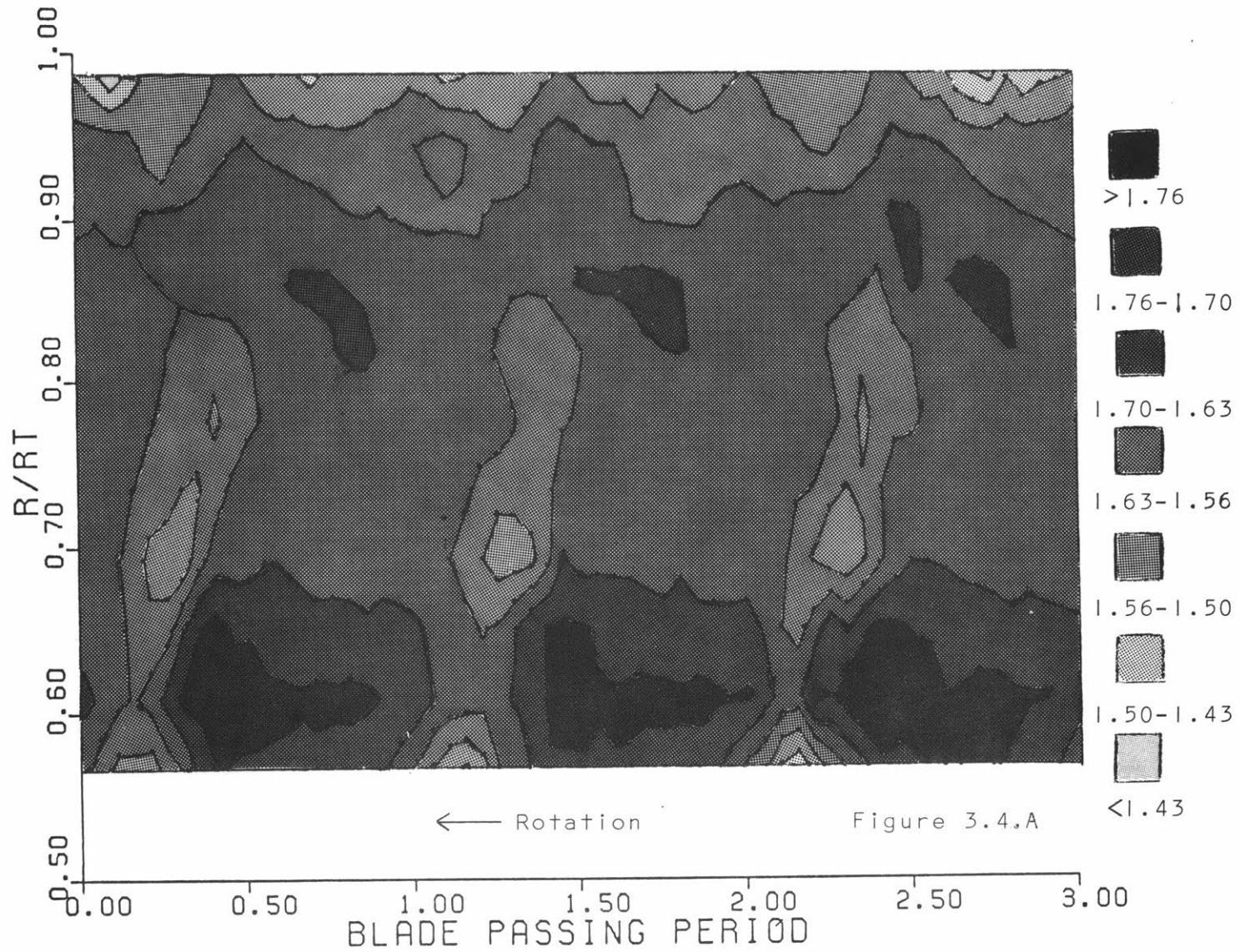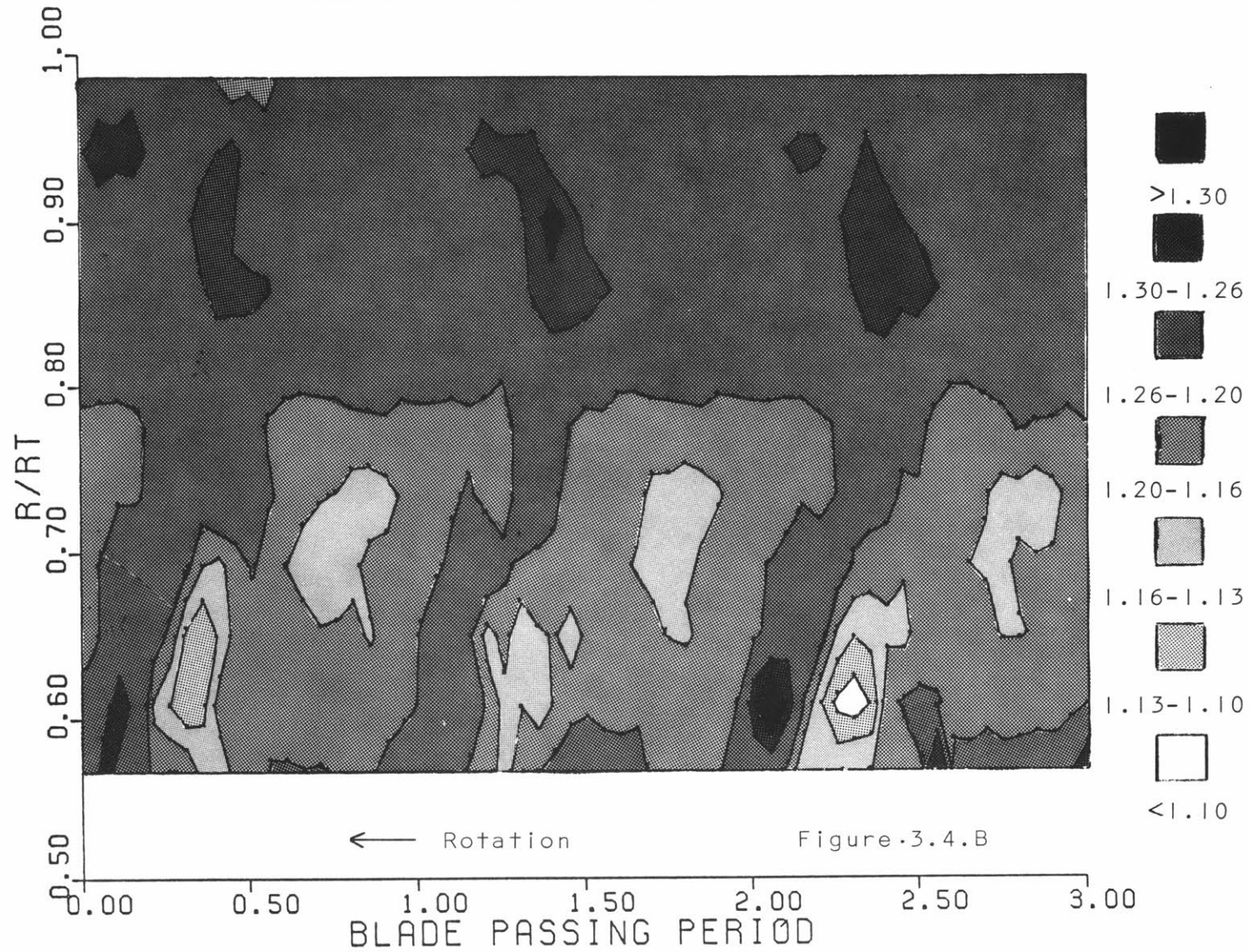
TOTAL TEMPERATURE RATIO MAP
BEHIND ROTOR, 5 CYCLE AVERAGED

Rotation

Figure 3.4.C

>1.23

1.23-1.22

1.22-1.20

1.20-1.18

1.18-1.17

1.17-1.15

<1.15

R/RT

BLADE PASSING PERIOD
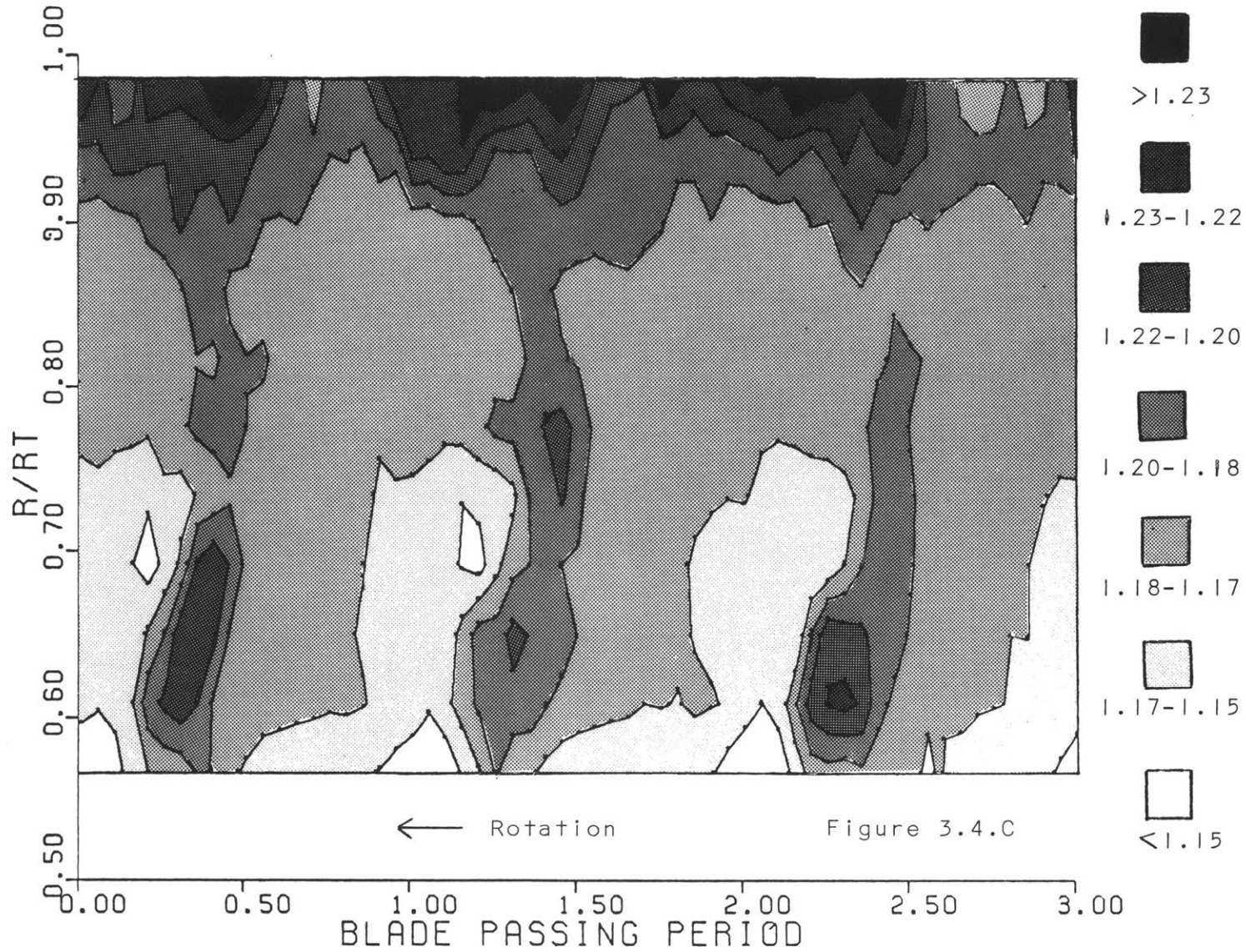
TOTAL EFFICIENCY MAP
BEHIND ROTOR, 5 CYCLE AVERAGED
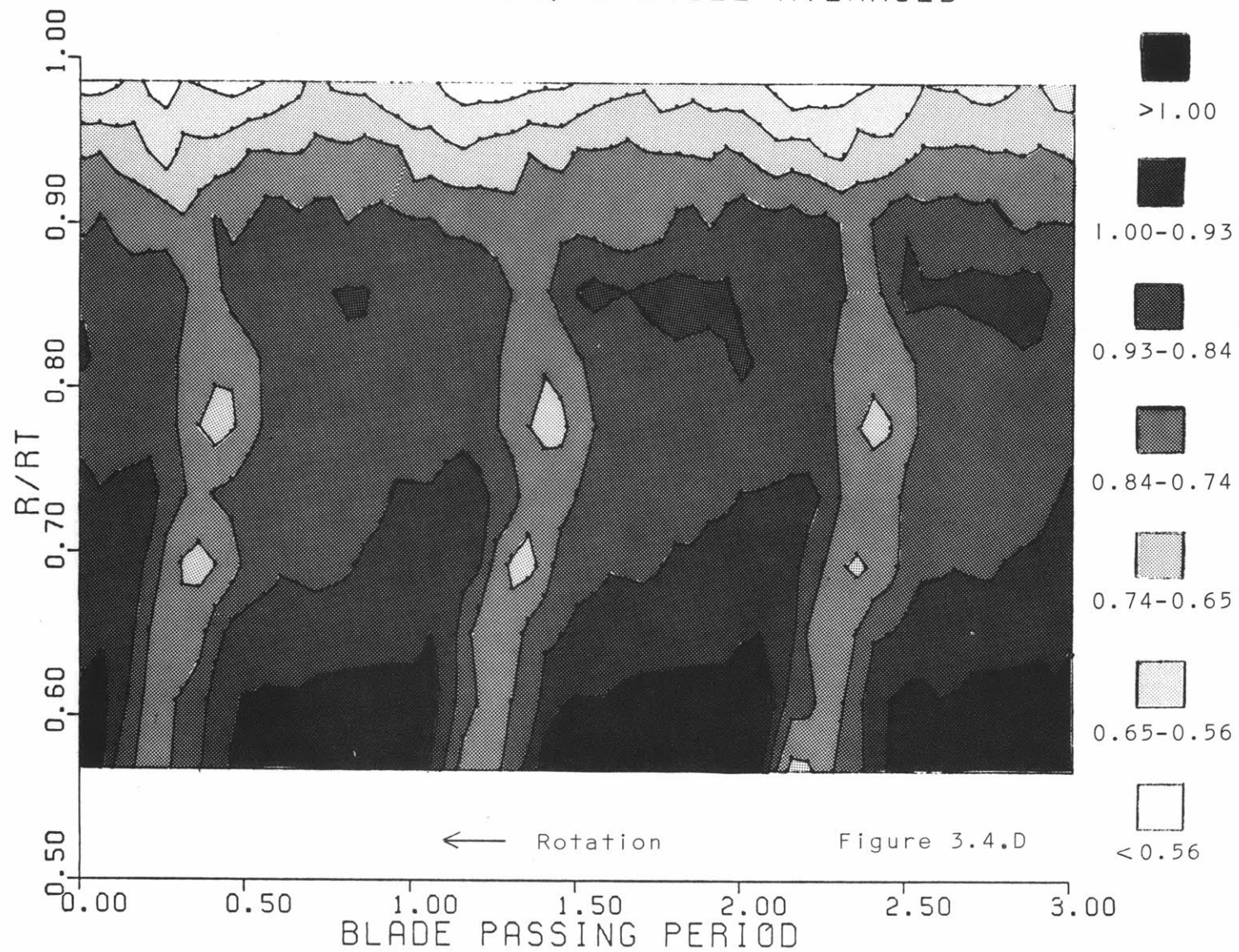
Figure 3.4.D

TOTAL MACH NUMBER MAP
BEHIND ROTOR, 5 CYCLE AVERAGED
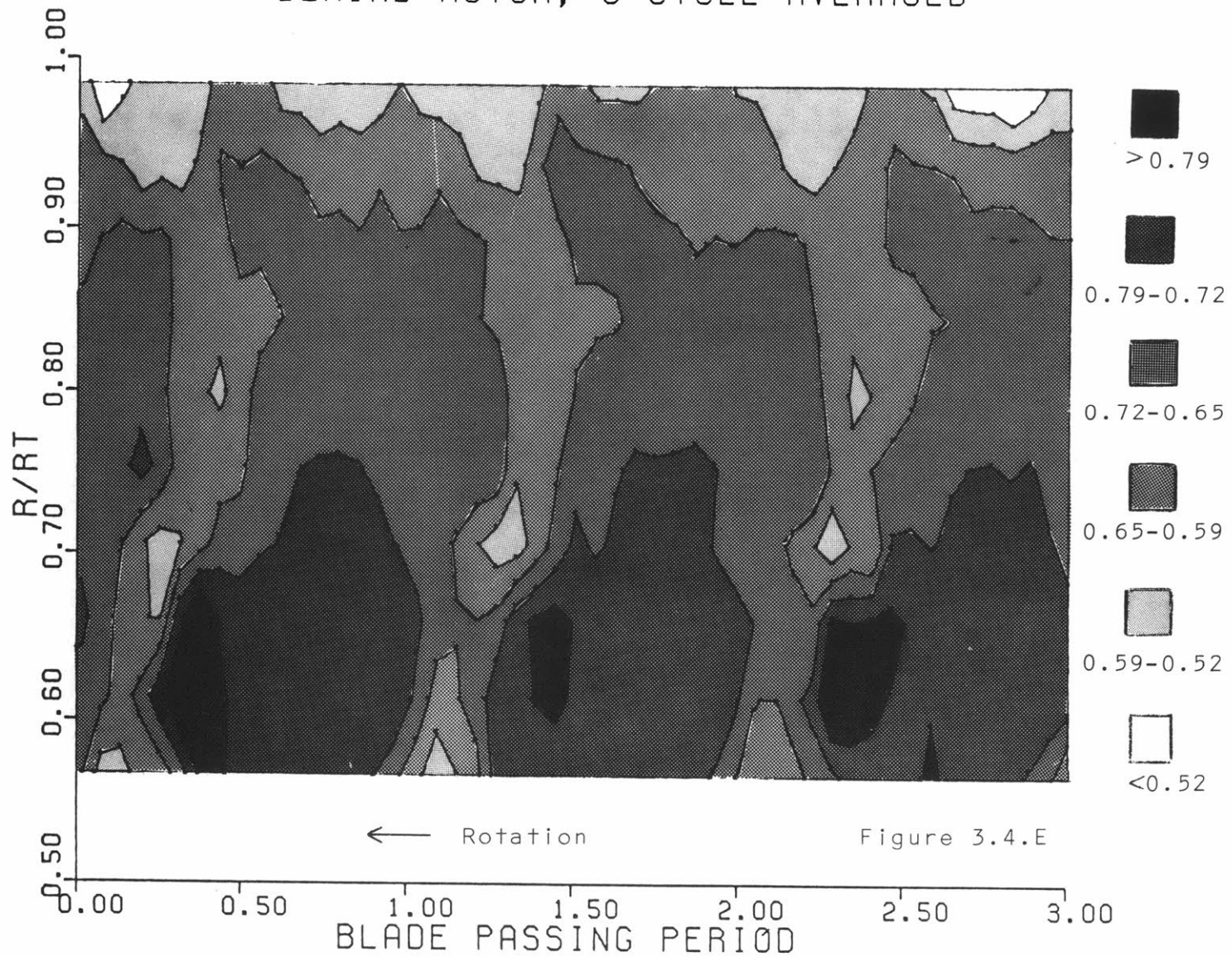
> 0.79

0.79 - 0.72

0.72 - 0.65

0.65 - 0.59

0.59 - 0.52

< 0.52

← Rotation

Figure 3.4.E

R/RT

BLADE PASSING PERIOD

AXIAL MACH NUMBER MAP
BEHIND ROTOR, 5 CYCLE AVERAGED

Legend:

■	>0.57
■	0.57-0.50
▨	0.50-0.44
▨	0.44-0.37
□	0.37-0.30
□	<0.30

←— Rotation

Figure 3.4.F

TANGENTIAL MACH NUMBER MAP
BEHIND ROTOR, 5 CYCLE AVERAGED

Figure 3.4.G

← Rotation

>0.67

0.67-0.60

0.60-0.54

0.54-0.48

0.48-0.41

0.41-0.35

<0.35
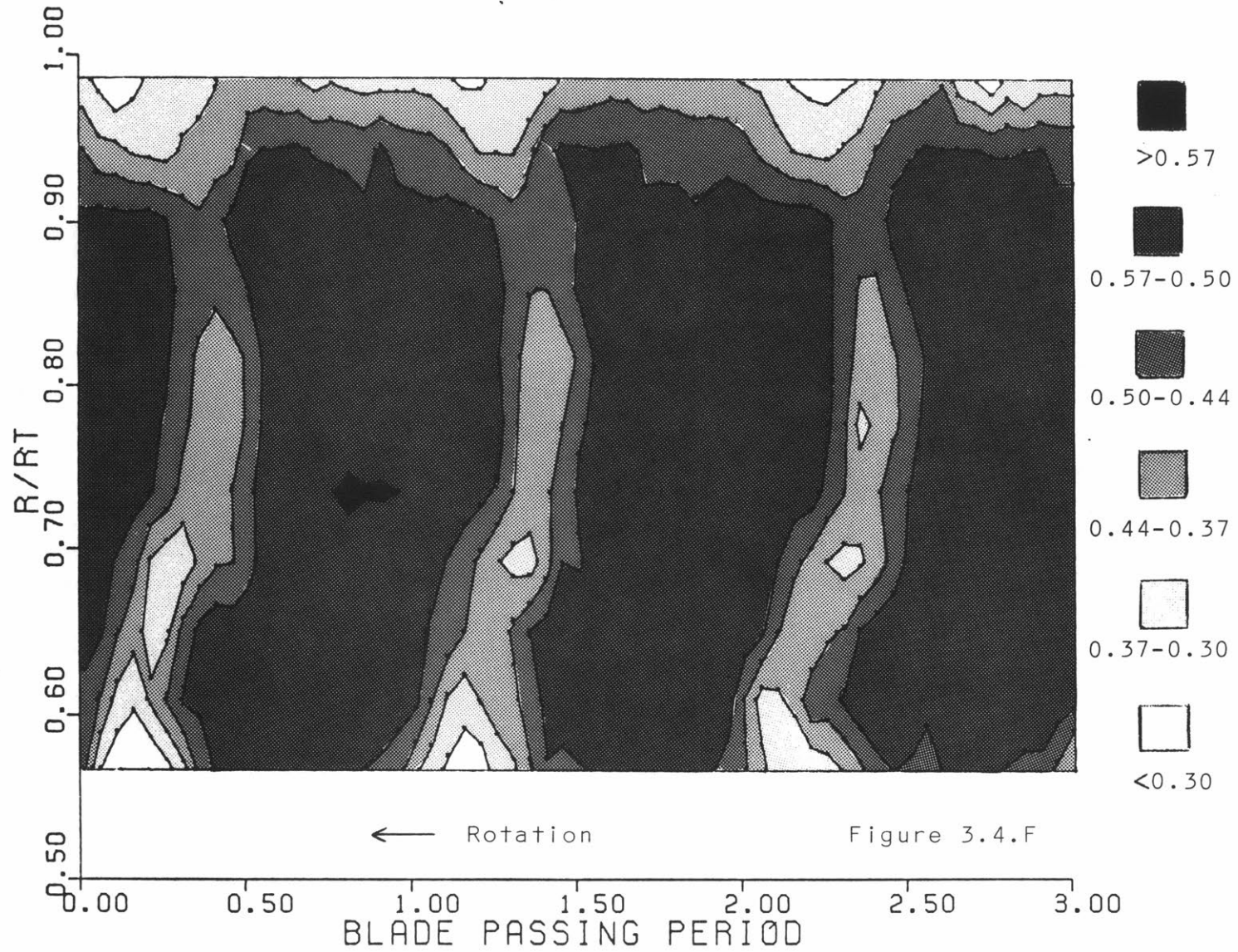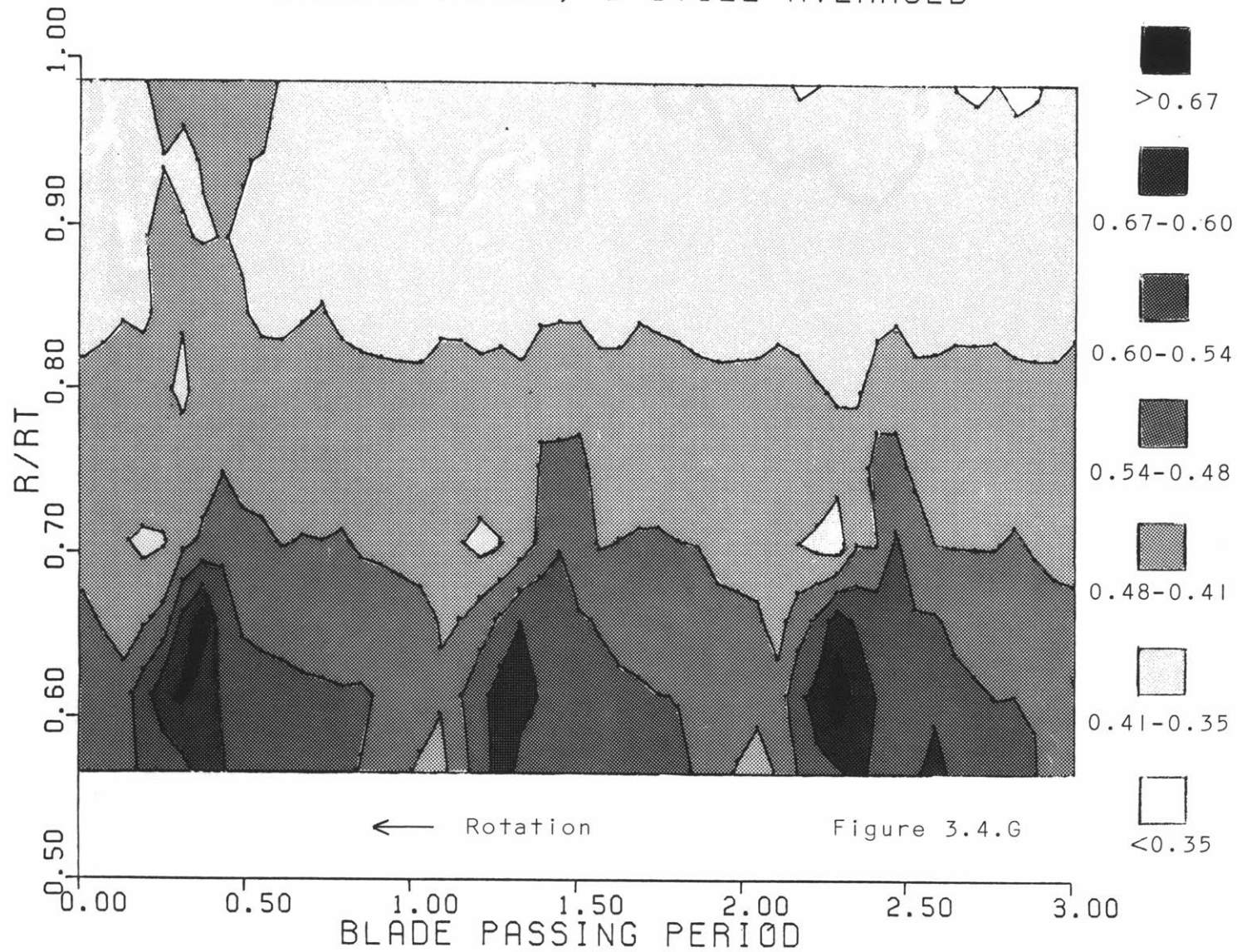
RADIAL MACH NUMBER MAP
BEHIND RØTØR, 5 CYCLES AVERAGED
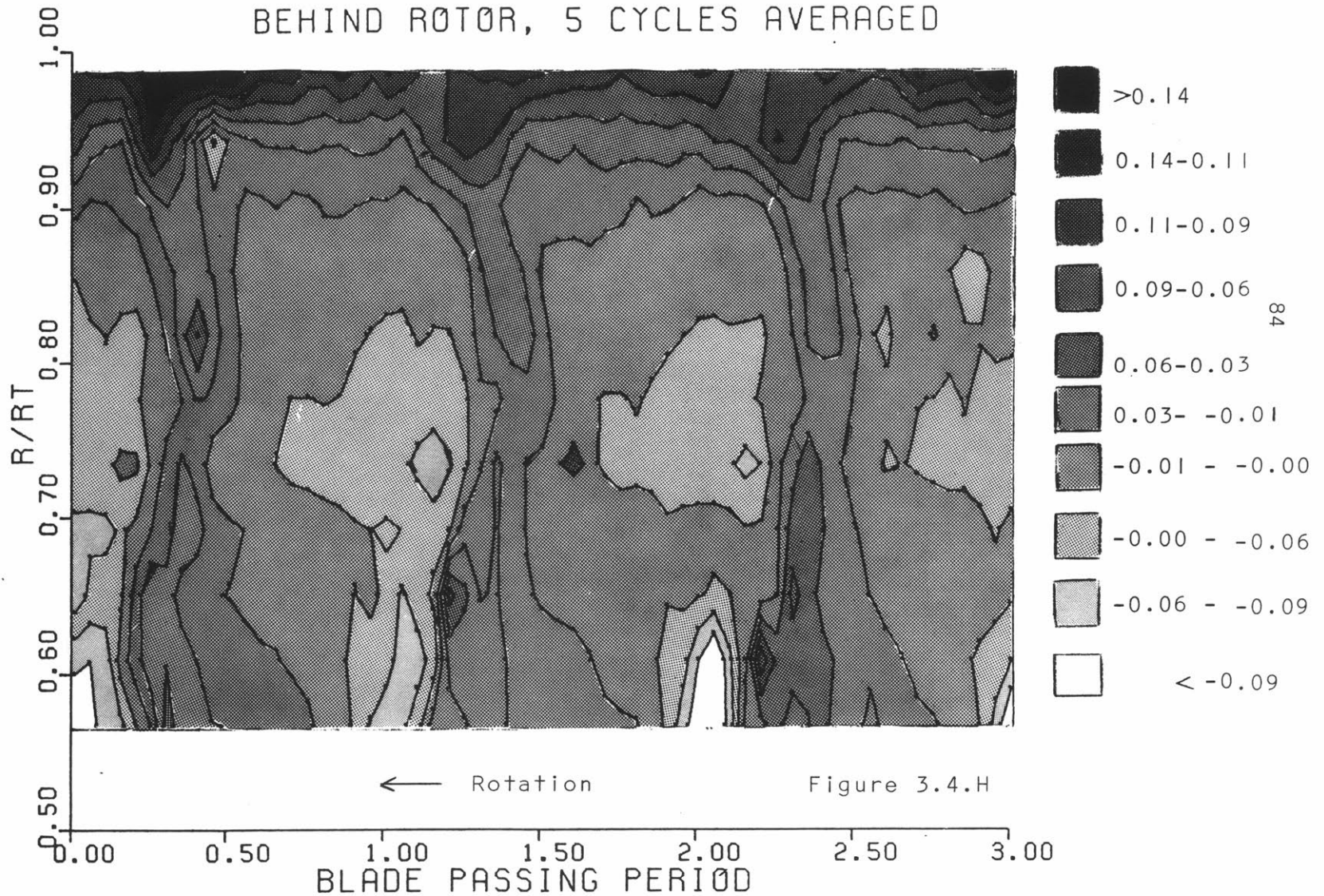
Figure 3.4.H

STREAMWISE VORTICITY MAP
BEHIND ROTOR, 5 CYCLE AVERAGED

Figure 3.4.1

← Rotation

BLADE PASSING PERIOD

R/RT

< -3.0

-3.0 - -2.4

-2.4 - -1.9

-1.9 - -1.3

-1.3 - -0.7

-0.7 - 2.1

2.1 - 2.7

2.7 - 3.2

> 3.2

85
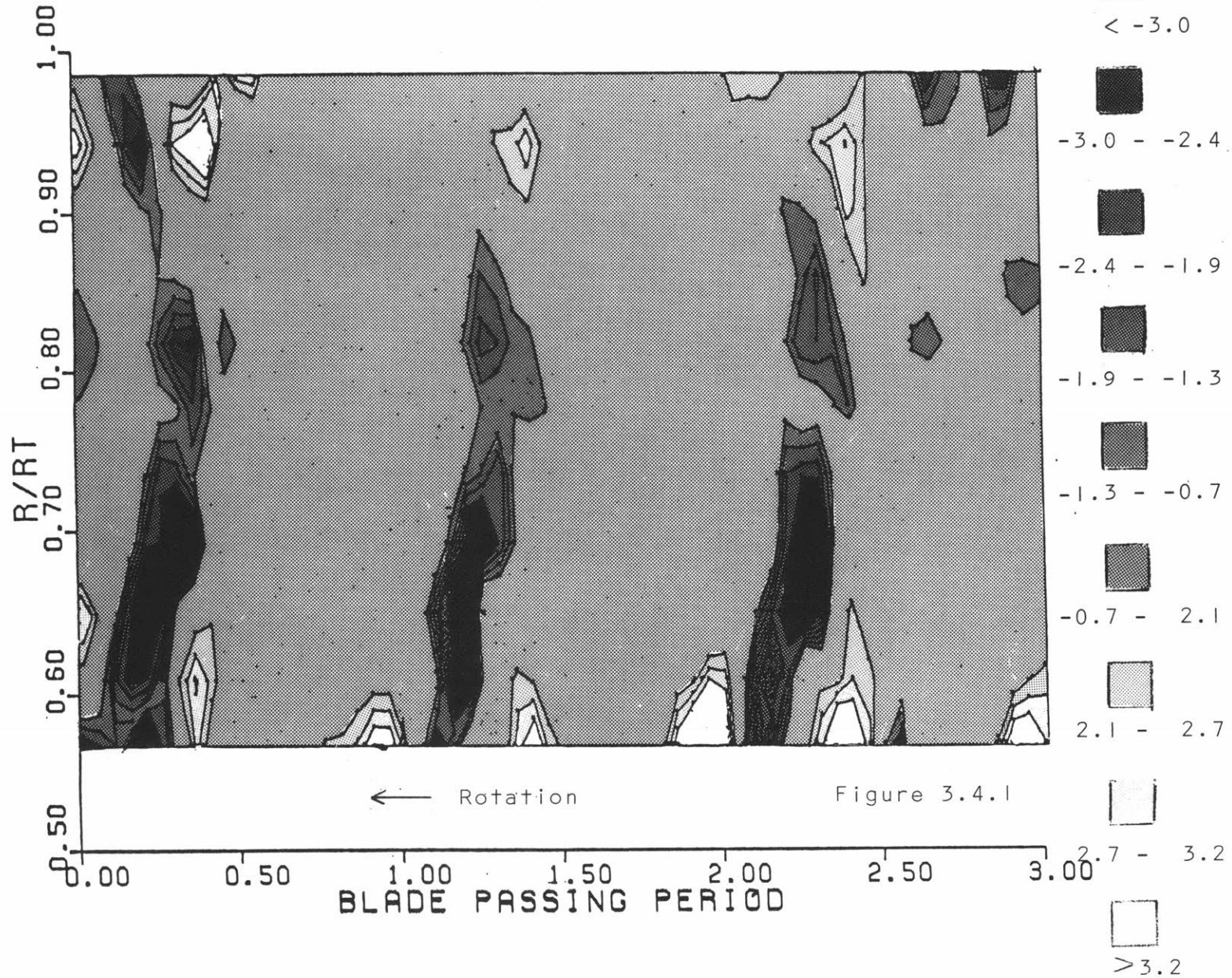
TANGENTIAL FLOW ANGLE MAP
BEHIND ROTOR, 5 CYCLE AVERAGED
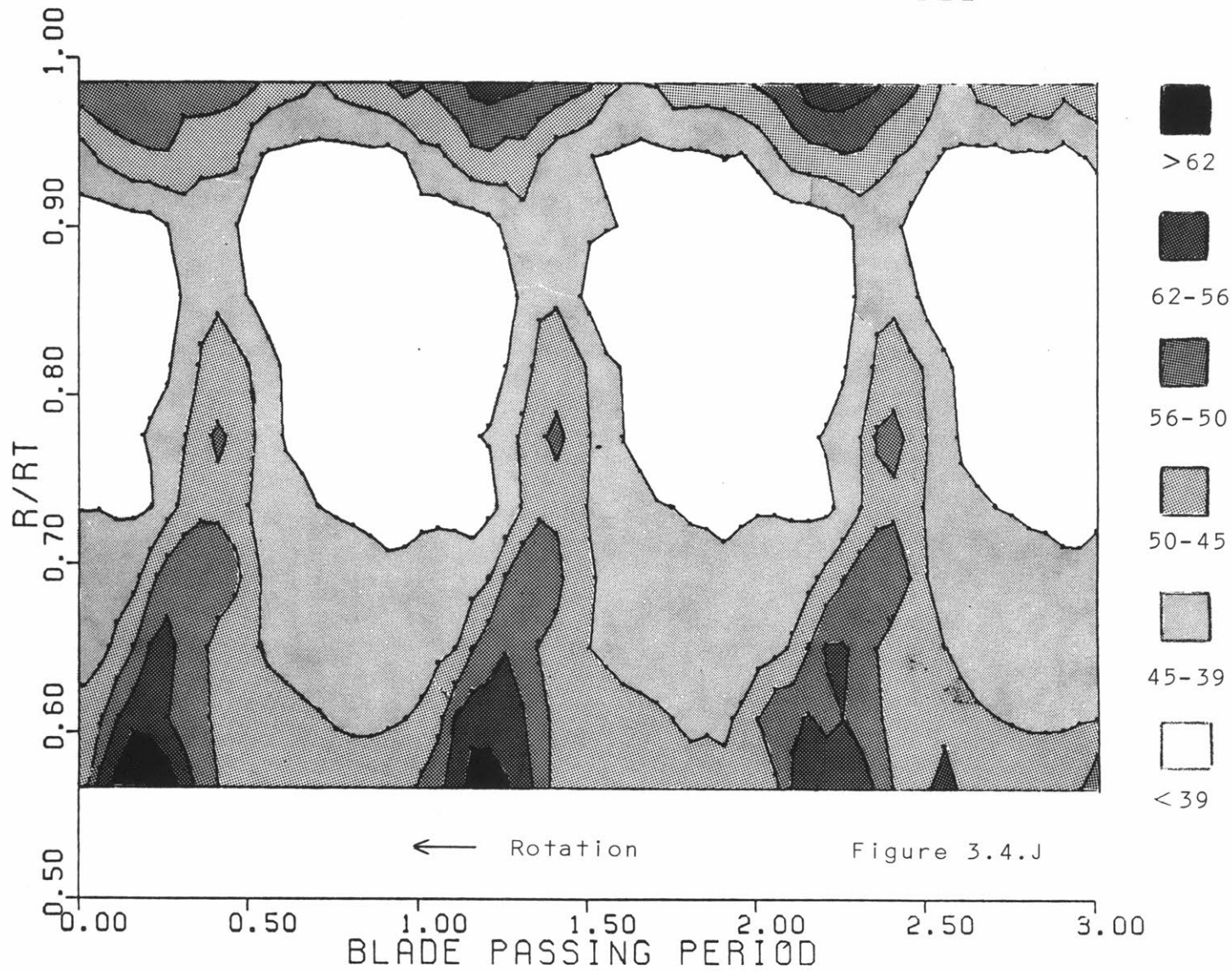
Figure 3.4.J

RADIAL FLOW ANGLE MAP
BEHIND ROTOR, 5 CYCLE AVERAGED

Figure 3.4.K

RELATIVE MACH NUMBER MAP
BEHIND ROTOR, 5 CYCLE AVERAGED

>0.79

0.79-0.70

0.70-0.60

0.60-0.51

0.51-0.41

<0.31

Rotation

Figure 3.4.L

R/RT

BLADE PASSING PERIOD
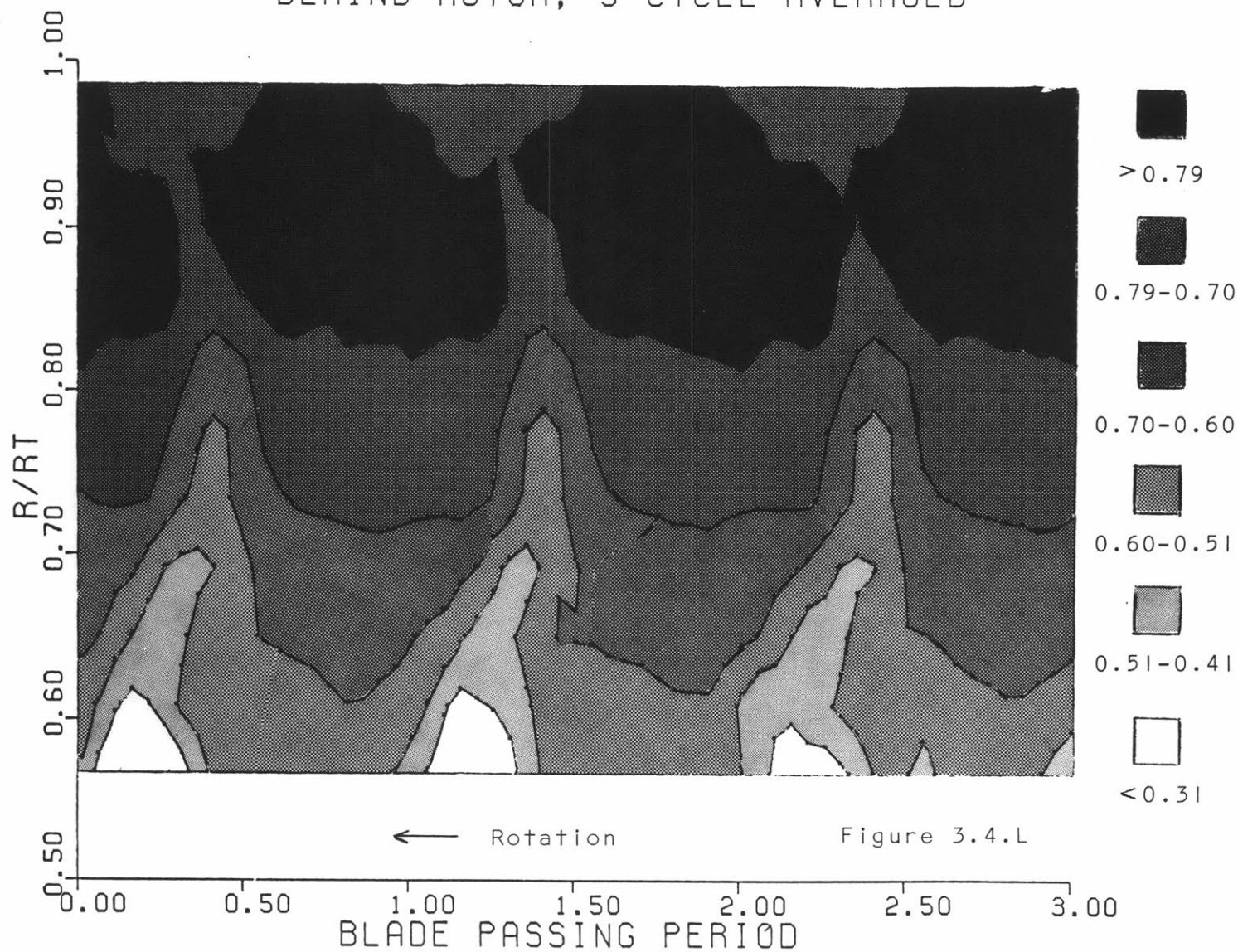
RELATIVE FLOW ANGLE MAP
BEHIND ROTOR, 5 CYCLE AVERAGED

← Rotation
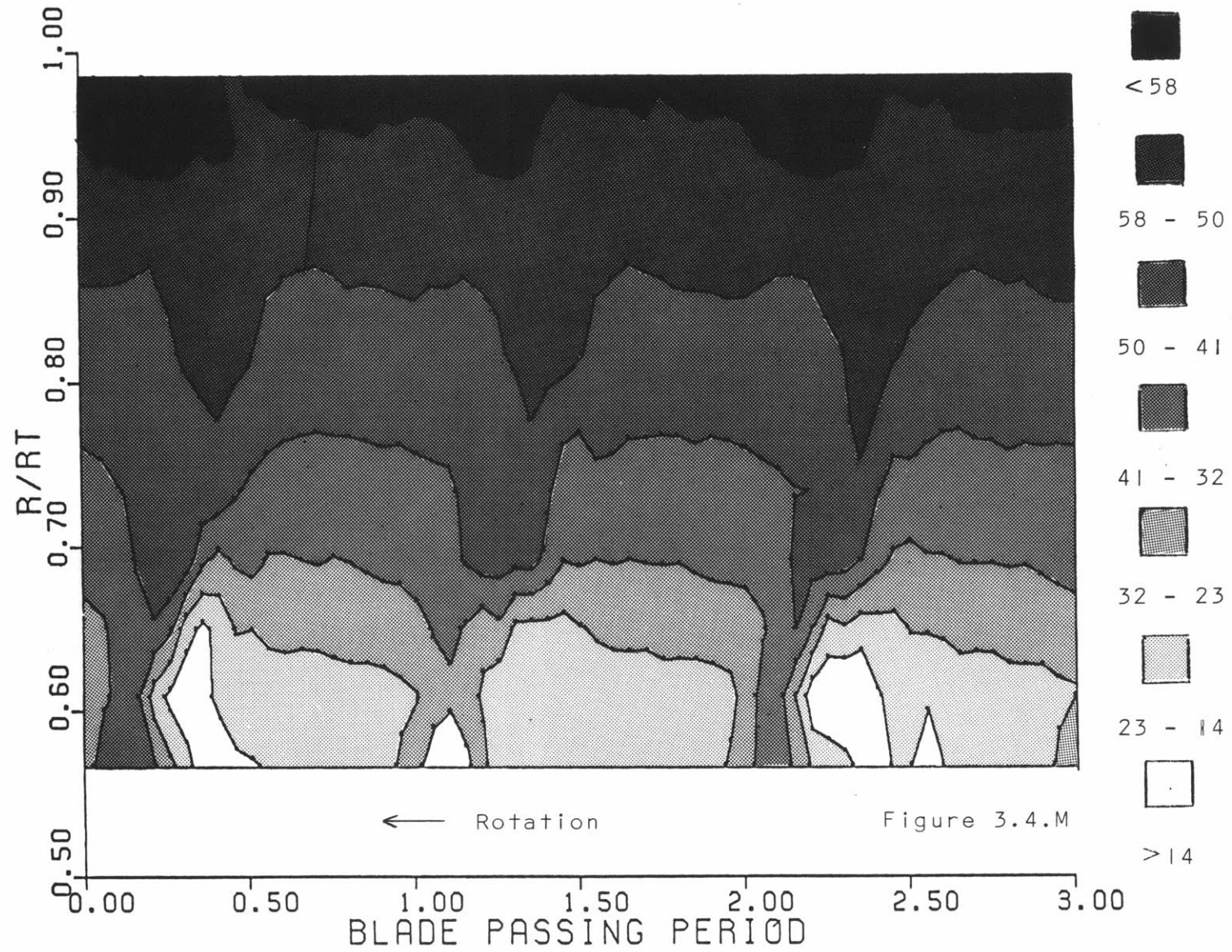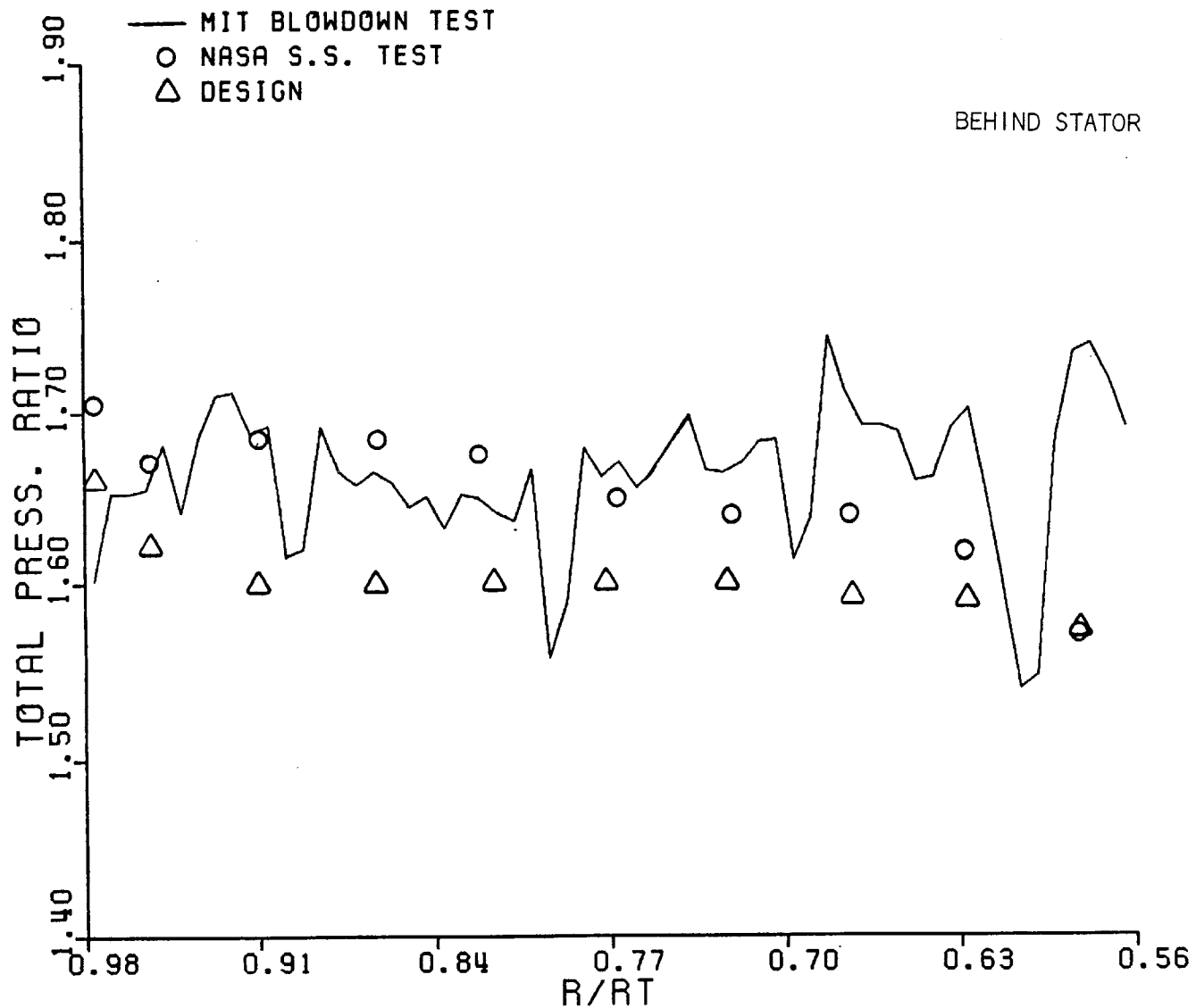
Figure 3.4.M

FIGURE 3.5   TIME AVERAGED TOTAL PRESSURE RATIO VS. RADIUS RATIOS BEHIND THE STATOR
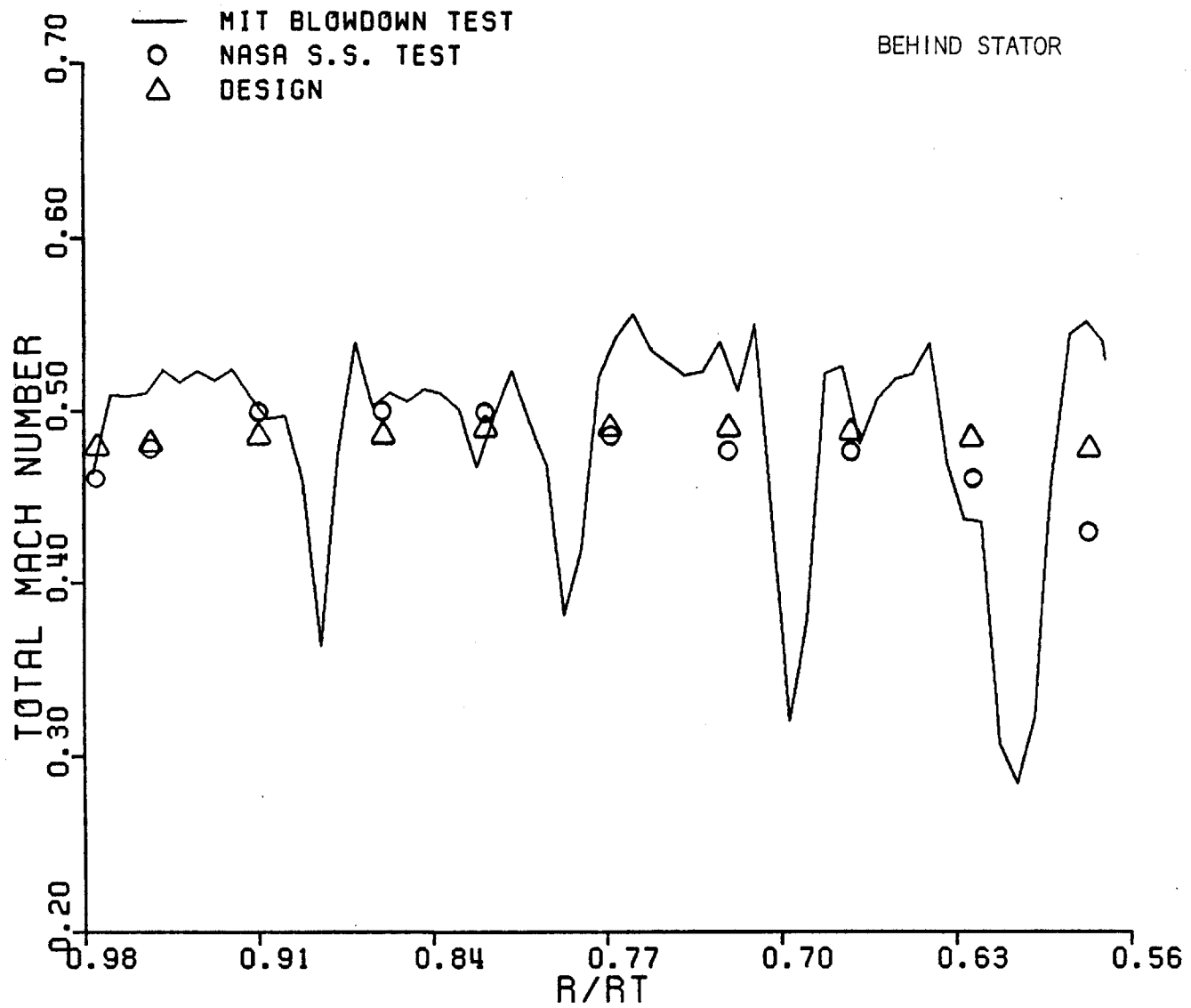
FIGURE 3.6   TIME AVERAGED TOTAL MACH NUMBER VS. RADIUS RATIOS BEHIND THE STATOR
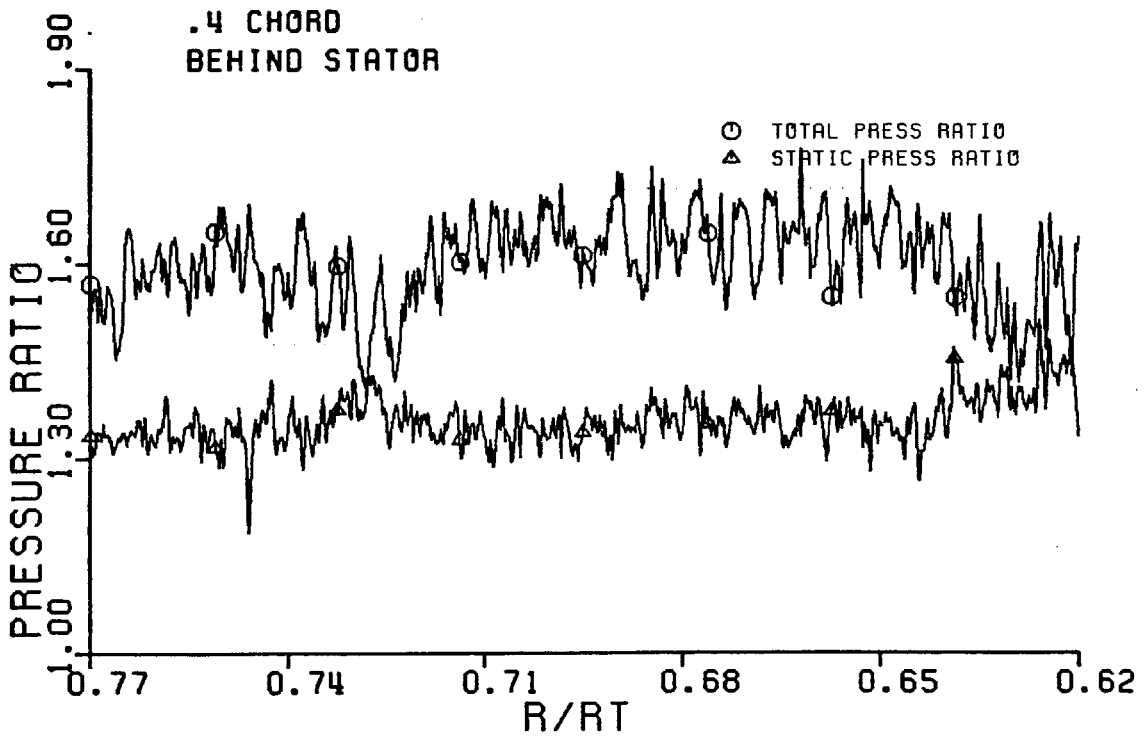
FIGURE 3.7.A   TOTAL AND STATIC PRESSURE RATIO BEHIND STATOR AT PORT 4

.4 CHORD
BEHIND STATOR
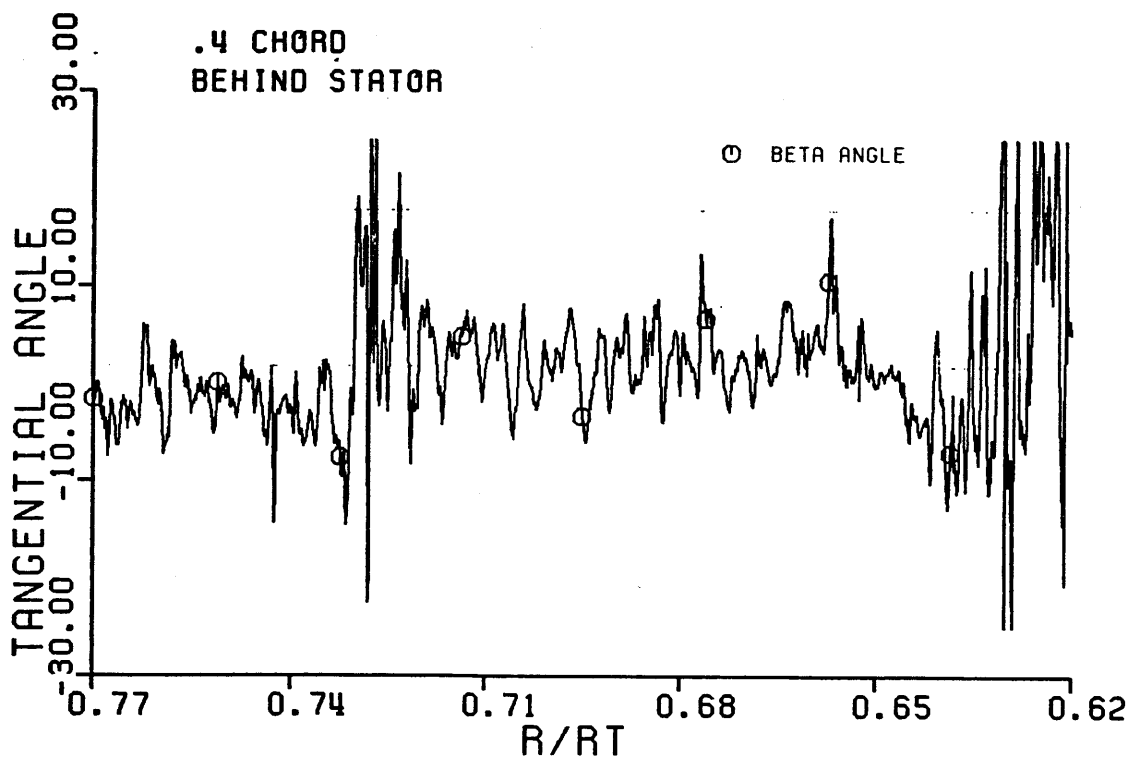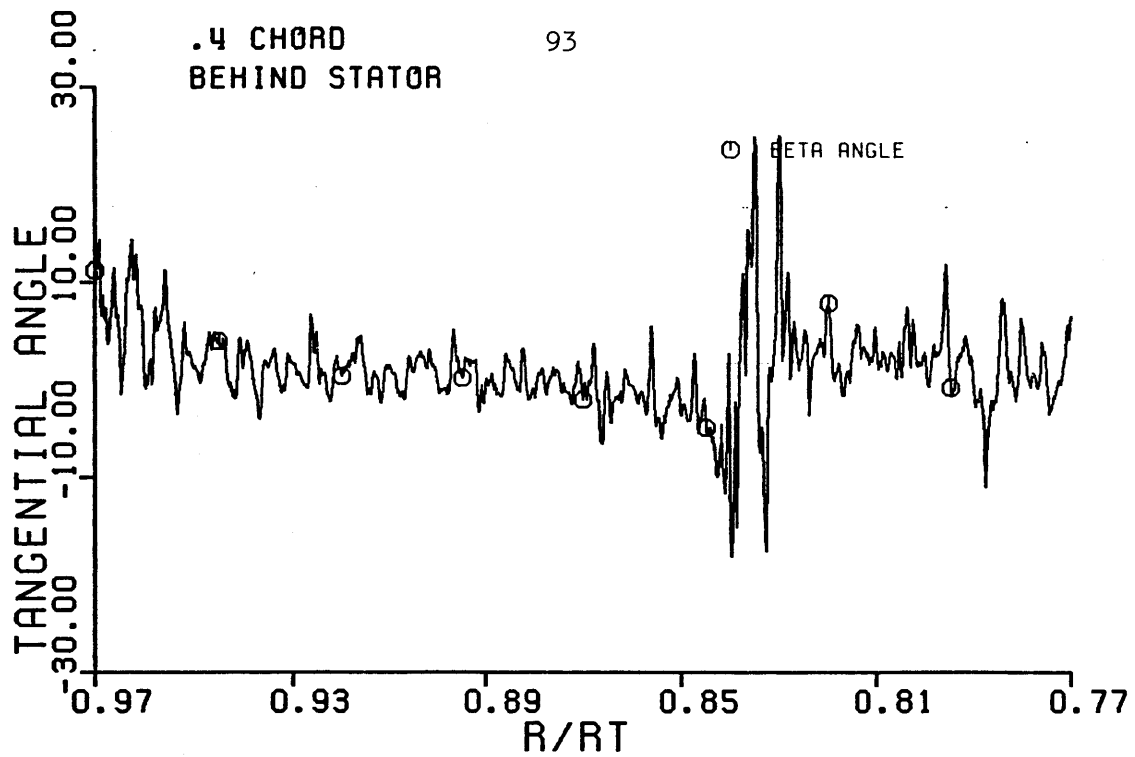
FIGURE 3.7.B   TANGENTIAL ANGLE BEHIND STATOR AT PORT 4
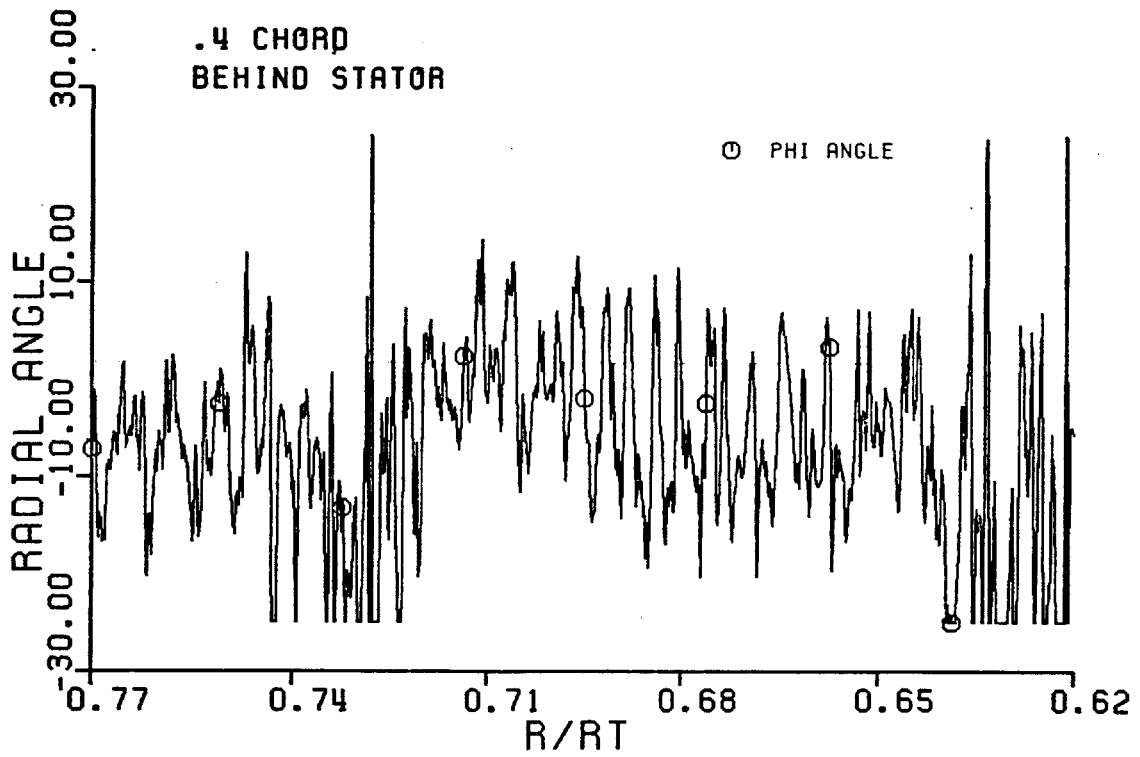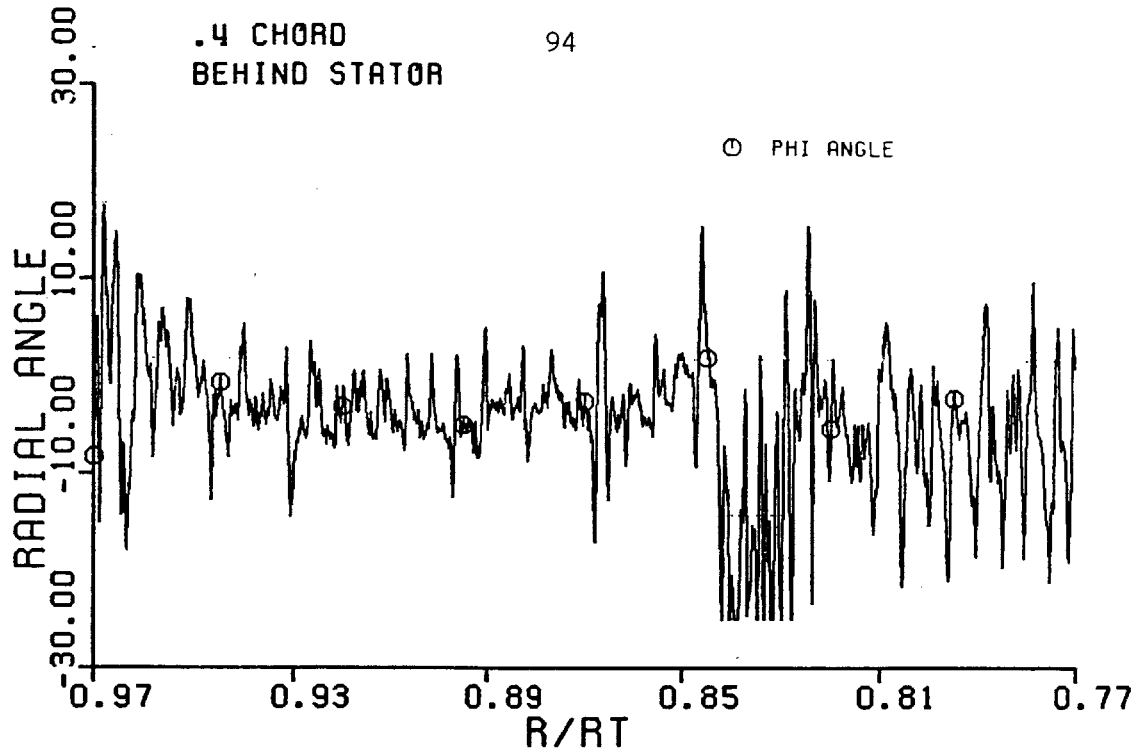
FIGURE 3.7.C   RADIAL ANGLE BEHIND STATOR AT PORT 4
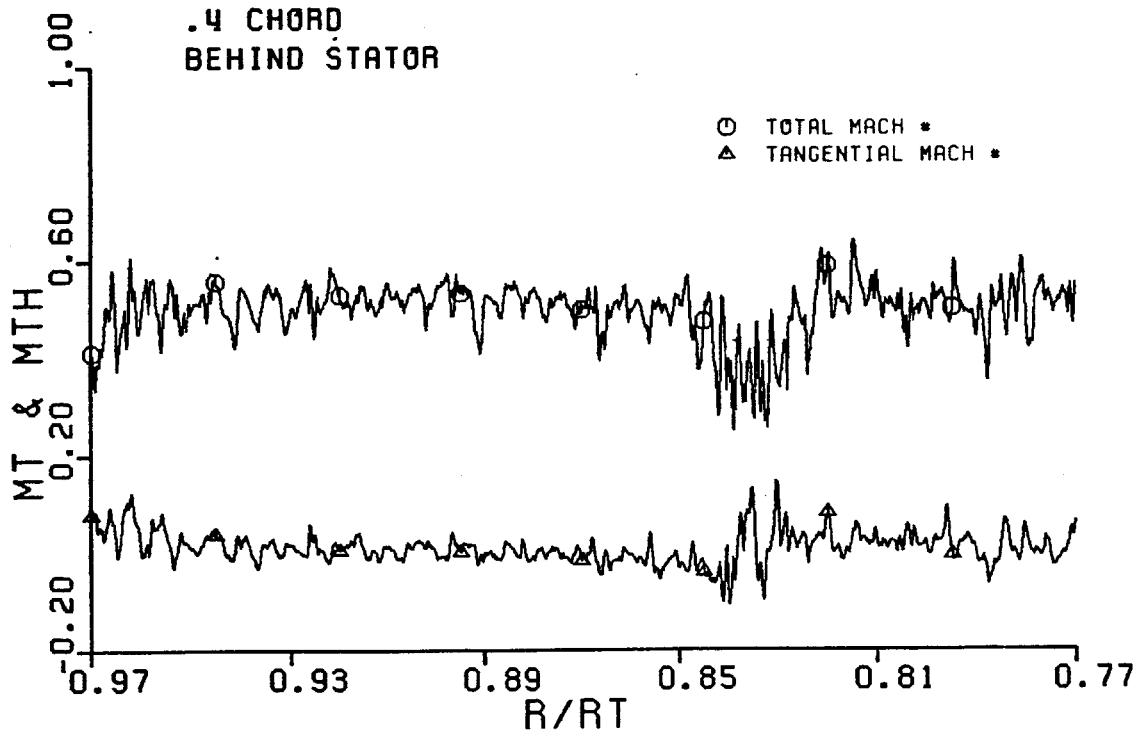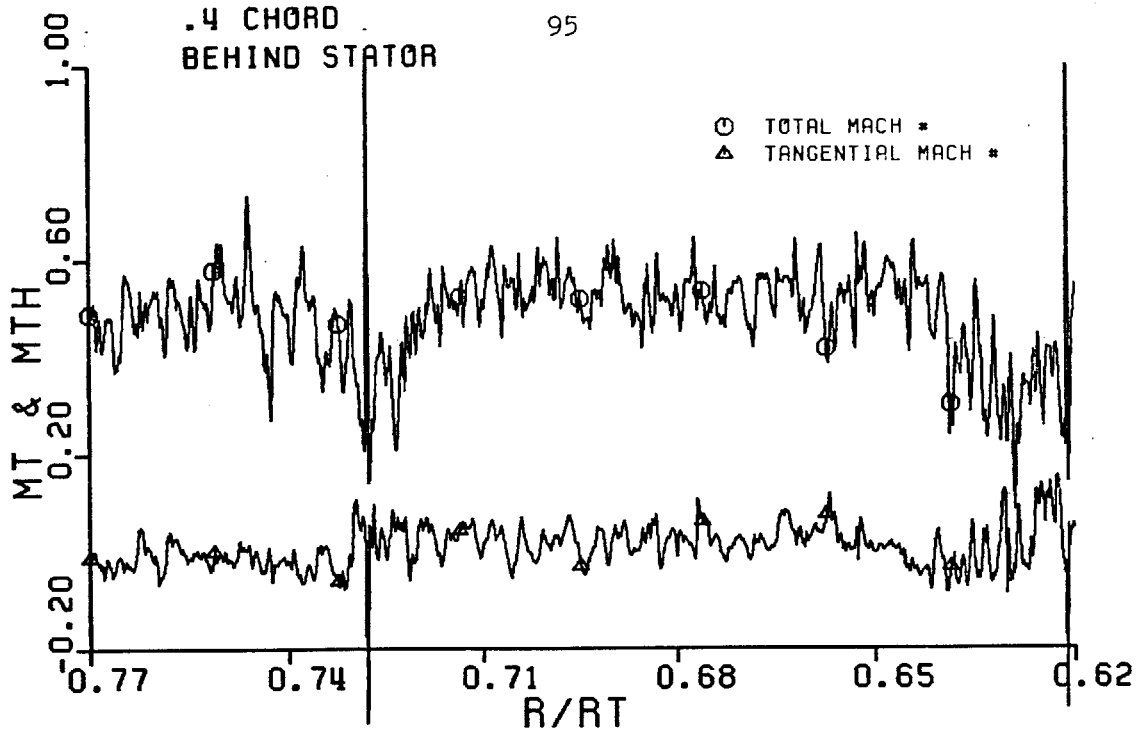
FIGURE 3.7.D   TOTAL & TANGENTIAL MACH NUMBER BEHIND STATOR AT PORT 4

.4 CHORD
BEHIND STATOR

○ AXIAL MACH #
△ RADIAL MACH #

MX & MPHI

R/RT

.4 CHORD
BEHIND STATOR

○ AXIAL MACH #
△ RADIAL MACH #

MX & MPHI

R/RT
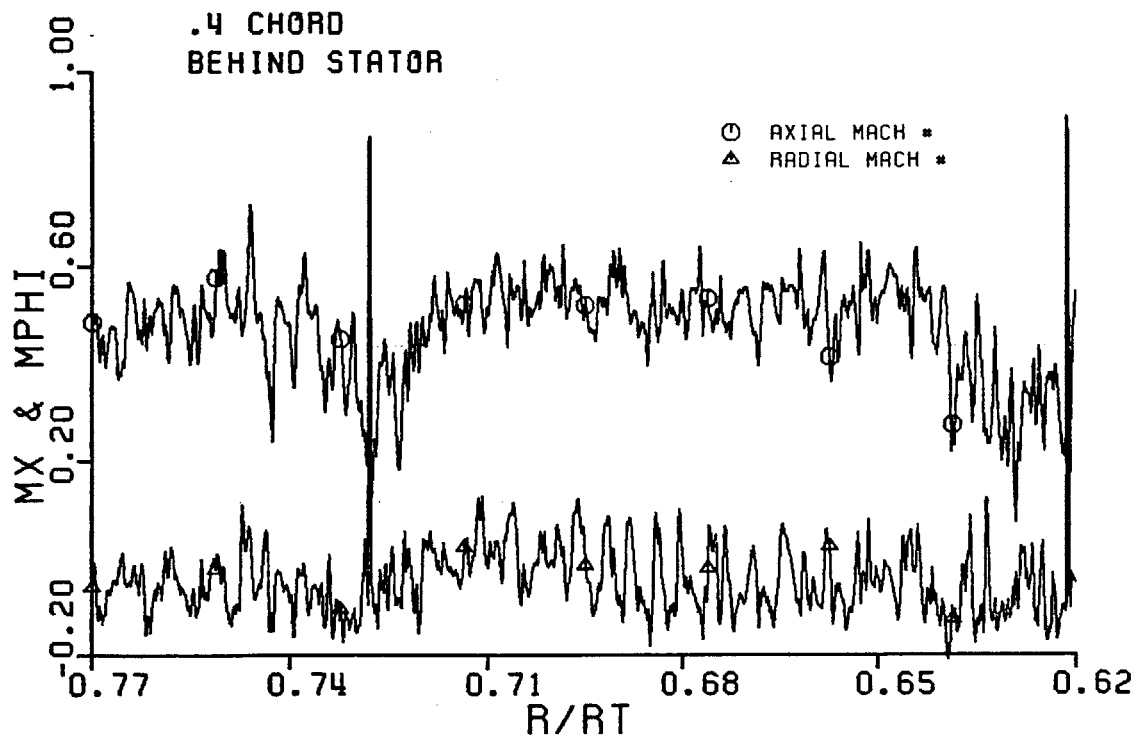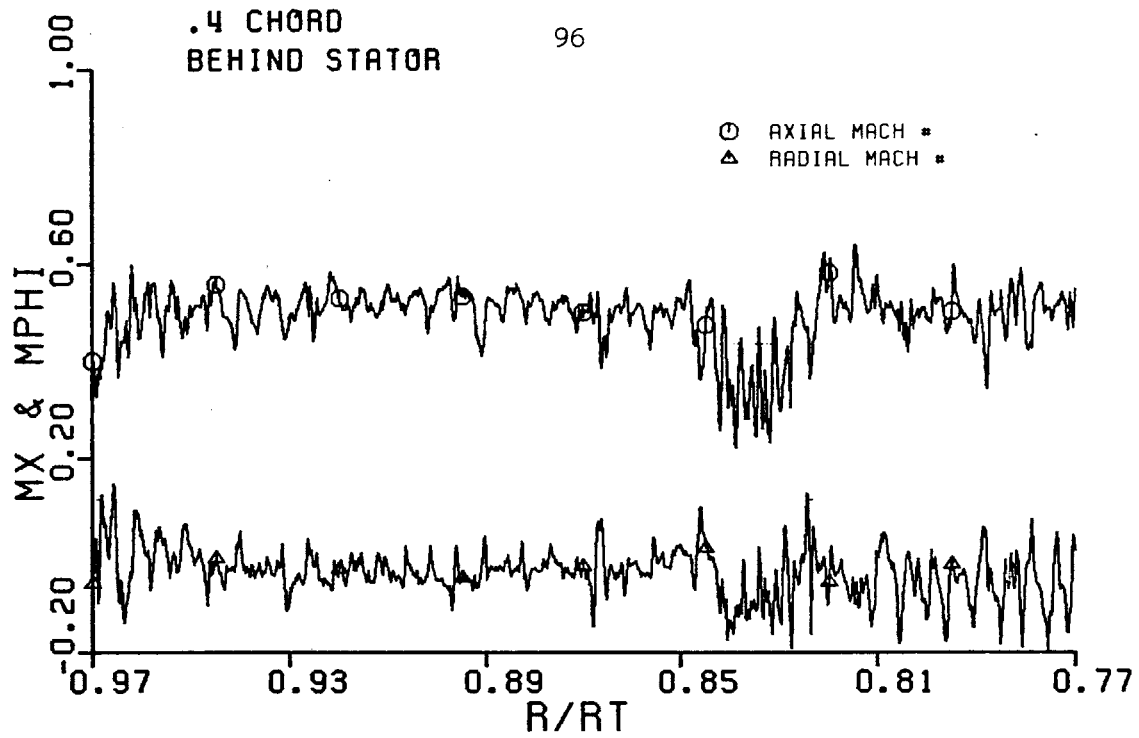
FIGURE 3.7.E   AXIAL AND RADIAL MACH NUMBER BEHIND STATOR AT PORT 4
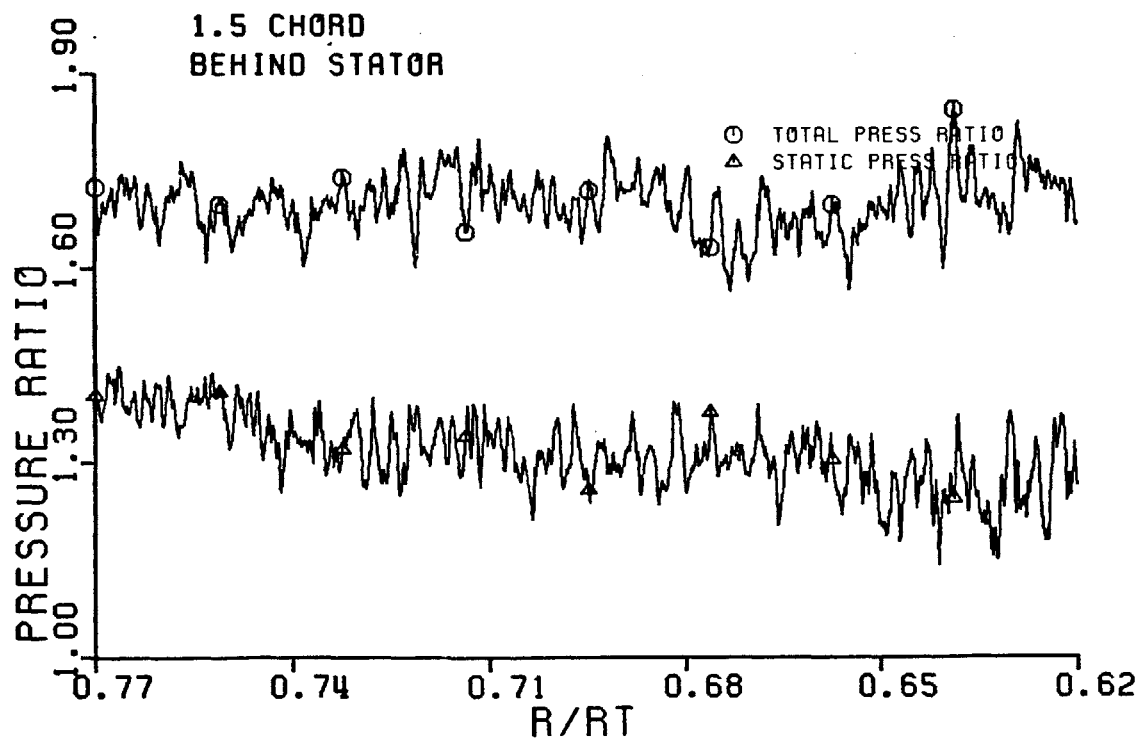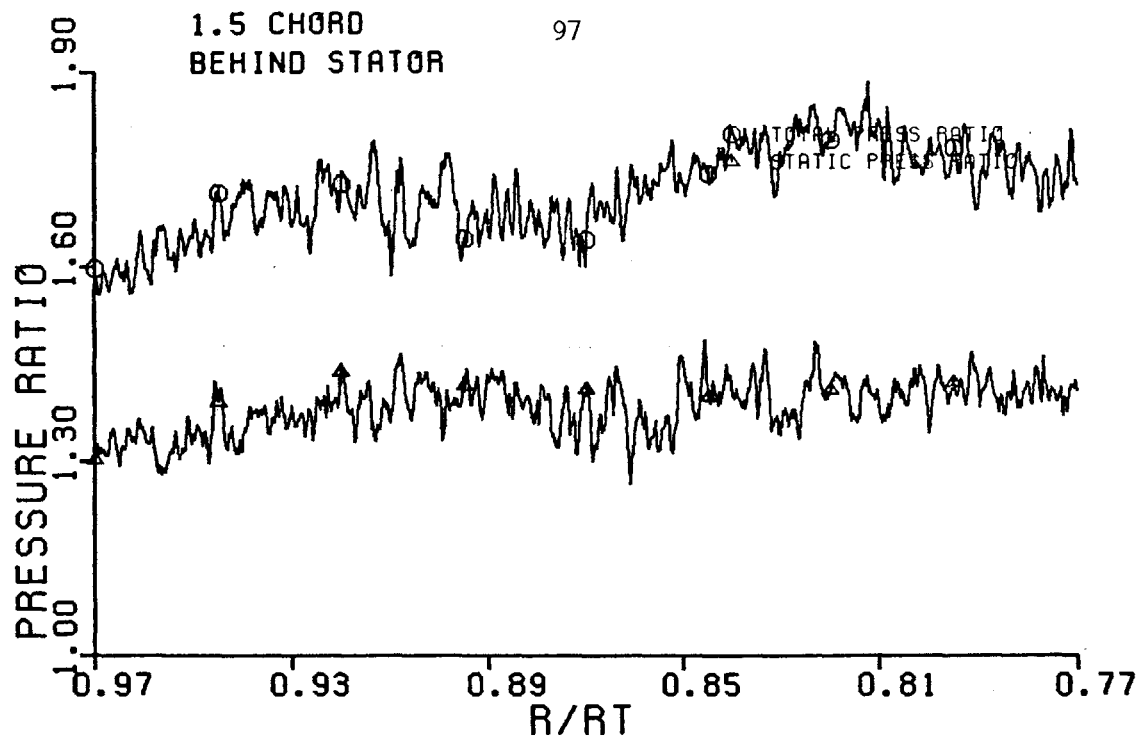
FIGURE 3.8.A   TOTAL AND STATIC PRESSURE RATIO BEHIND STATOR AT PORT 7
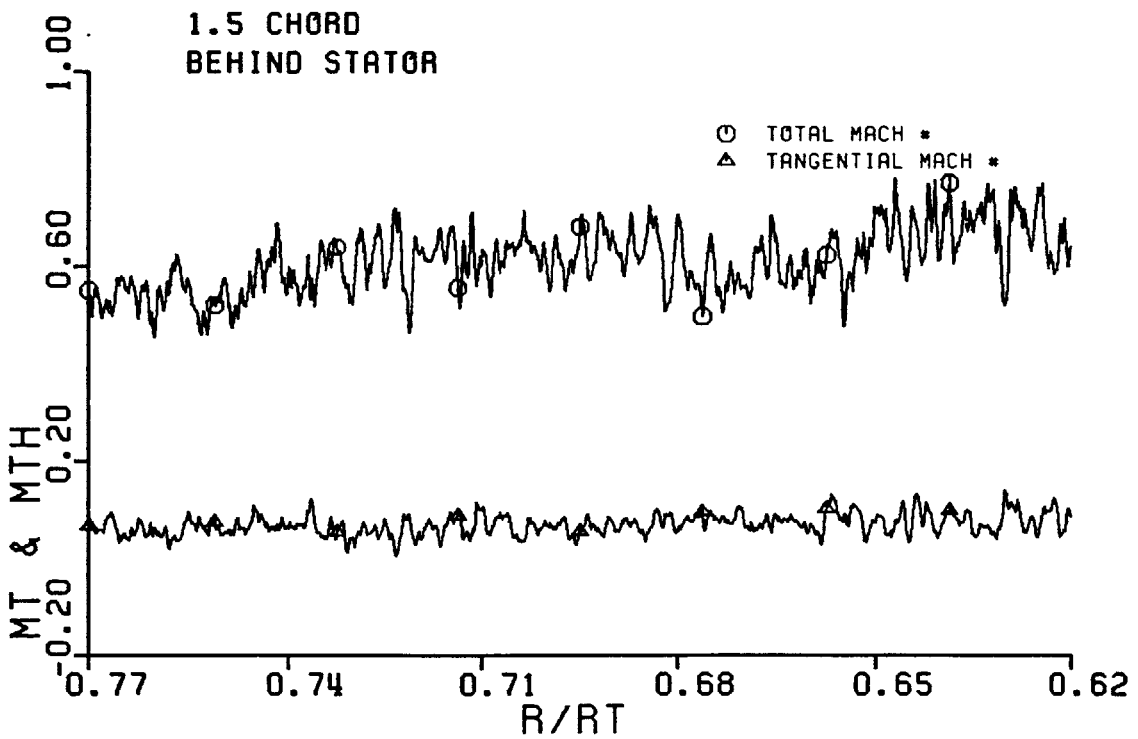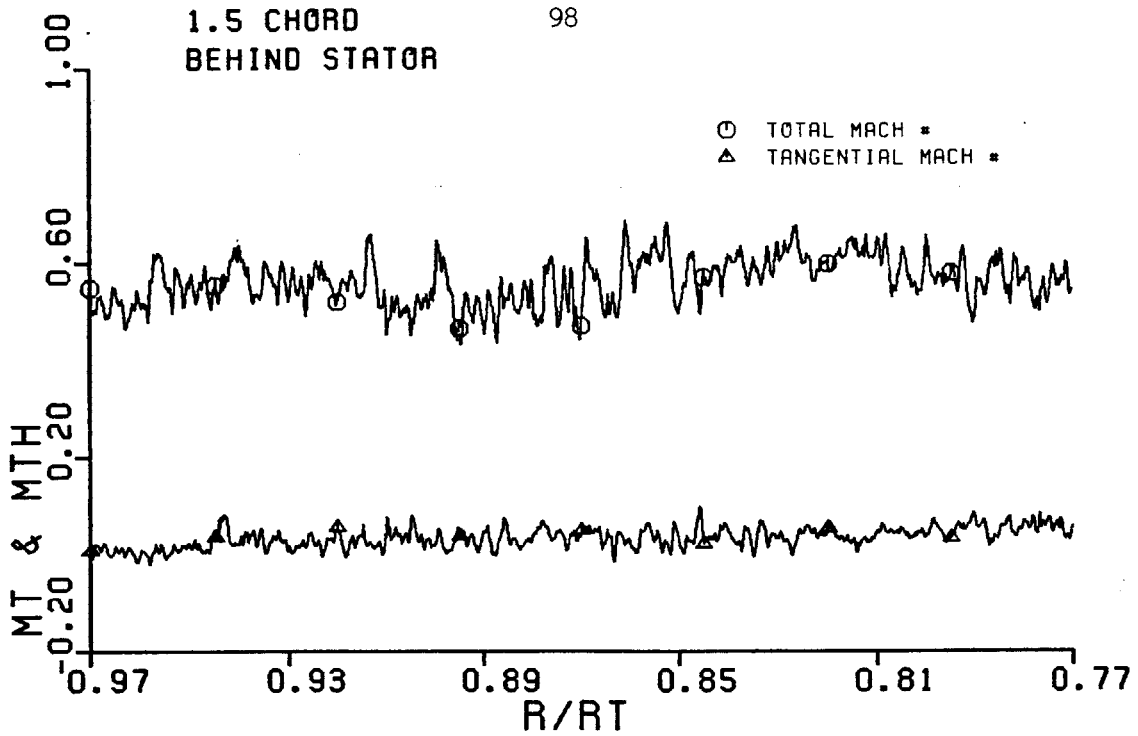
FIGURE 3.8.B   TOTAL AND TANGENTIAL MACH NUMBER BEHIND STATOR AT PORT 7
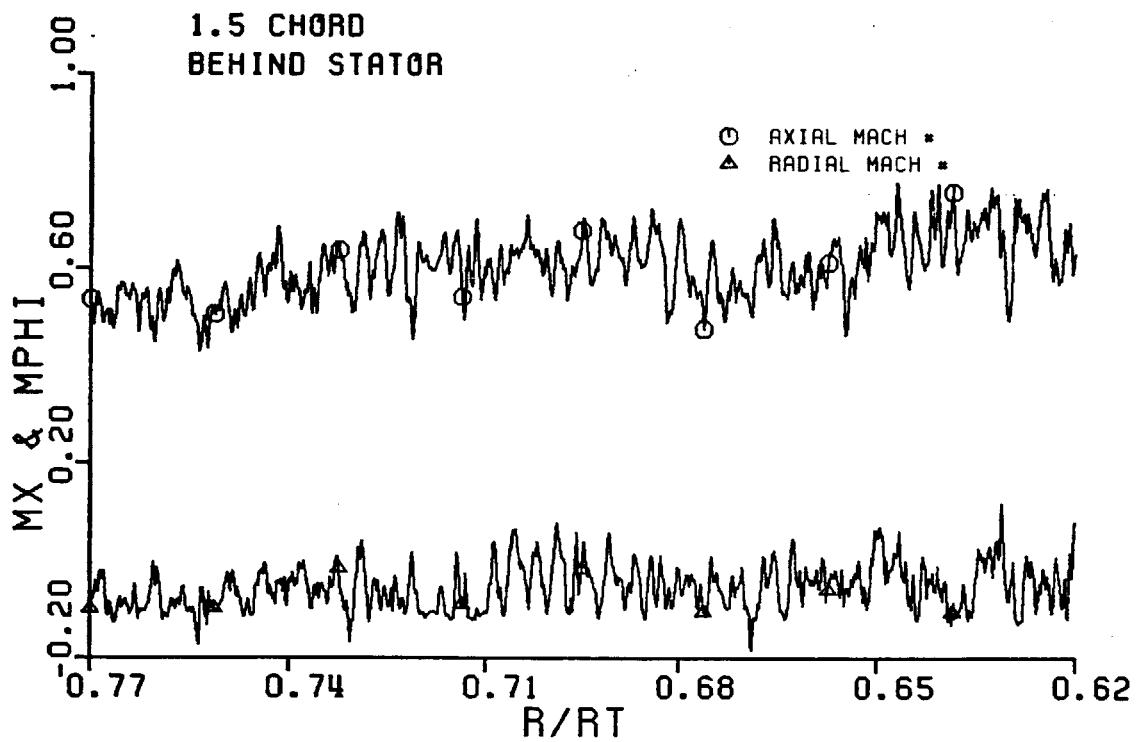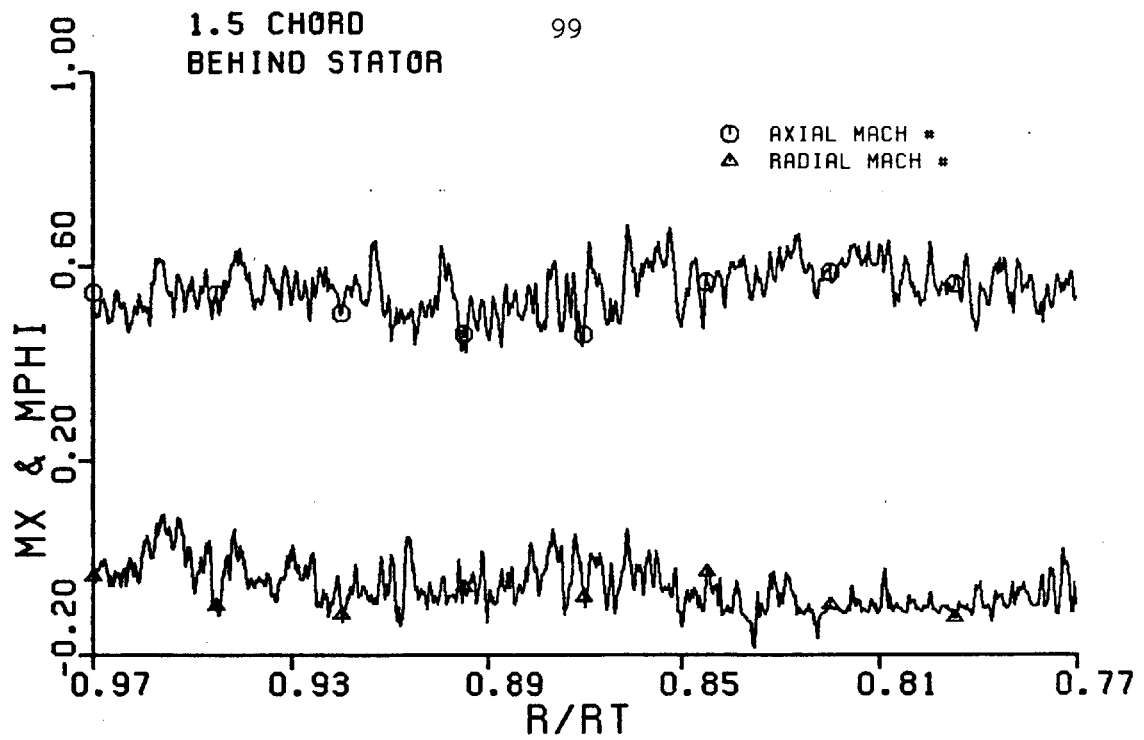
FIGURE 3.8.C   AXIAL AND RADIAL MACH NUMBER BEHIND STATOR AT PORT 7
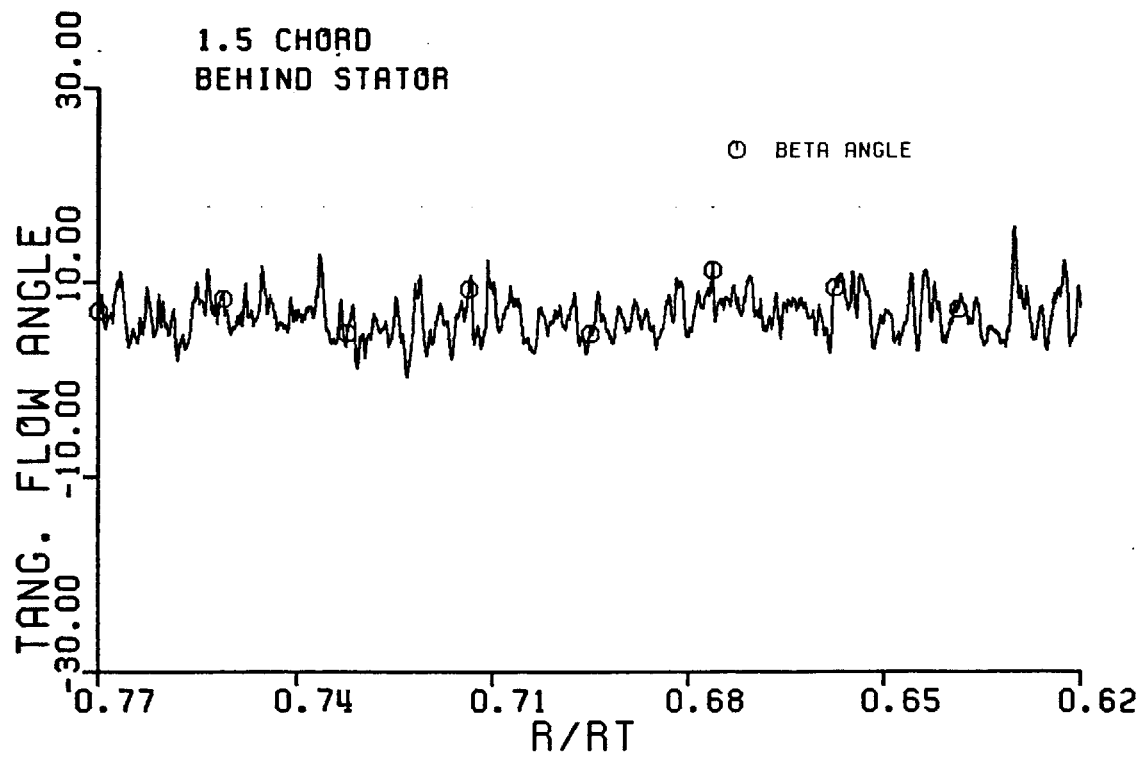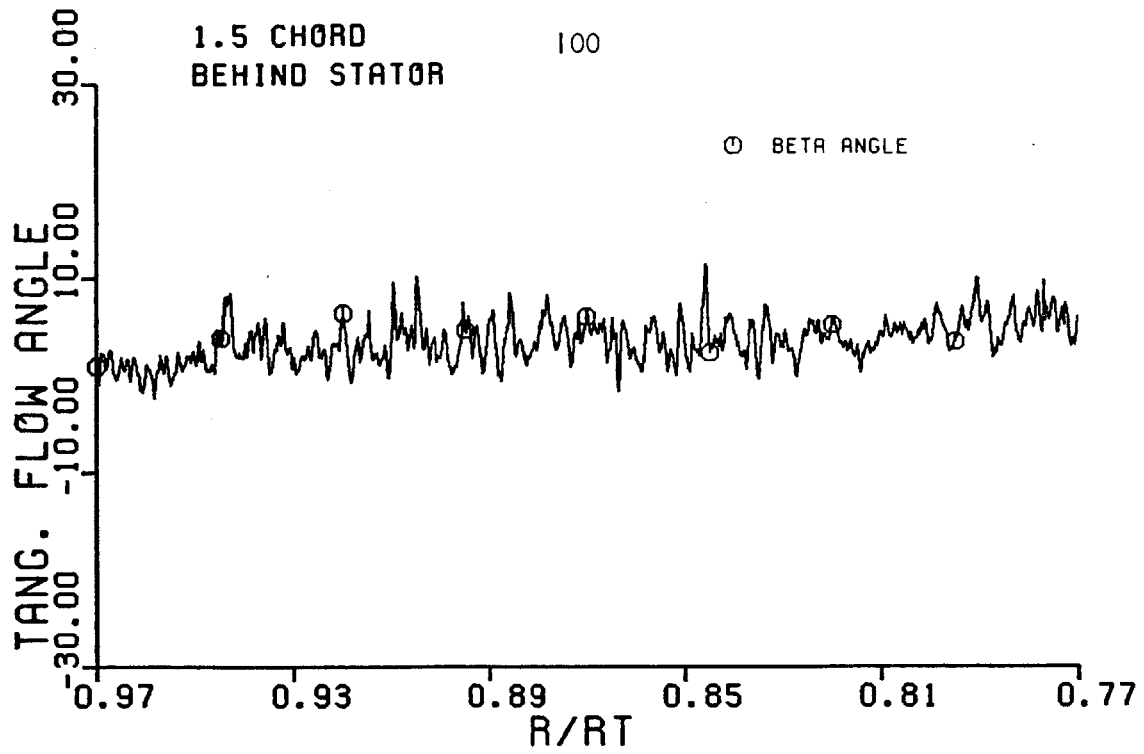
FIGURE 3.8.D   TANGENTIAL FLOW ANGLE BEHIND STATOR AT PORT 7

1.5 CHORD
BEHIND STATOR

⊙ PHI ANGLE

RADIAL ANGLE

30.00   10.00   -10.00   -30.00

0.97   0.93   0.89   0.85   0.81   0.77

R/RT

1.5 CHORD
BEHIND STATOR

⊙ PHI ANGLE

RADIAL ANGLE

30.00   10.00   -10.00   -30.00

0.77   0.74   0.71   0.68   0.65   0.62

R/RT
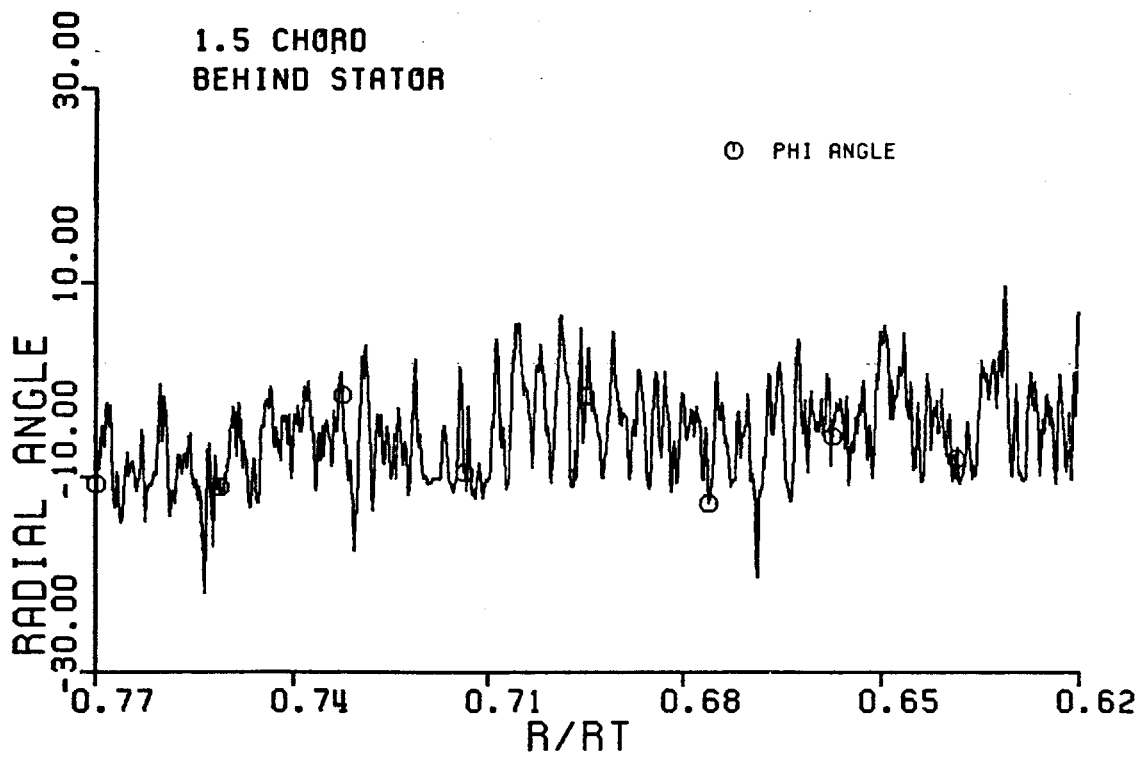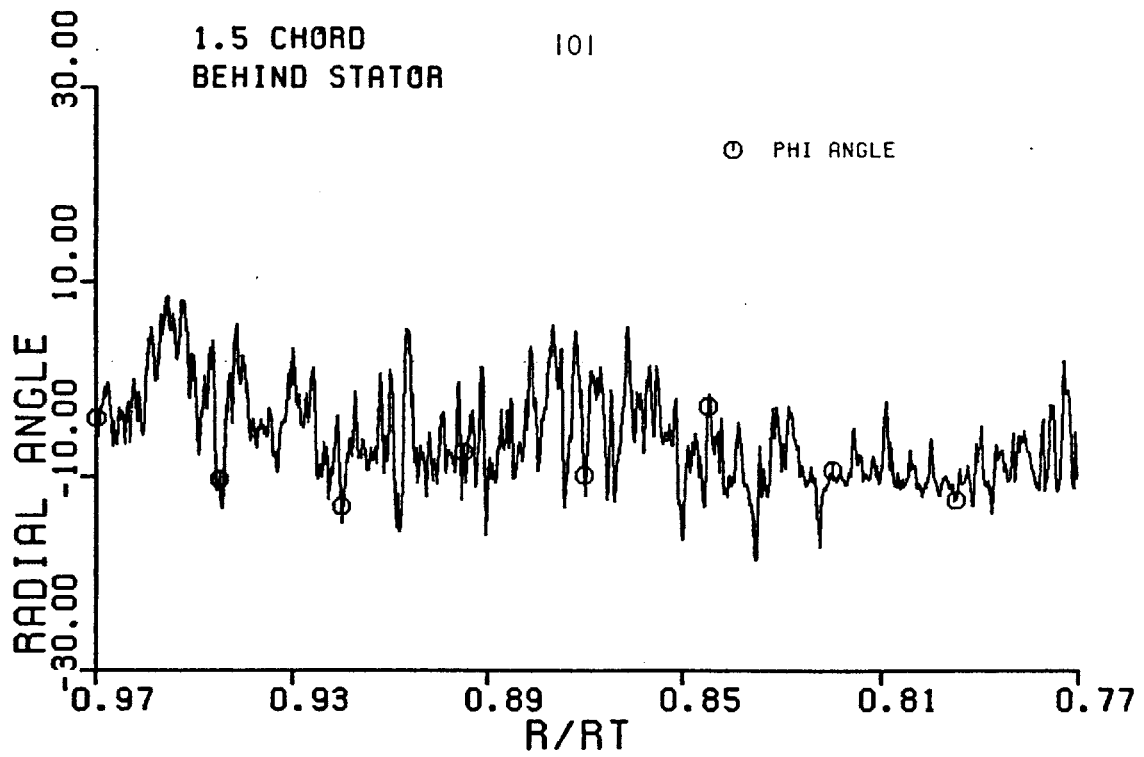
FIGURE 3.8.E   RADIAL FLOW ANGLE BEHIND STATOR AT PORT 7

BEHIND ROTOR

Ⓞ TOTAL PRESS RATIO

.4 CHORD
BEHIND STATOR

Ⓞ TOTAL PRESS RATIO

1.5 CHORD
BEHIND STATOR

Ⓞ TOTAL PRESS RATIO

R/RT

TOTAL PRESSURE RATIO
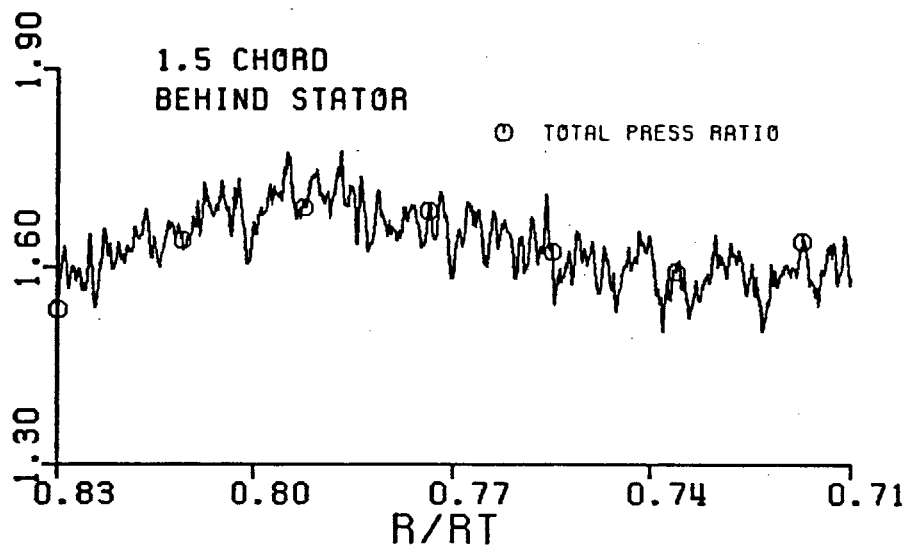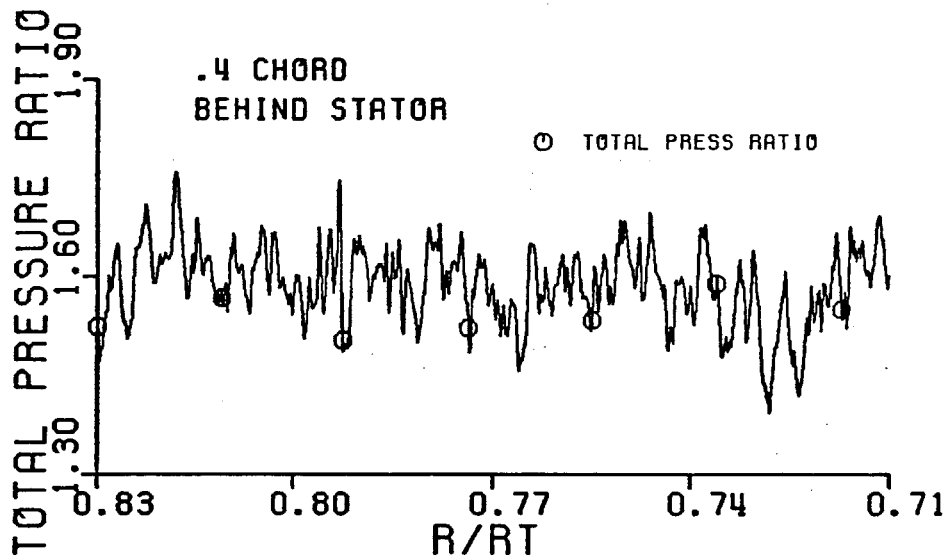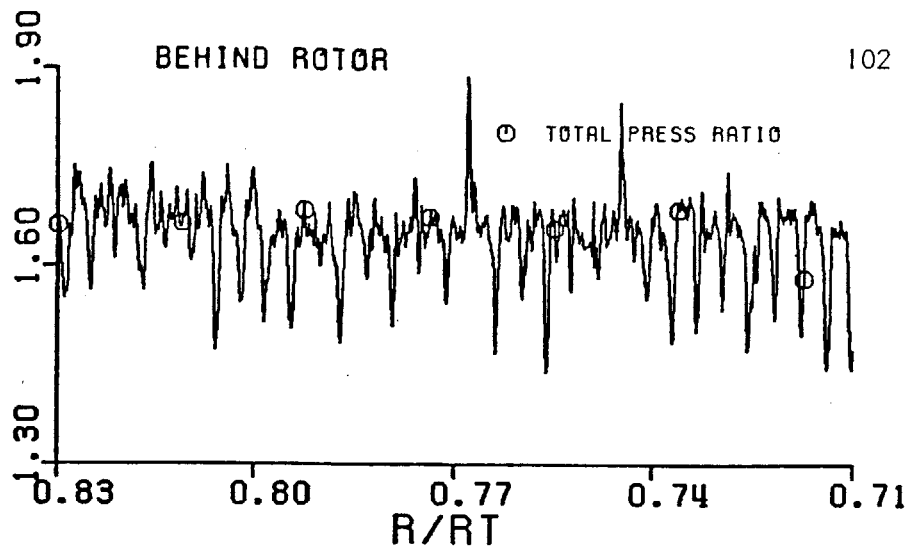
FIGURE 3.9.A   COMPARISON BETWEEN TOTAL PRESSURE RATIO AS MEASURED AT
DIFFERENT AXIAL LOCATIONS IN THE STAGE
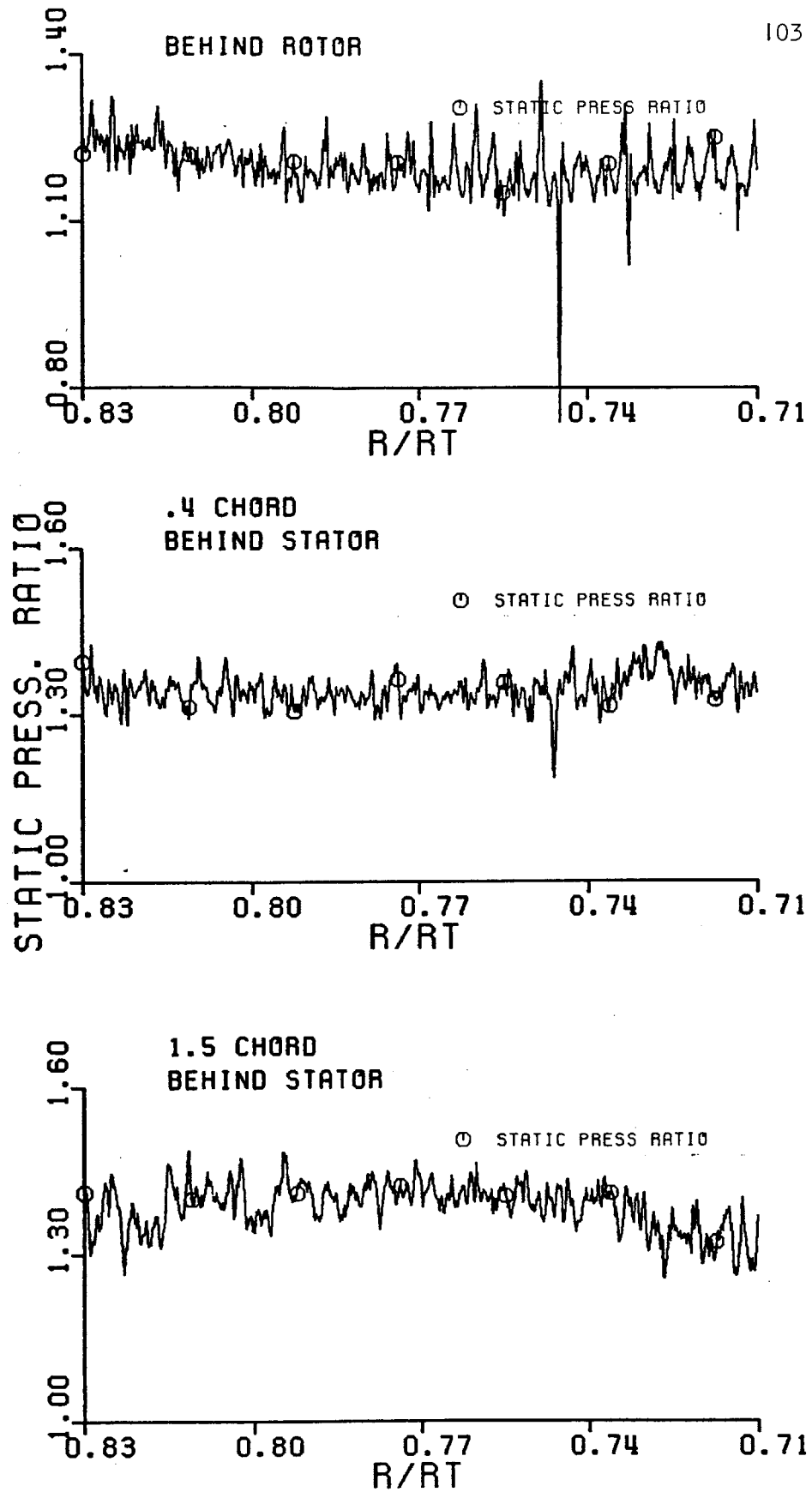
FIGURE 3.9.B   COMPARISON BETWEEN STATIC PRESSURE RATIO AS MEASURED AT
DIFFERENT AXIAL LOCATIONS IN THE STAGE
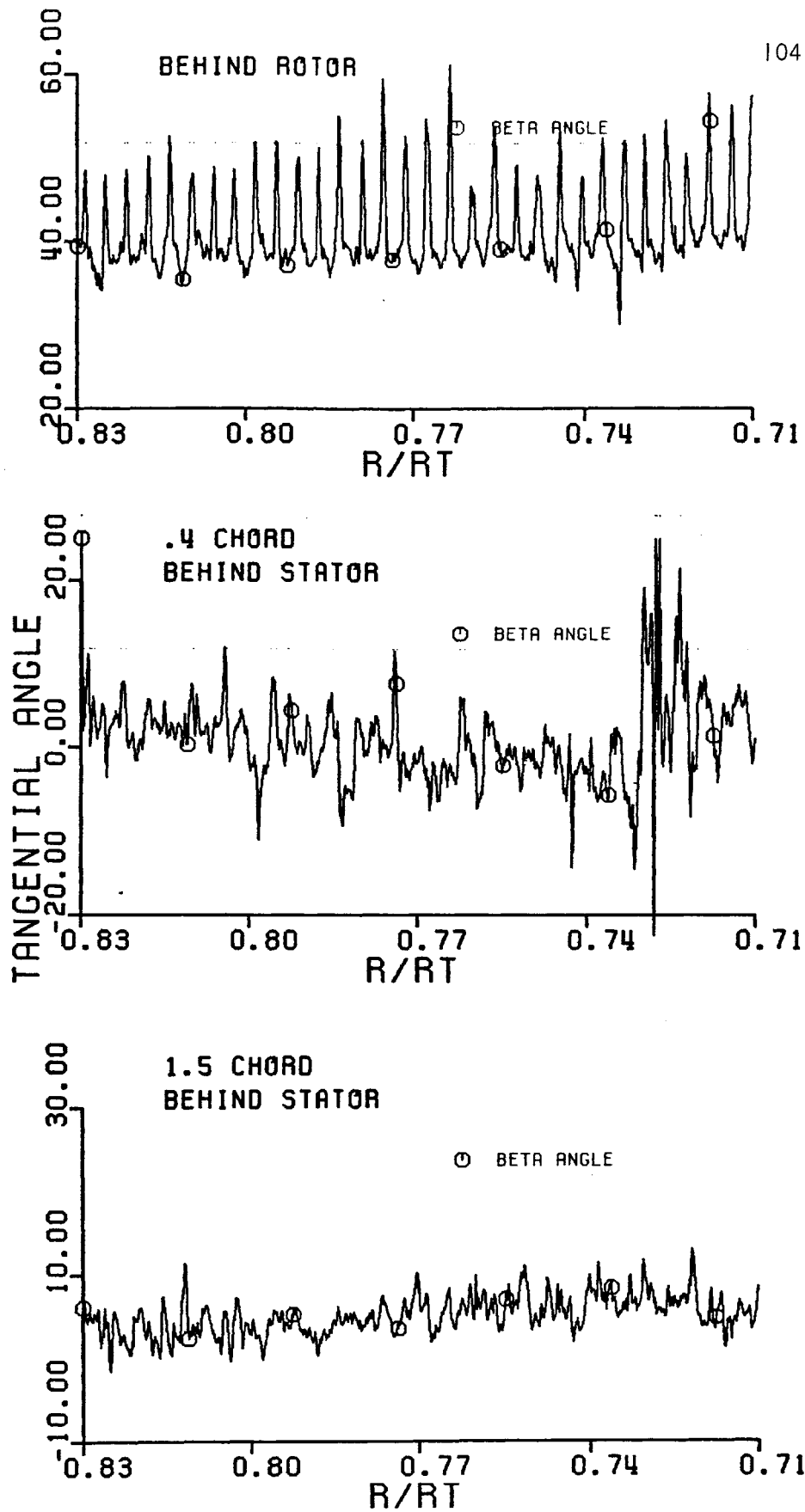
FIGURE 3.9.C COMPARISON BETWEEN TANGENTIAL FLOW ANGLE AS MEASURED AT
DIFFERENT AXIAL LOCATIONS IN THE STAGE
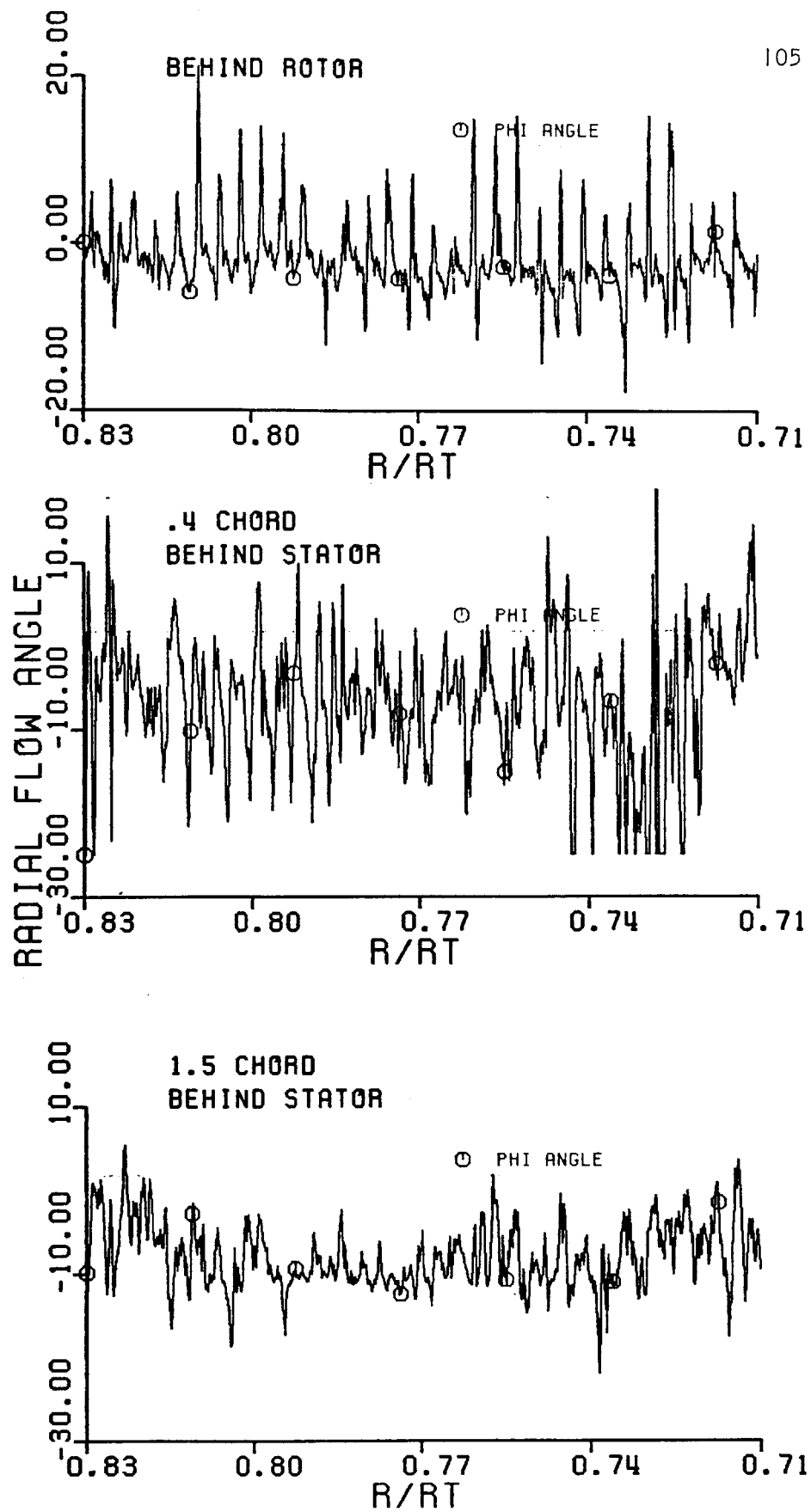
FIGURE 3.9.D   COMPARISON BETWEEN RADIAL FLOW ANGLE AS MEASURED AT
DIFFERENT AXIAL LOCATIONS IN THE STAGE

BEHIND ROTOR

⊙ TOTAL MACH #

0.83 0.80 0.77 0.74 0.71
R/RT

.4 CHORD
BEHIND STATOR

⊙ TOTAL MACH #

0.83 0.80 0.77 0.74 0.71
R/RT

TOTAL MACH NUMBER

1.5 CHORD
BEHIND STATOR

⊙ TOTAL MACH #

0.83 0.80 0.77 0.74 0.71
R/RT
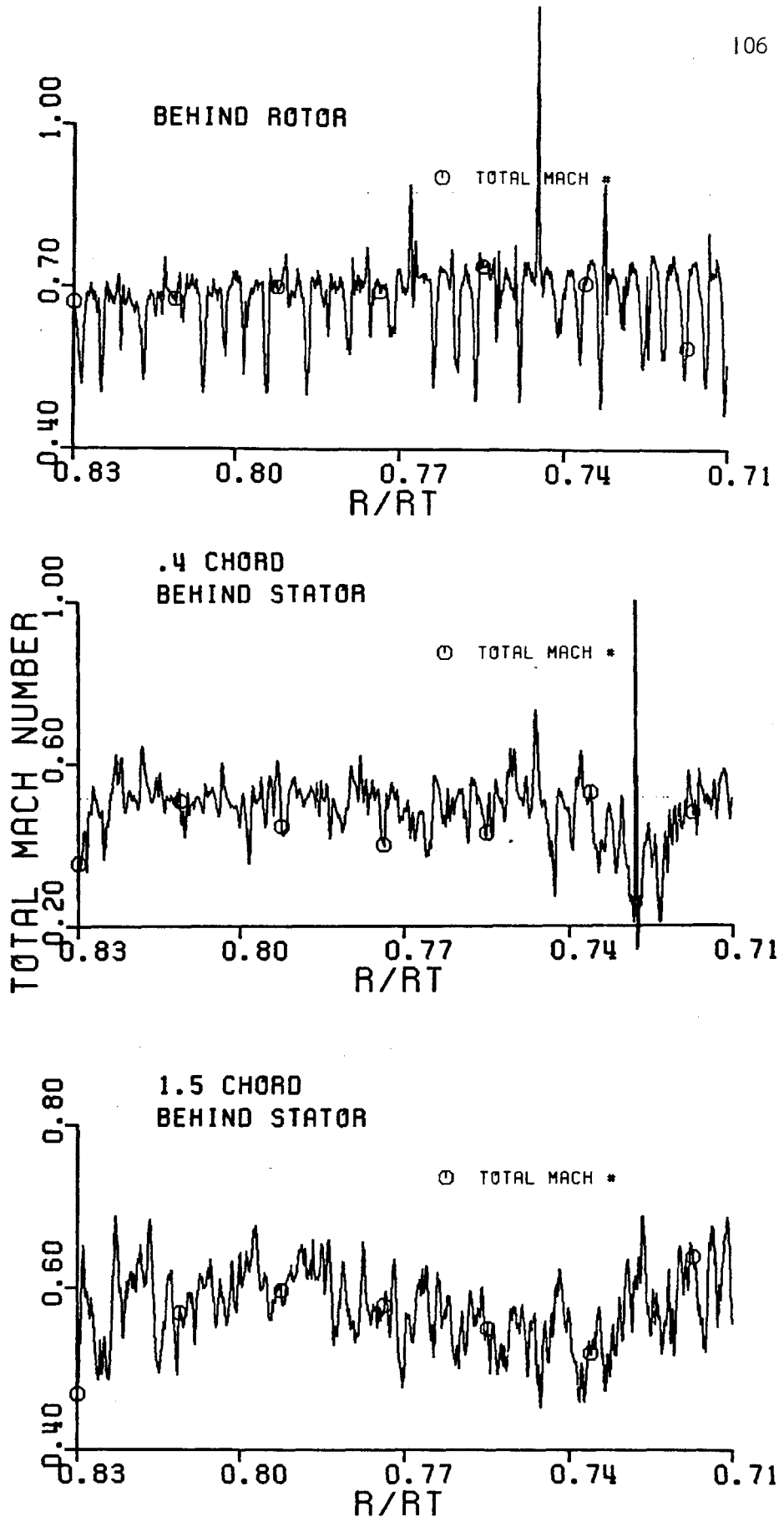
FIGURE 3.9.E   COMPARISON BETWEEN TOTAL MACH NUMBER AS MEASURED AT
DIFFERENT AXIAL LOCATIONS IN THE STAGE
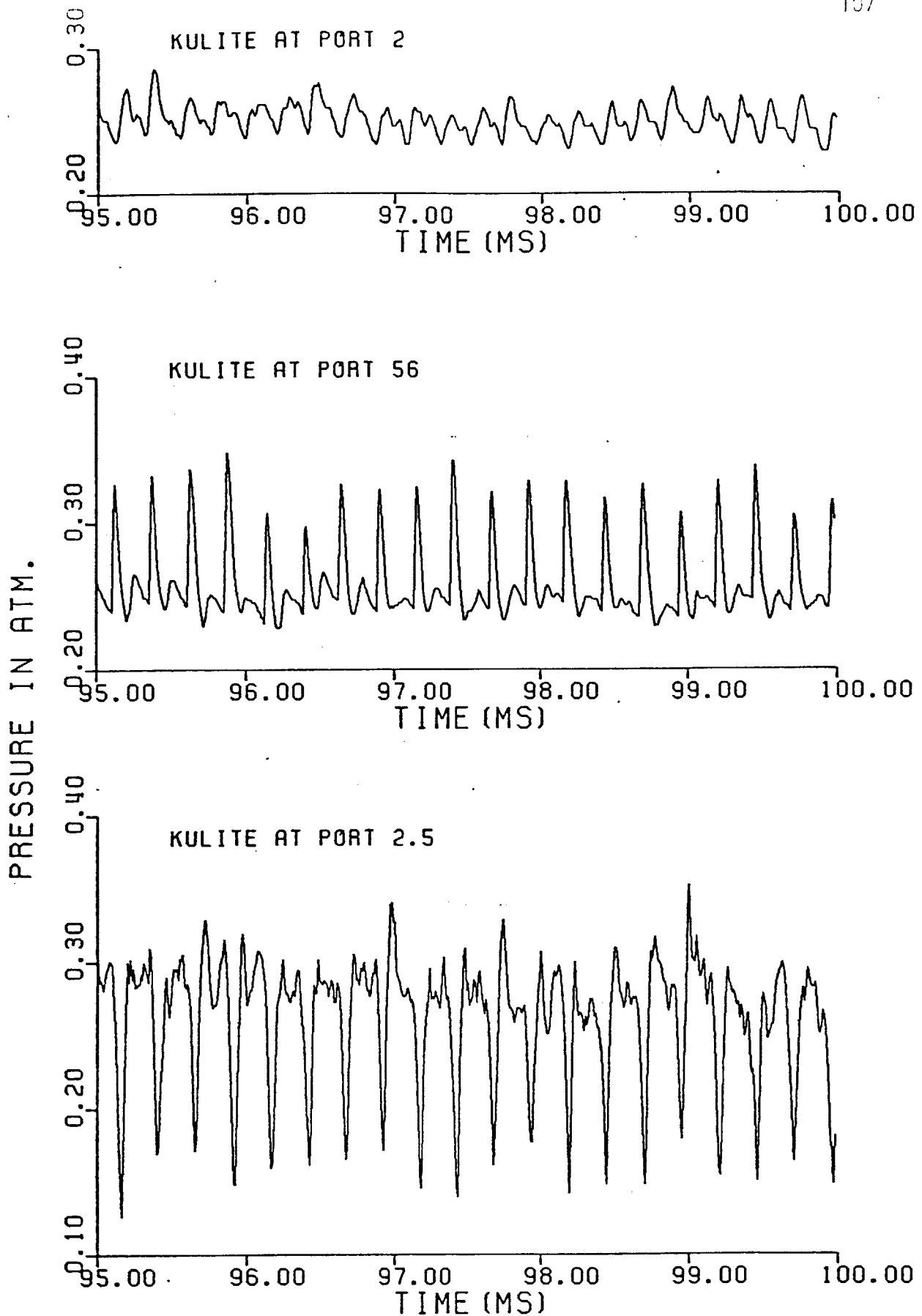
FIGURE 3.10 COMPARISON OF WALL STATIC PRESSURE MEASUREMENTS AT PORT 2, PORT 56, AND PORT 2.5
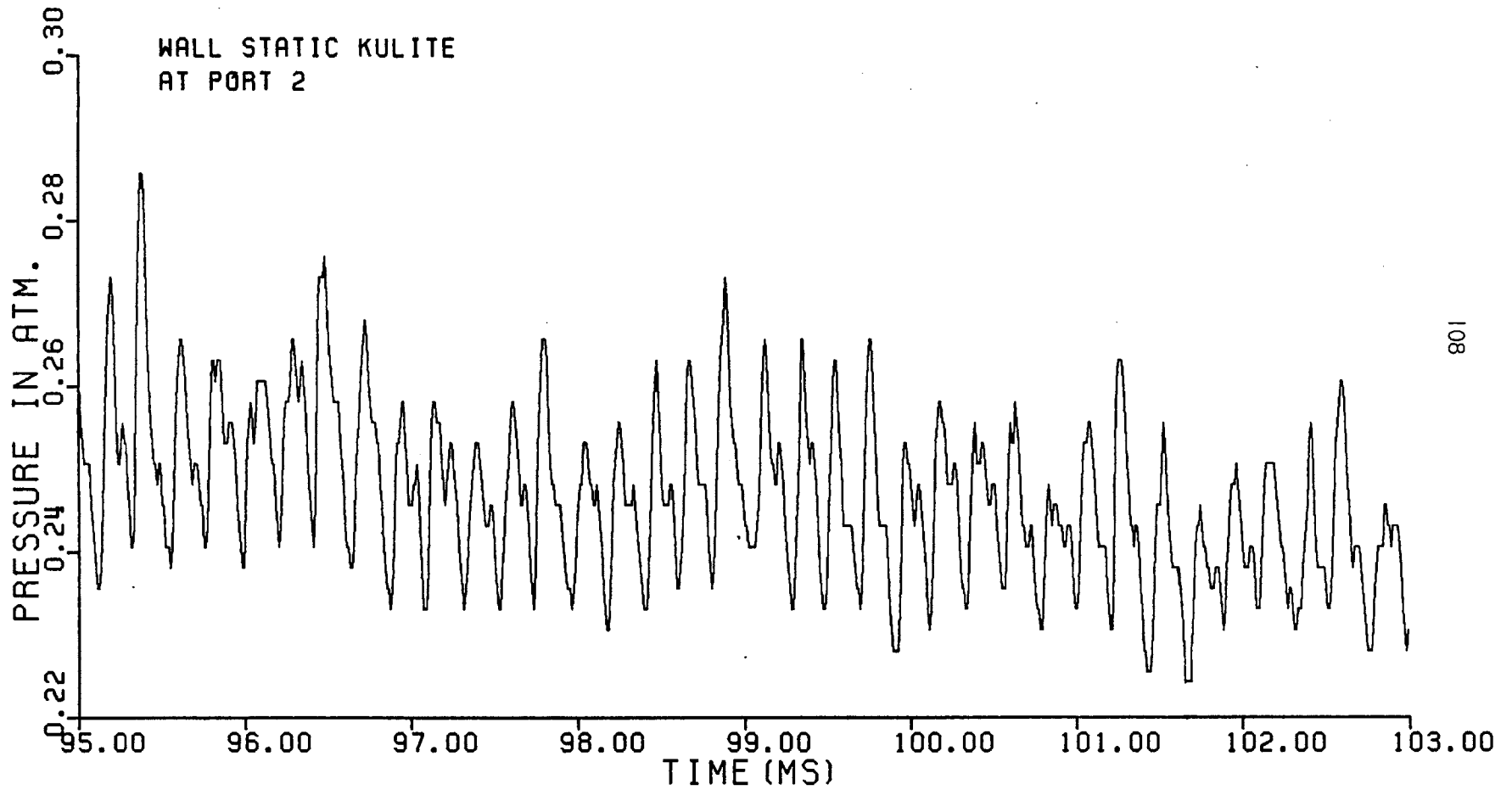
FIGURE 3.11.A   WALL STATIC MEASUREMENTS AT PORT 2

POWER SPECTRUM DENSITY OF KULITE AT PORT 2

TIME = 96.44 TO 101.56 M.S.
FREQUENCY RANGE 1.00 TO 20.00 KHZ.
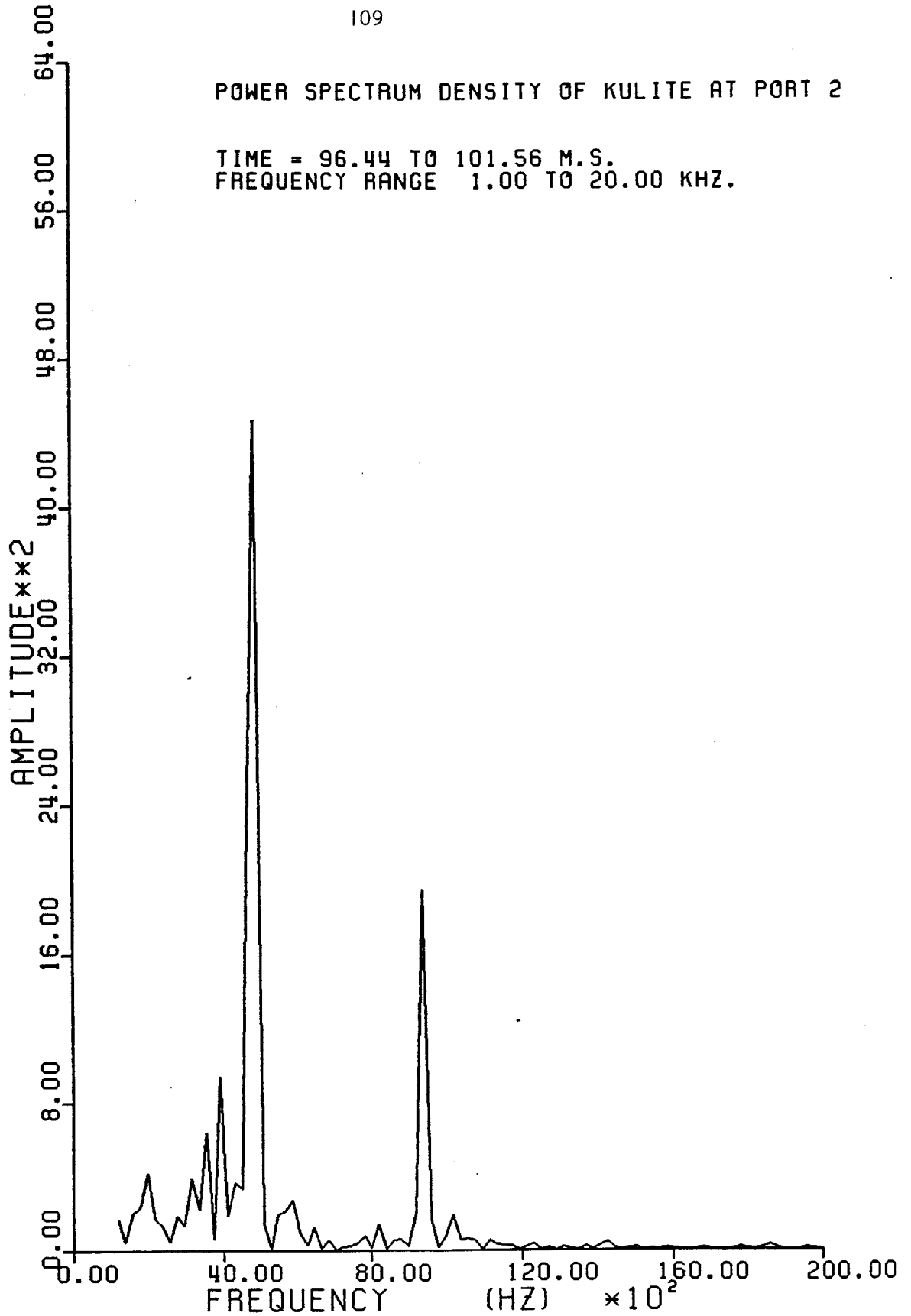
FIGURE 3.11.B FREQUENCY SPECTRUM OF WALL STATIC PRESSURE MEASUREMENTS AT
              PORT 2
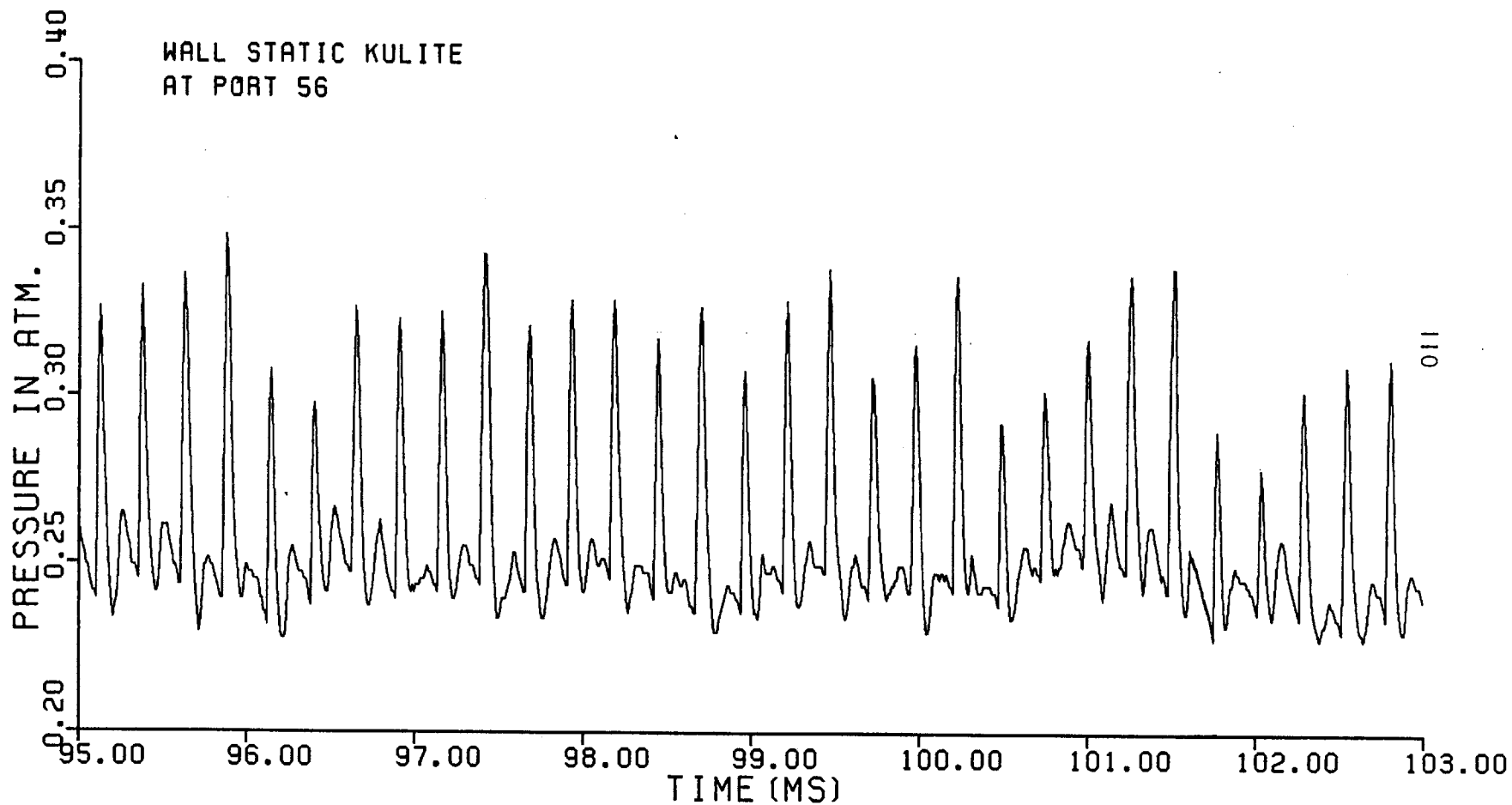
FIGURE 3.12.A WALL STATIC MEASUREMENTS AT PORT 56
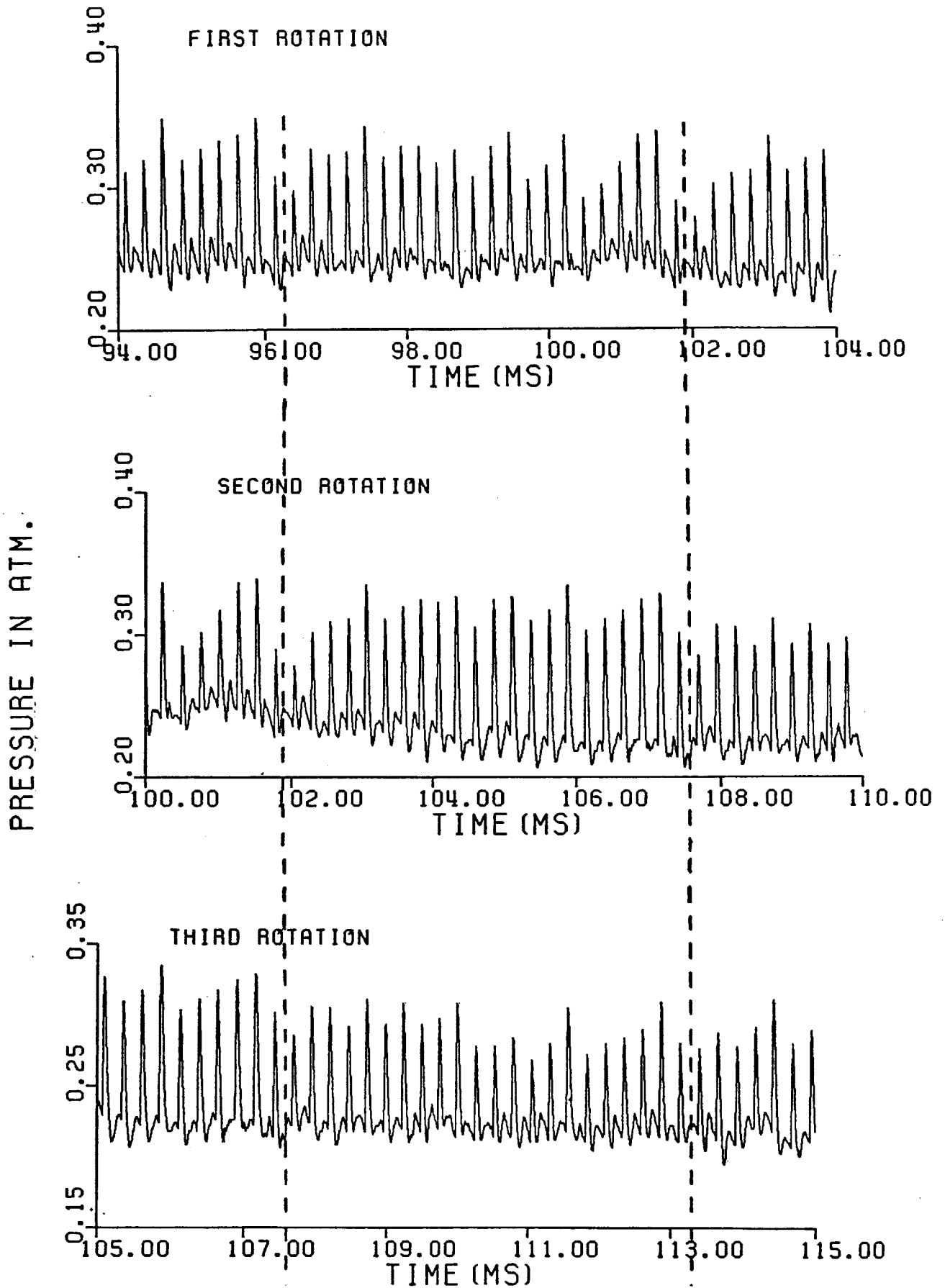
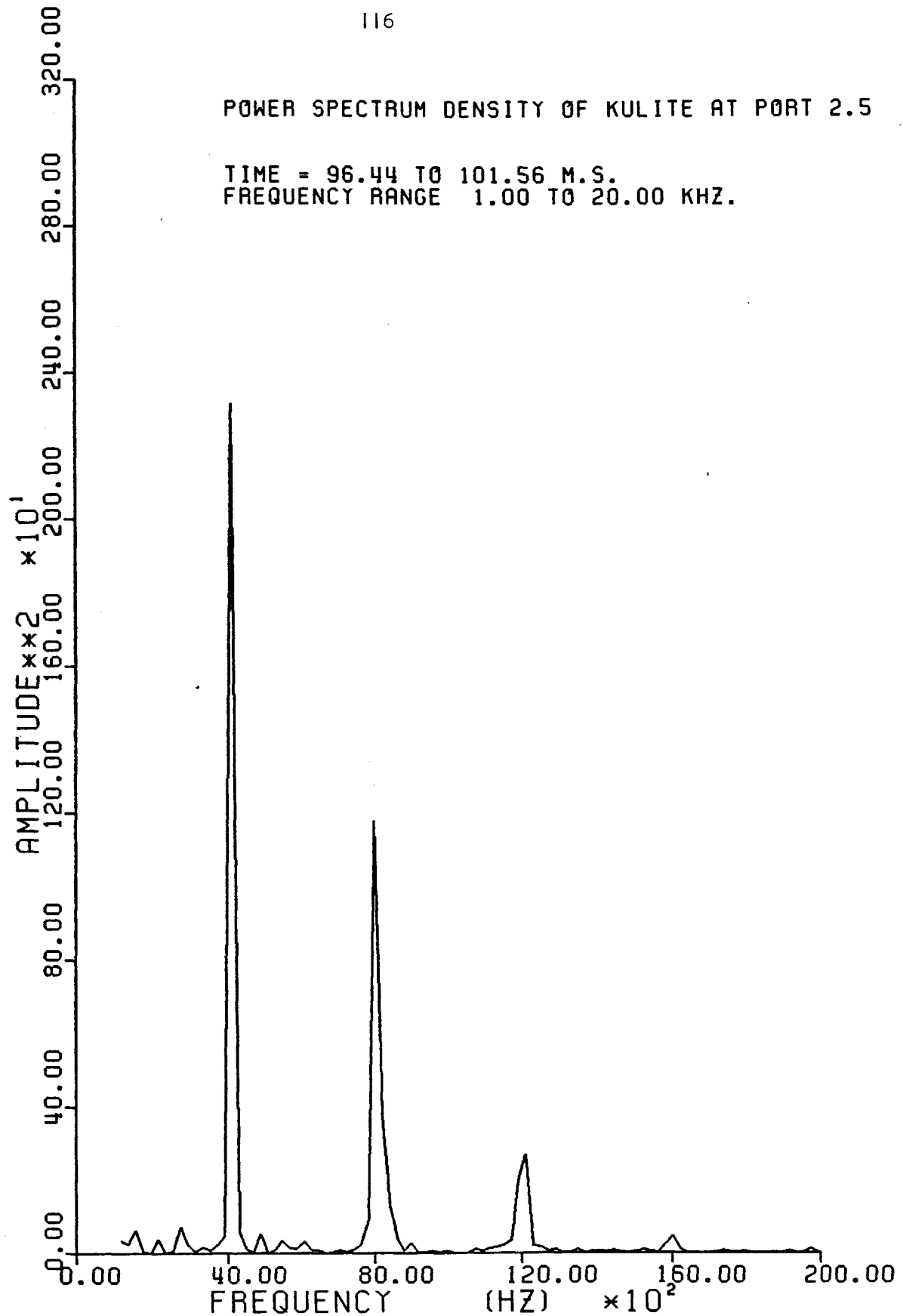FIGURE 3.12.B   WALL STATIC MEASUREMENTS AT PORT 56 FOR THREE SUCCESSIVE
ROTATIONS OF THE ROTOR
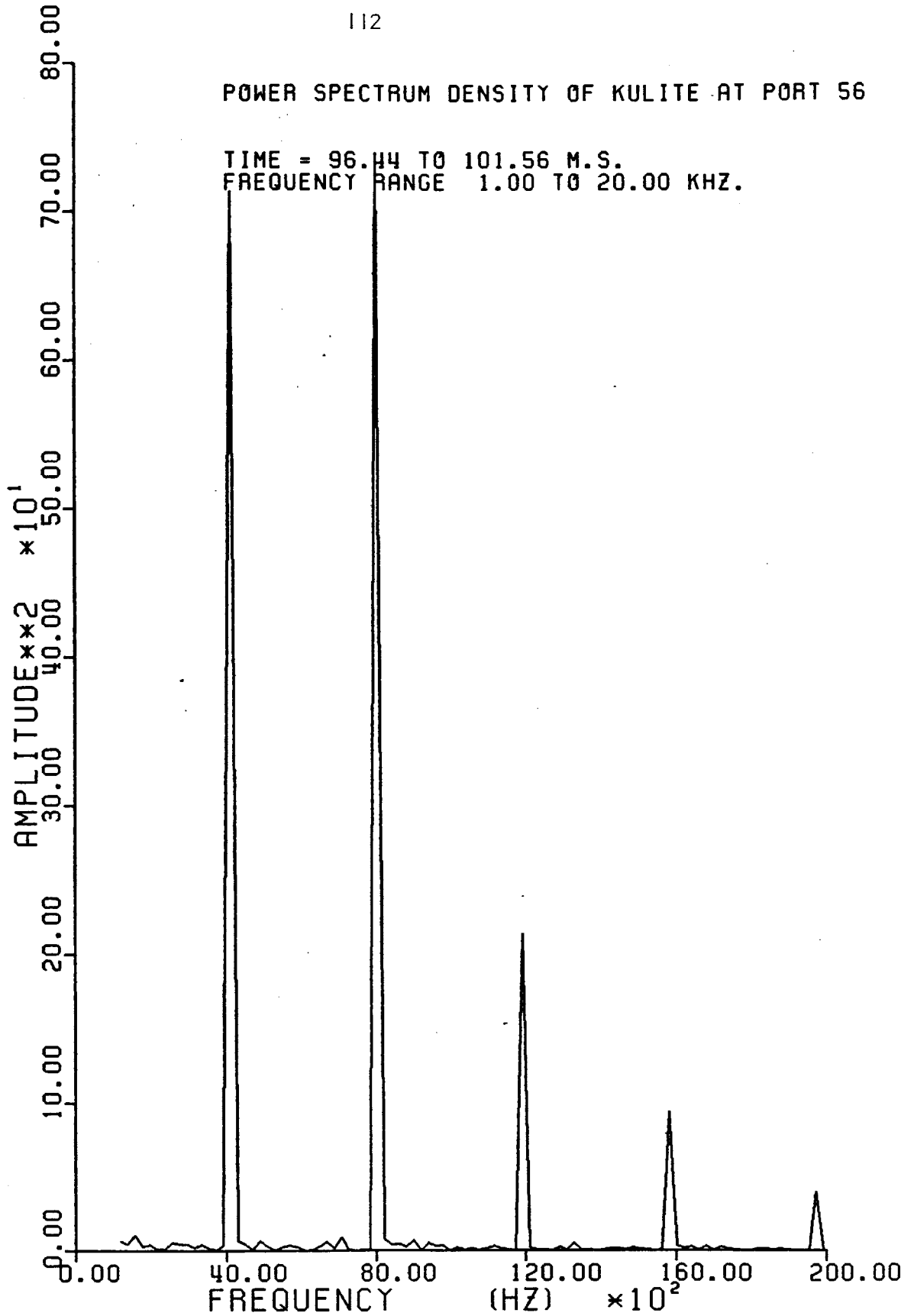
FIGURE 3.12.C   FREQUENCY SPECTRUM OF WALL STATIC PRESSURE MEASUREMENTS
AT PORT 56
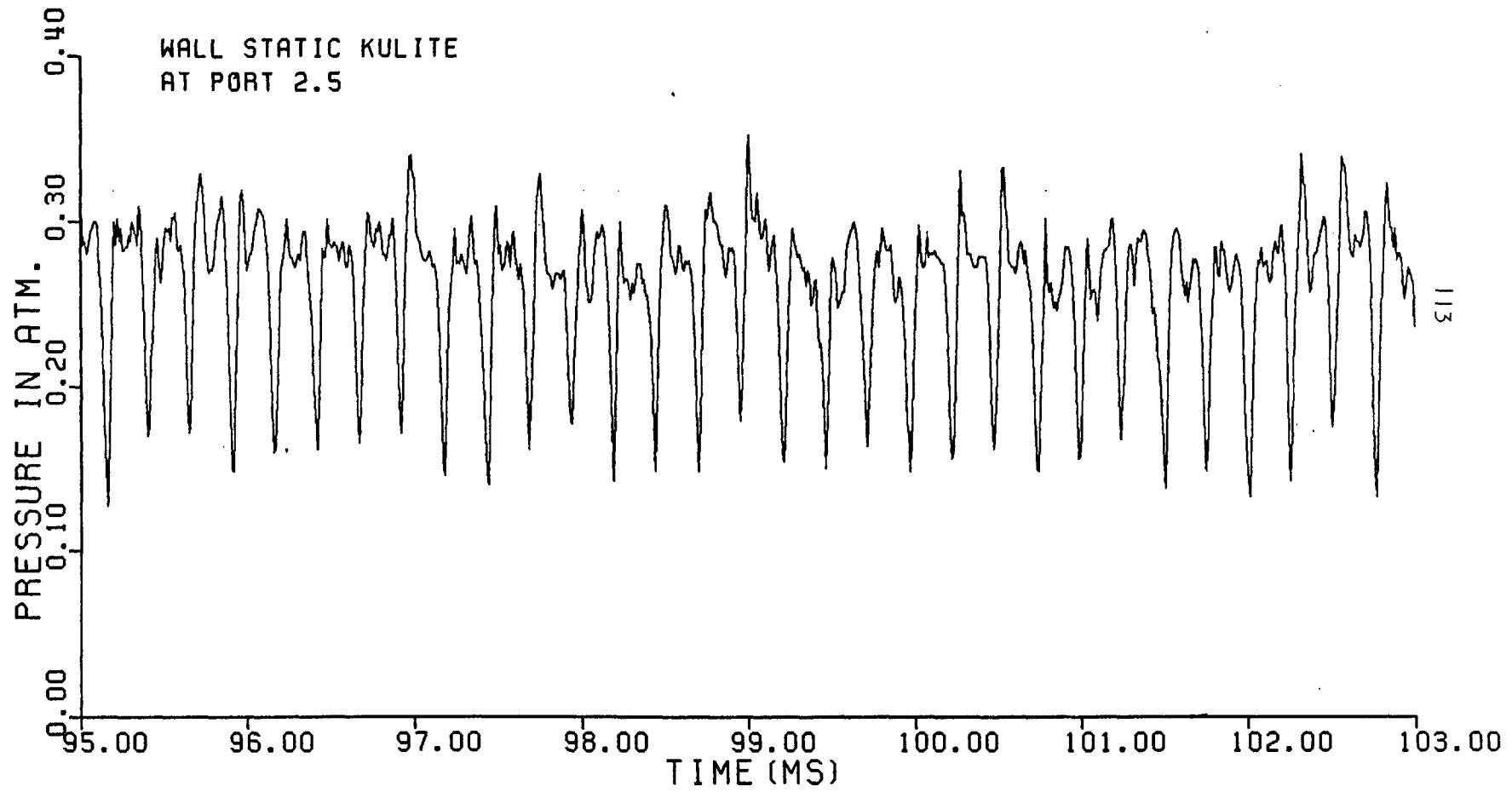
FIGURE 3.13.A   WALL STATIC MEASUREMENTS AT PORT 2.5
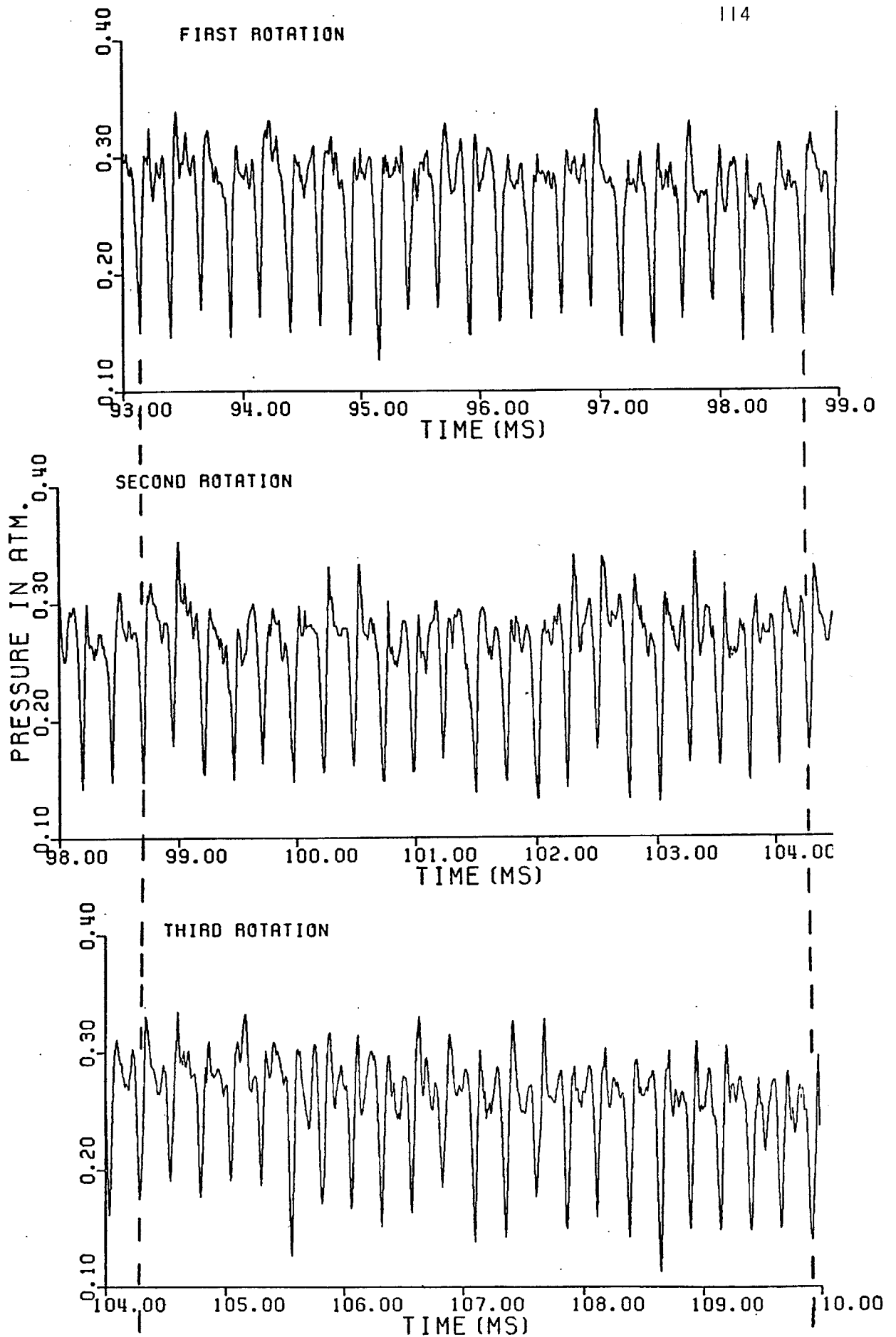
FIGURE 3.13.B WALL STATIC MEASUREMENTS AT PORT 2.5 FOR THREE SUCCESSIVE ROTATIONS OF THE ROTOR
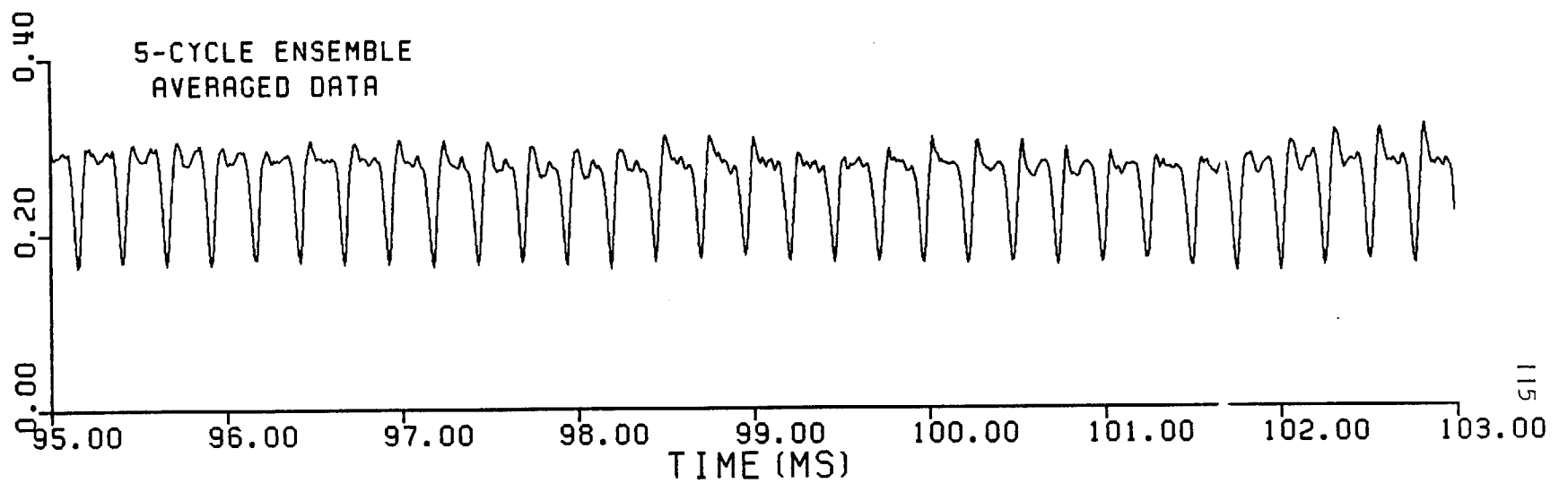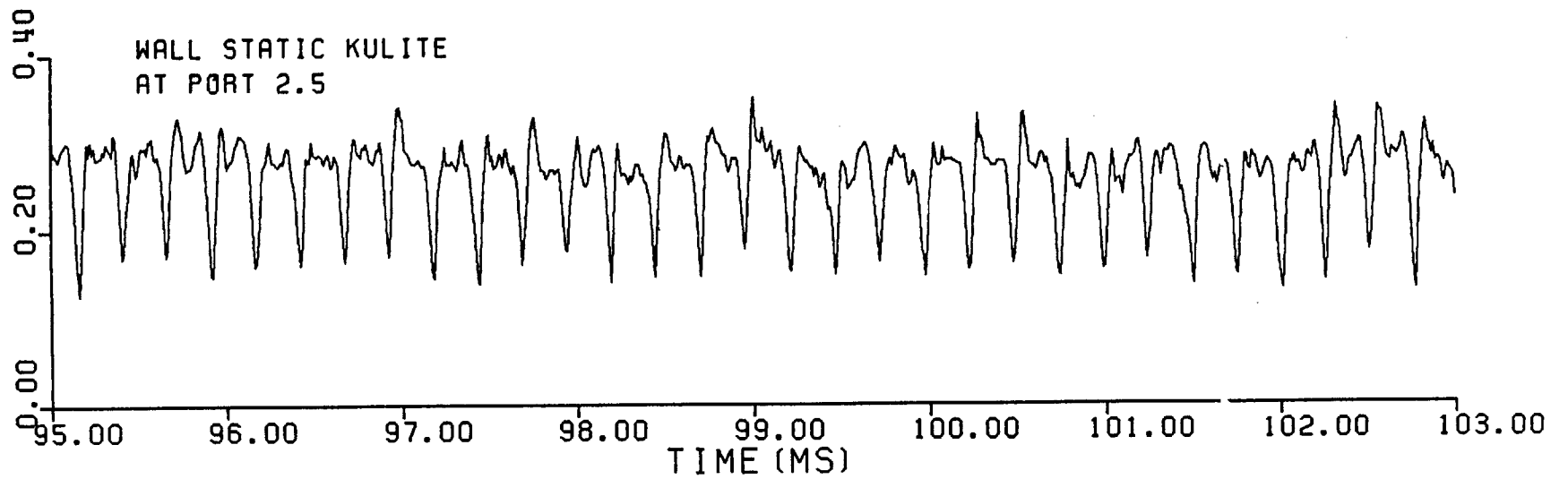
FIGURE 3.13.C COMPARISON BETWEEN ORIGINAL SIGNALS & 5 CYCLES ENSEMBLE AVERAGE OF THE SAME
SIGNALS FROM PORT 2.5

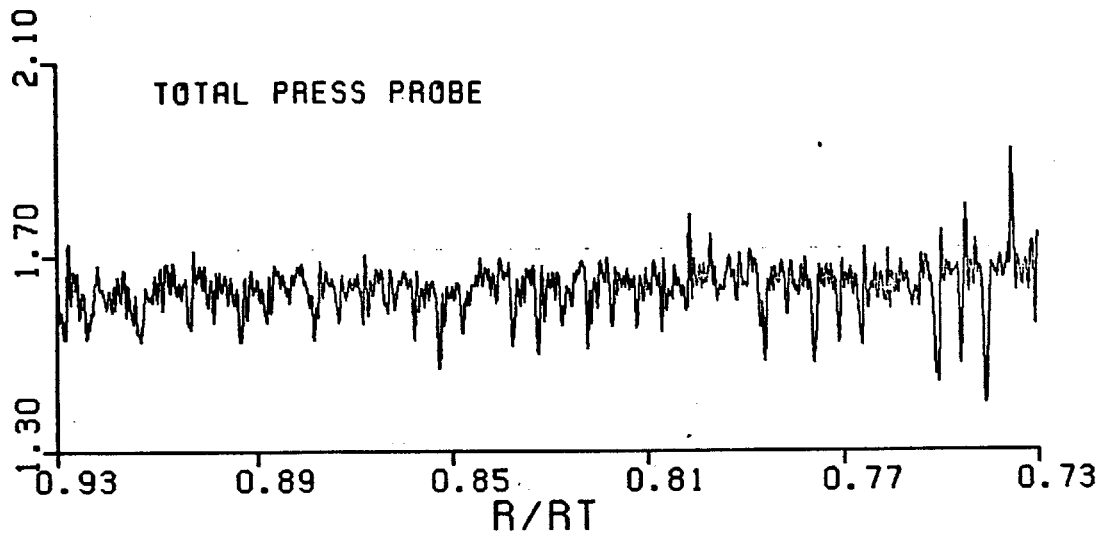FIGURE 3.13.D   FREQUENCY SPECTRUM OF WALL STATIC PRESSURE MEASUREMENTS
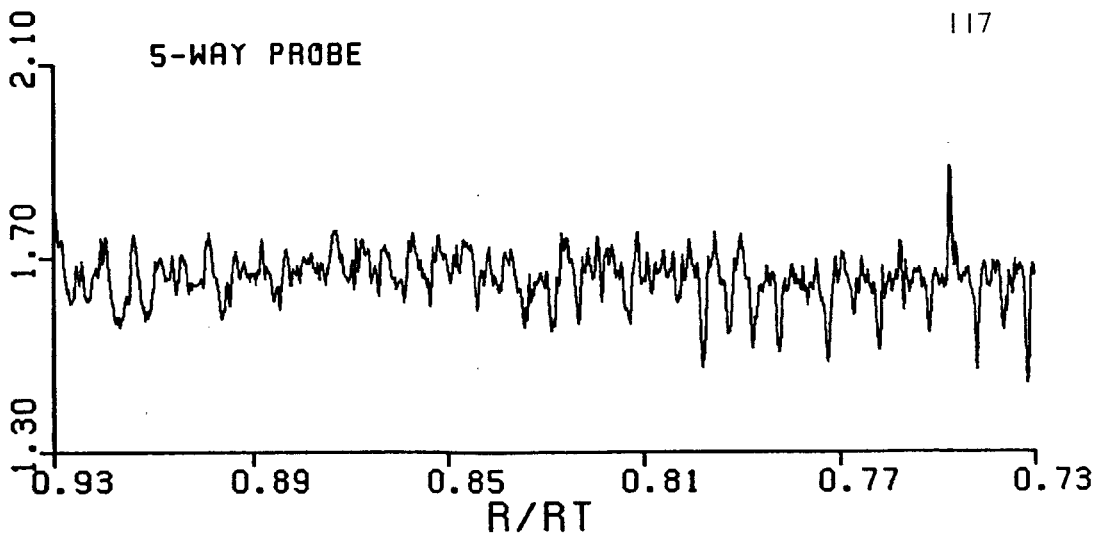AT PORT 2.5
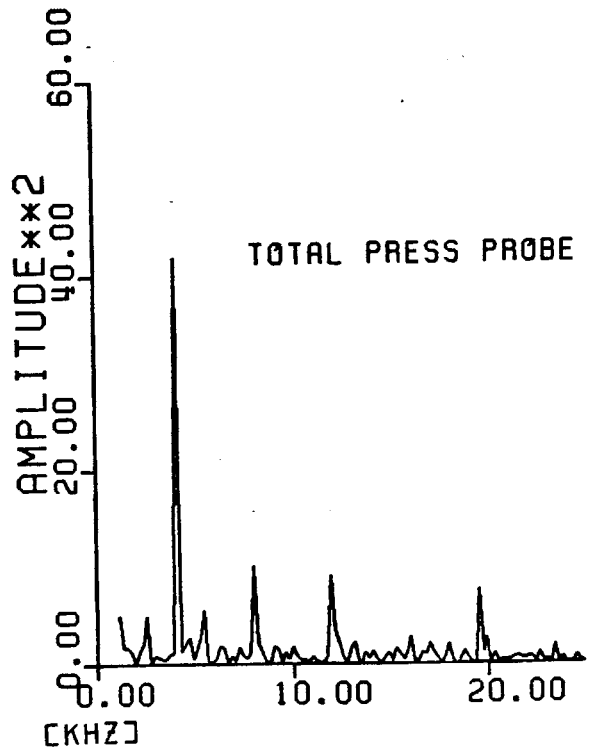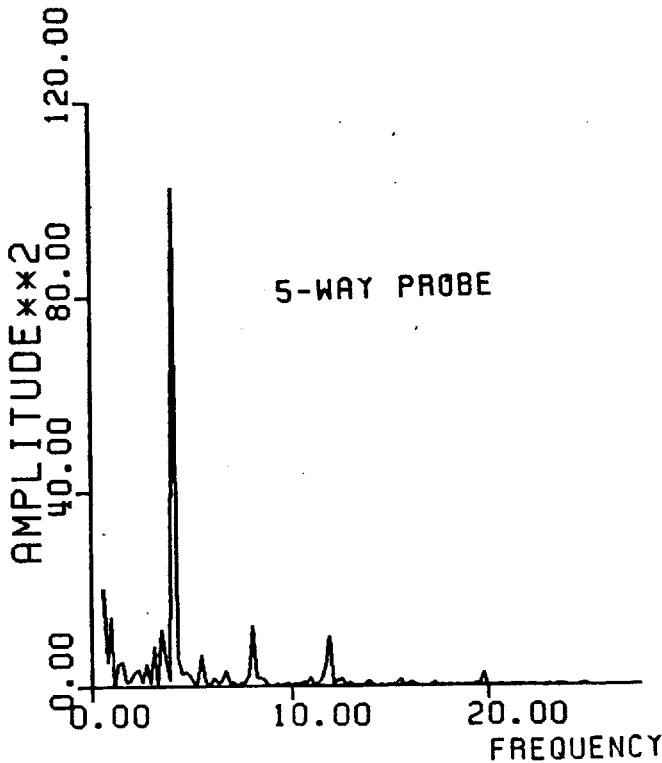
FIGURE 3.14.A   COMPARISON OF TOTAL PRESSURE PROBE MEASUREMENTS TO 5-WAY
PROBE MEASUREMENTS AND THEIR CORRESPONDING FREQUENCY SPECTRA

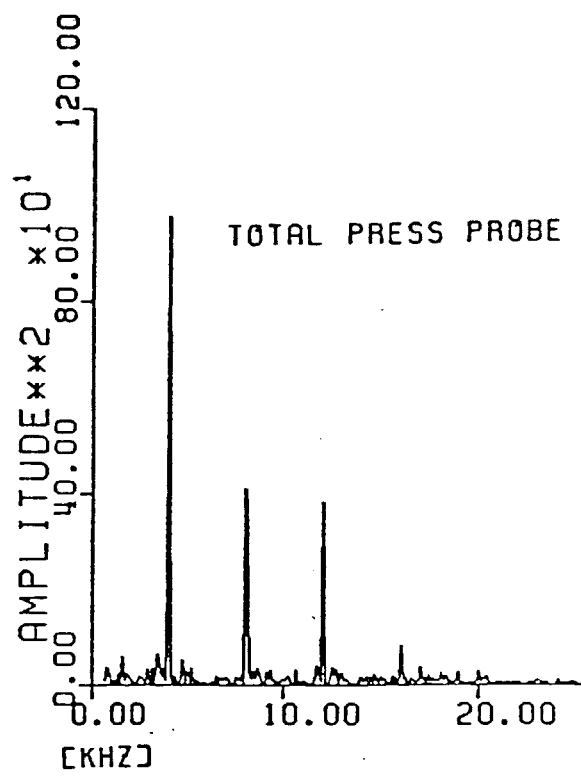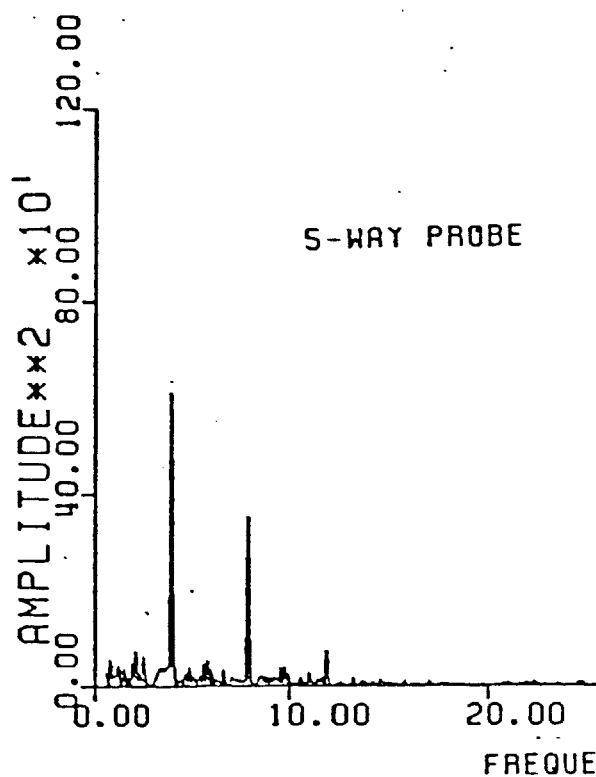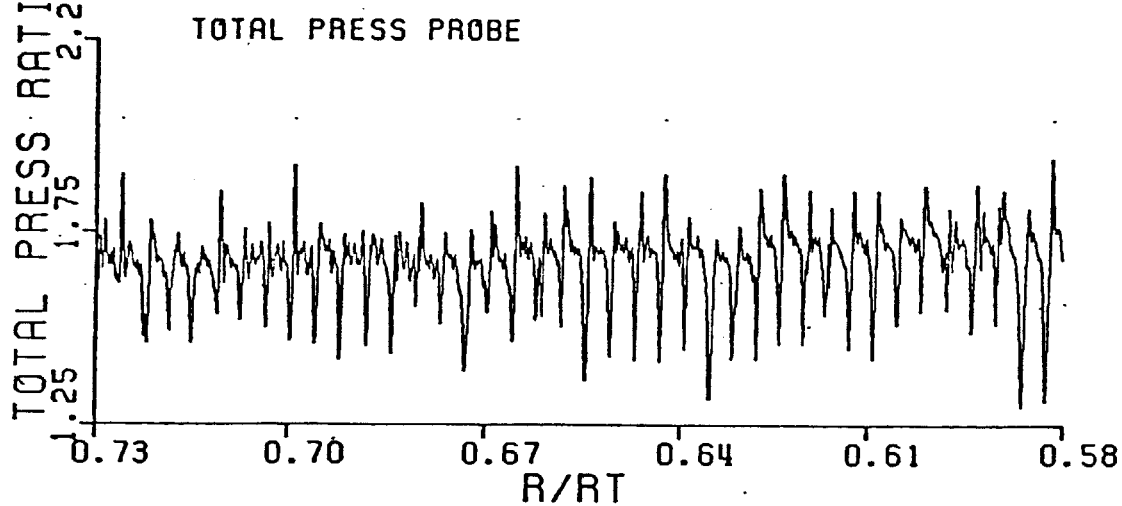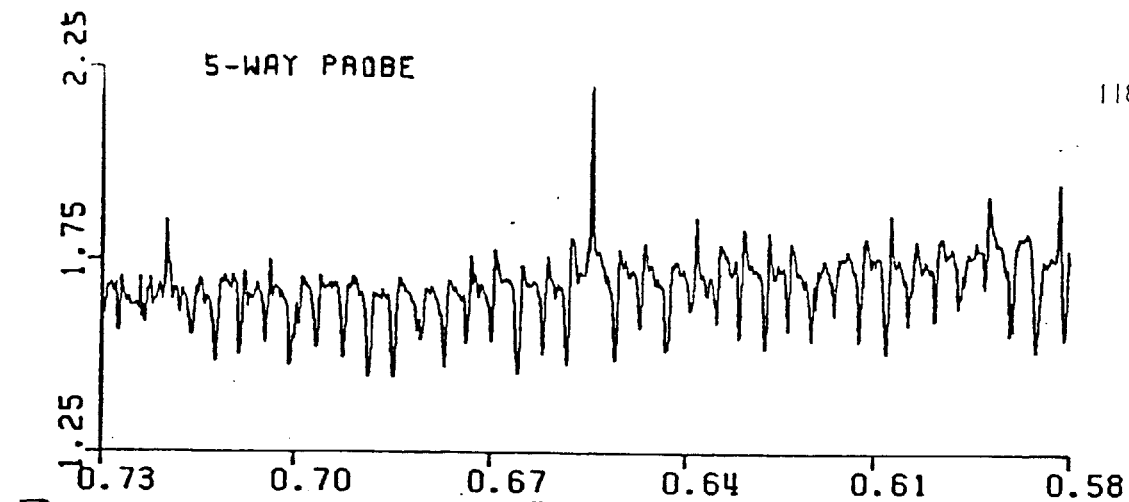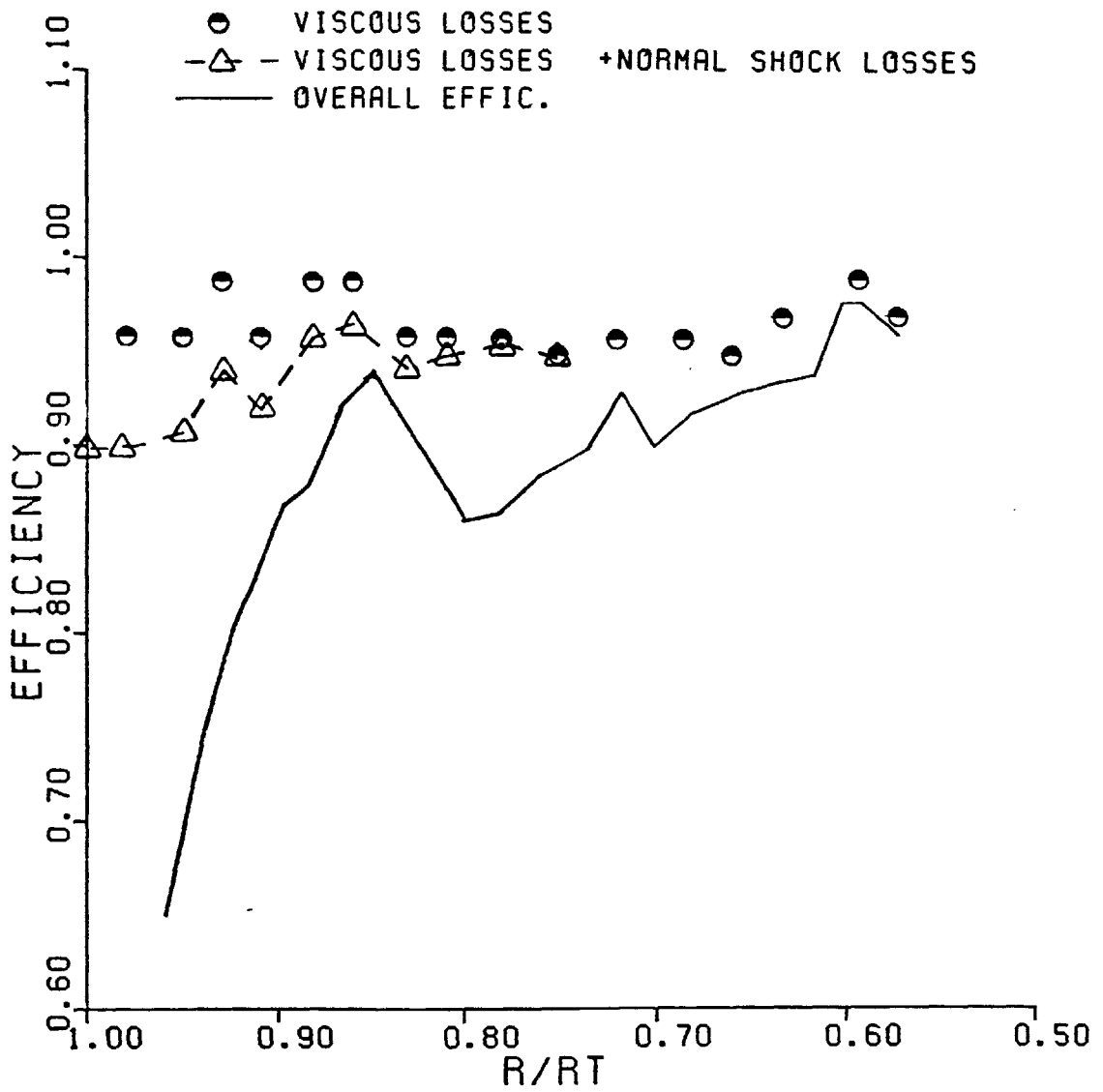FIGURE 3.14.B   COMPARISON OF TOTAL PRESSURE PROBE MEASUREMENTS TO 5-WAY
PROBE MEASUREMENTS AND THEIR CORRESPONDING FREQUENCY SPECTRA

REFERENCES

1. Kerrebrock, J. L., "Flow in Transonic Compressors," Dryden Lectureship in Research, AIAA-80-0124, January, 1980.

2. Kerrebrock, J. L., Epstein, A. H., and Thompkins, W. T., "A Miniature High Frequency Sphere Probe," Proc. ASME Symposium Measurement Methods in Rotating Components of Turbomachinery, 1980.

3. Urasek, D. C., Gorrell, W. T., and Cunnan, W. S., "Performance of Two-Stage Fan Having Low-Aspect-Ratio, First-Stage Rotor Blading," NASA Technical Paper 1493, 1978.

4. Kerrebrock, J. L., "The MIT Blowdown Compressor Facility," MIT Gas Turbine Lab. Report #108, September, 1975.

5. Epstein, A. H., Kerrebrock, J. L., and Thompkins, W. T., "Shock Structure in Transonic Compressor Rotors," AIAA Journal, Vol. 17, No. 4, April, 1979.

6. Thompkins, W. T., "An Experimental and Computational Study of the Flow in a Transonic Compressor Rotor," MIT GTL Report No. 129, 1976.

7. Epstein, A. H., "Quantitative Density Visualization in a Transonic Compressor Rotor," Ph.D. Thesis, MIT, September, 1975.